AFRL-OSR-VA-TR-2014-0039

NANOENERGETICS AND HIGH HYDROGEN CONTENT
MATERIALS FOR SPACE PROPULSION

RICHARD YETTER

PENNSYLVANIA STATE UNIVERSITY

01/28/2014
Final Report

AIR FORCE RESEARCH LABORATORY
AF OFFICE OF SCIENTIFIC RESEARCH (AFOSR)/RSA
ARLINGTON, VIRGINIA 22203
AIR FORCE MATERIEL COMMAND

REPORT DOCUMENTATION PAGE

Form Approved
OMB No. 0704-0188

1. REPORT DATE (DD-MM-YYYY)	2. REPORT TYPE	3. DATES COVERED (From - To)
01-19-2014	Final Report	From 11/1/2010 to 10/31/2013

4. TITLE AND SUBTITLE

NANOENERGETICS AND HIGH HYDROGEN CONTENT MATERIALS FOR SPACE PROPULSION and

Hierarchical Theoretical Methods for Understanding and Predicting Anisotropic Thermal Transport and Energy Release in Rocket Propellant Formulations

5a. CONTRACT NUMBER
FA9550-11-1-0002

5b. GRANT NUMBER

5c. PROGRAM ELEMENT NUMBER

6. AUTHOR(S)

Steven F. Son[1], Vigor Yang[2], Richard A. Yetter[3]

Thomas D. Sewell[4], Donald L. Thompson[4], Michael Ortiz[5], Moshe Matalon[6], and D. Scott Stewart[6]

5d. PROJECT NUMBER

5e. TASK NUMBER

5f. WORK UNIT NUMBER

7. PERFORMING ORGANIZATION NAME(S) AND ADDRESS(ES)

[3]The Pennsylvania State University University Park, PA 16802
[2]Georgia Institute of Technology, Atlanta, GA
[1]Purdue University, West Lafayette, IN
[4]University of Missouri-Columbia, Missouri
[5]Caltech, CA
[6]University of Illinois Urbana-Champaign, IL

8. PERFORMING ORGANIZATION REPORT NUMBER

9. SPONSORING / MONITORING AGENCY NAME(S) AND ADDRESS(ES)

Air Force Office of Scientific Research
Attn: Dr. Mitat Birkan
875 North Randolph Street
Suite 325, Room 3112
Arlington, VA 222203-1768

10. SPONSOR/MONITOR'S ACRONYM(S)

11. SPONSOR/MONITOR'S REPORT NUMBER(S)

12. DISTRIBUTION / AVAILABILITY STATEMENT

Distribution A – Approved for Public Release

13. SUPPLEMENTARY NOTES

14. ABSTRACT

This program concerned the development and analysis of nanoenergetic and high hydrogen content materials for use in propellants. During the first two years of this program, research was conducted on: 1) experimental and multi-scale modeling of the thermo-chemical behavior of nano-aluminum particles, 2) combustion and decomposition studies of metal hydrides including ammonia borane, and 3) the integration of nanomaterials into propellants and the combustion analysis of these materials. During the third and final year of the program, the research concerned the development of theoretical methods for understanding and predicting anisotropic thermal transport and energy release in rocket propellant formulations. This report describes accomplishments from the effort.

15. SUBJECT TERMS
Novel propellants, propellant modeling

16. SECURITY CLASSIFICATION OF: Unclassified			17. LIMITATION OF ABSTRACT	18. NUMBER OF PAGES	19a. NAME OF RESPONSIBLE PERSON Richard A. Yetter
a. REPORT UU	b. ABSTRACT UU	c. THIS PAGE UU	UU	96	19b. TELEPHONE NUMBER (include area code) (814) 863-6375

Standard Form 298 (Rev. 8-98)
Prescribed by ANSI Std. Z39.18

NANOENERGETICS AND HIGH HYDROGEN CONTENT MATERIALS FOR SPACE PROPULSION
and
Hierarchical Theoretical Methods for Understanding and Predicting Anisotropic Thermal Transport and Energy Release in Rocket Propellant Formulations

Final Report, 19 January 2014, FA9550-11-1-0002

Steven F. Son[1], Vigor Yang[2], Richard A. Yetter[3]
[1]Purdue University
[2]Georgia Institute of Technology
[3]The Pennsylvania State University
and
Thomas D. Sewell[4], Donald L. Thompson[4], Michael Ortiz[5], Moshe Matalon[6], and D. Scott Stewart[6]
[4]University of Missouri-Columbia
[5]Caltech
[6]University of Illinois Urbana-Champaign

Abstract

This program concerned the development and analysis of nanoenergetic and high hydrogen content materials for use in propellants. During the first two years of this program, research was conducted on: 1) experimental and multi-scale modeling of the thermo-chemical behavior of nano-aluminum particles, 2) combustion and decomposition studies of metal hydrides including ammonia borane, and 3) the integration of nanomaterials into propellants and the combustion analysis of these materials. During the third and final year of the program, the research concerned the development of theoretical methods for understanding and predicting anisotropic thermal transport and energy release in rocket propellant formulations. This report describes accomplishments from the effort.

TABLE OF CONTENTS

LIST OF FIGURES

5

LIST OF TABLES

I.   Introduction

The last few decades have witnessed a tremendous increase in space-related activities and many more challenging space missions are currently being planned. So far, most space exploration and utilization activities have primarily employed chemical propulsion technology and the situation will continue in the foreseeable future. The progressively ambitious future space-mission goals have identified an acute need for novel, better performing, cost-effective, and safer ways of space exploration and utilization. Unfortunately, none of the current operational propellants have all the desired properties, and the selection of a particular propellant combination is largely a compromise based on various factors such as physical properties, ignition and combustion characteristics, cost, safety, environmental hazards, processing, material compatibility, and availability [1]. Substantial efforts are thus needed towards the development of new propellants to meet the requirements of the next generation of space exploration and utilization activities. The focus on advancing the existing propellant technologies, at this juncture, will benefit all major space programs for the Air Force, NASA, and industry. A typical space mission requires two different types of propulsion systems, viz., launch vehicle (i.e. primary and upper stages) and spacecraft (i.e. on-board) systems. The combination of solid and liquid rockets is typical of launch systems, wherein solid propellants provide a cost effective and simple way to deliver very high thrust required at lift-off, and liquid propellants fulfill the higher specific-impulse requirement of upper stages. Currently, small launches use solid propellants for the sake of economy, simplicity, and operability. The medium and heavy launches use liquid propellants in the main propulsion system, and are usually assisted by solid rocket boosters in the initial stage to meet the thrust requirements.

The propulsion system (including propellants), which is often the largest and the most massive component of a launch vehicle, provides a powerful leverage that can be gained by using high density and better-performing propellants. The overall objective for the advancement of such systems is crucially dependent on the density and specific impulse of the propellant. Conventionally, the requirement of higher specific impulse has led to the use of cryogenic bipropellants.

Liquid oxygen (LOX) and liquid hydrogen (LH) have been most widely used for space missions [2], especially in the western world. Some of the advantages in using LOX/LH propellants are:
- low molecular weight of hydrogen which implies higher specific impulse (30% - 40% higher than other existing rocket propellants)
- non-toxic and clean combustion exhaust
- superior chamber cooling capability
- relatively stable combustion

On the other hand, the disadvantages associated with the use of LOX/LH cryogenic bipropellants are:
- low density of hydrogen which necessitates a large storage volume
- bulky tanks leading to increase in the structural mass
- safety issues linked with hydrogen and oxygen
- very low storage temperatures
- propellant compatibility with materials of storage containers

Due to low temperatures of cryogenic propellants, it is difficult to store them for long periods of time. Consequently, such propellants are less desirable for use in rockets that must be kept launch ready for months together. The tank for storing liquid propellants is typically the highest nonexpendable mass in a chemical propulsion system. Since liquid hydrogen has a very low density, the propellant volume required is many times greater than other denser fuels, thus requiring bulky and massive storage tanks. The use of high-density propellants is an excellent way to reduce the structural mass of storage tanks and associated propellant-conditioning and flow-control components. The increase in propellant density thus translates into a lower take-off weight and a larger vehicle payload capacity. Higher-energy propellant delivers better specific impulse, and consequently helps reduce the required propellant weight for a given

total impulse. Such propellants can achieve the desired performance of a mission with smaller and lighter launch vehicles.

There exists a need to thoroughly identify, and investigate novel propellants in order to achieve desired combinations with higher density, higher specific impulse, and better thermal properties. Alternatives to such propellant systems as LOX/LH need to be explored in a systematic manner.

Additives to hydrogen or the use of hydrocarbons may allow upper stages to deliver a better overall performance with reduced volume and cost [2]. One such fuel with desirable properties which may replace LH is liquid methane. In the past forty years, LOX/methane is the only new propellant combination that has been adopted for flight engines in the United States. Such a lack of innovation highlights the fact that the advancements in propellant technology have been found wanting for a long time. Although LOX/methane provides a reasonable propulsive performance for certain applications, more appropriate and effective propellant combinations must be continuously explored, especially in light of the encouraging advances in the field of energetic materials in the past twenty years. Ammonia borane has already been used with success to produce hydrogen for chemical lasers and fuel cells. The alternatives being considered for the oxidizer LOX are hydroxylammonium nitrate (HAN), ammonium dinitramide (ADN), hydrazinium nitroformate (HNF), and water (H_2O). Gelled propellants are being tested to determine the practicality of letting propellants freeze at low environmental temperatures and thawing them only when required for use. In addition to the above possible combinations, there is a concept to harness powerful chemical bonds between individual atoms of hydrogen, boron, carbon, and aluminum. The atoms could be arrested with a cryogenic solid, and released as they enter the rocket engine. The ongoing progress in nanotechnology can make such propellants a reality.

Among the commonly used bi-propellants are monomethylhydrazine (CH_3NHNH_2, MMH)/nitrogen tetroxide (N_2O_4, NTO) and hydrazine (N_2H_4)/NTO. Due to the toxicity of these propellants, other bi-propellants such as LOX/ethanol and H_2O_2/hydrocarbon are being explored. The catalytic-decomposed N_2H_4 has been used extensively as a monopropellant for the primary propulsion of smaller spacecrafts as well as for gas-generator applications [3]. H_2O_2 has also been used as a monopropellant in the past. With a goal to develop monopropellants with significantly better performance and no hazardous properties, efforts have been focused on aqueous solution of HAN. The HAN-based monopropellants have higher densities and lower freezing points than the state-of-the-art hydrazine. Furthermore they pose no vapor hazard, and do not require any extraordinary storage, handling, or disposal procedures. For very small and micro spacecrafts, several alternative propulsion technologies can provide performance and system benefits. Examples include (a) a warm gas (mixture of hydrogen, oxygen, and an inert gas) propulsion system that offers a high specific impulse as compared to the conventional cold-gas systems, (b) exothermic decomposition of solid and hybrid systems, which offer the high density and simplicity of solid propellants for low-thrust, and quick-response applications, and (c) bipropellant systems using microelectronic mechanical system (MEMS) fabrication technology. In the past, the stringent system design requirements and the reluctance to change them have obviated the use and application of promising high-energetic materials. But it has become increasingly clear that to meet the needs of future space-propulsion activities, a stage has been reached wherein novel and well characterized HDEMs may dictate the overall propulsion system design.

This research effort investigated new energetic materials that feature nanometer length scales and/or materials with potential of yielding high hydrogen yields. In a previous effort, frozen propellants based on nAl and ice were studied, which because of the nanometer sized aluminum particles resulted in fast burning rates and produced hydrogen gas as the primary gaseous combustion product. The present program continued research efforts on nanometer metallics as additives to propellants, with particular emphasis on nanometer aluminum, and also considered materials with high hydrogen content, such as ammonia borane and several metal hydrides. During the first two years of this effort, research was conducted at Penn State University, Purdue University, and Georgia Tech. These efforts included: 1) multi-scale modeling of the thermo-chemical behavior of nano-aluminum particles, 2) further development of aluminum and water solid propellants, 3) performance analysis of metal hydride fuel additives, 4) encapsulation of nanoscale particles in oxidizer crystals, 5) investigation of inclusion

materials in micron scale aluminum, 6) combustion analysis of nano-aluminum with hydroxyl ammonium nitrate (HAN)/water mixtures, 7) decomposition and oxidation studies of ammonia borane (with Professors Adri van Duin and Stefan Thynell at Penn State), and 8) studies on the usage of several of these materials in hybrid rocket motors. Examples of this research are presented in the sections that follow with references to other papers published in the literature as a result of this effort. During the third and final year of this program, the research was conducted at the University of Missouri-Columbia, Caltech, and the University of Illinois Urbana-Champaign. This research focused on the development of theoretical methods for understanding and predicting anisotropic thermal transport and energy release in rocket propellant formulations. A summary of the accomplishments of this one year effort are also provided in the report.

II.   Ammomia Borane as a High Hydrogen Content Propellant Additive (Penn State)

Future space missions with chemical propulsion systems will require the development of propellants with increased performance. To increase the energy density (per unit mass) over current hydrocarbons, earlier studies identified hydrogen, beryllium, boron, or some combination thereof as elements of future fuels [4]. Molecular hydrogen has been used successfully as a liquid fuel for rocket propulsion. However, it requires cryogenic facilities, which complicates handling and rocket design. Beryllium and its compounds have generally been deemed too toxic to be viable fuels. Boron, however, is of strong interest due its high combustion enthalpy on both a mass and volume basis. It is typically introduced as a particle with a passivation layer, and as such there are significant difficulties with ignition and complete combustion [5]. Similarly, boranes (B_xH_y) have been of interest for years as a propellant fuel because of their high energy density. The liquid pentaborane (B_5H_9) has 60% greater energy density than conventional jet fuel [4]. However, problems with the pyrophoricity and toxicity of boranes ultimately proved them too dangerous for widespread use.

Recently, ammonia borane (AB, NH_3BH_3), a solid compound at room temperature, has been the subject of vigorous study to examine its potential for storing hydrogen at high densities. AB contains 19.6% hydrogen by mass. The initial studies on AB decomposition [6, 7] showed that it would slowly decompose to produce hydrogen gas. Unlike the previously investigated borane fuels (B_2H_6, B_5H_9), AB is not known to have significant toxicity or safety problems, and it does not require any special storage conditions [8].

Increasing specific impulse (I_{sp}) is one of the main objectives in developing novel rocket propellants for deep space travel. Since I_{sp} is proportional to the square root of chamber temperature divided by the average molecular weight of the products, AB is of interest because it undergoes an exothermic decomposition to release H_2 [9]. Thermochemical calculations and preliminary laboratory scale motor tests confirm that AB can indeed improve specific impulse in a paraffin-fueled hybrid rocket motor [10]. However, this study also showed that significant additions of AB result in a considerable quantity of condensed-phase products accumulating on the solid-fuel surface, leading to a decreased regression rate. To understand the chemistry related to these results, a better understanding of AB decomposition is required.

A.   Using Molecular Dynamics Simulations with a ReaxFF Reactive Force Field to Develop a Kinetic Mechanism for Ammonia Borane Oxidation (with Adri van Duin, Penn State University)

The use of chemical kinetic modeling has been used with great success in understanding combustion phenomena, but such modeling requires the knowledge of all relevant elementary chemical reactions and the reaction rates associated with them. The kinetics of boron reactions in the presence of hydrocarbon oxidation [11-14] have been reported previously. Conversely, elementary reactions and rate parameters describing the oxidation of B/N/H species are significantly lacking from the literature. Acquiring experimental data for elementary reaction rates in a completely novel system is time consuming and often, although still very important. Computational techniques, such as molecular dynamics (MD), have matured along with modern computing power and can aid greatly in the development of kinetic mechanisms for novel systems.

Advances in the speed and accuracy of computational quantum chemistry (QC) have allowed for the calculation of molecular geometries and energies for small molecules with relative ease. Nevertheless, it is still impractical, due to computational expense, to simulate a large system of reacting molecules (100 or more) over a relevant time scale using a purely quantum mechanical description. To simulate large systems at an atomistic scale, it is typical to use a force field approach instead of QC. For example, the MM3 force field [15] has been used successfully in the description of hydrocarbons, and more general force fields, such as DREIDING [16], are able to provide relatively accurate results for a

number of different elements.   However, to allow for the simulation of large systems, these force fields use sufficiently simple descriptions of bonding and are not able simulate chemical reaction because they cannot model the bond breaking and formation. One approach to analyzing such systems is through the development of reactive force fields.

Recently, a reactive ReaxFF force field has been developed to study the oxidation of ammonia borane (NH_3BH_3) [17]. ReaxFF is a reactive force field method which uses "bond-order" to describe bonds as a function of inter-atomic distance, as opposed to explicitly defined bonding [18]. This allows for continuous breaking and forming of bonds, as the bond order is updated at every iteration as atom distance changes. Furthermore, a ReaxFF force field can be parameterized using data derived from either experimental or QC calculations, so that no extensive experimental data is needed [18]. The ReaxFF method has been discussed in depth in previous publications, which should be referred to for greater detail [18-20]. .

Using the ReaxFF reactive force field developed previously [17] with data acquired through density functional theory (DFT) calculations, this paper discusses the development of a chemical kinetic mechanism based on MD simulation results. The first step was to conduct MD simulations and analyze the results to identify chemical pathways. From these, the intermediate species and elementary reactions of importance can be deduced. For species for which there were no thermochemical data available, the enthalpy and entropy of formation were calculated using QC methods, along with specific heat as a function of temperature.   Next, the rates for new reactions were estimated. In this work, simple collision theory was used to attain initial estimates of reaction rates. Chemical kinetics calculations were then performed and compared with the MD results. Refinements to the mechanism are made by performing additional MD simulations to isolate specific steps in the reaction progress and by using more accurate *ab initio* reaction rate calculation methods for the most important reactions, for example, as determined by sensitivity analysis on the chemical kinetics calculations.

The MD simulations used to study the chemical pathways through which AB oxidation proceeds were all performed under NVT conditions (constant number of atoms, volume, and temperature). A Berendsen thermostat [21] with a 0.1 ps damping constant was used to control temperature. For an accurate simulation, the force field must be able to model flexible molecules with flexible bonds that exhibit translational, rotational, torsional, and vibrational motion. Normally, a time step one order of magnitude smaller than the shortest motion, or approximately 0.5 to 1.0 fs, is required. A smaller time step is required when using ReaxFF because the charges and bond orders are allowed to change at every time step. For ReaxFF MD simulations which exceed temperatures of 2500 K, a time step of 0.1 fs is preferred for efficient coverage of the phase space and collisions and reactions to occur smoothly.

For this work, molecules were simulated inside of a 2.5 nm periodic cube. The use of high pressure and temperature is required in ReaxFF simulations in order to create enough successful molecular collisions within reasonable simulation times. For the simulations discussed here, the initial system pressure in approximately 170 bar, however at the highest temperatures it can exceed 2500 bar. The requirement of high pressure makes MD simulations best suited for modeling systems such as rocket and gun propellants or shock induced reactions.

To model the chemistry of a system, the thermochemical parameters of each species must be known, including heat of formation, entropy of formation, and specific heat. Since borane amines have been studied recently for chemical vapor deposition of BN films and hydrogen storage, thermochemical data have been calculated for many of the pertinent B/N/H species with ab intio QC methods, as reported in the literature [22-24]. However, the thermochemical properties of B/N/H/O species are not available. Therefore, DFT calculations were undertaken to calculate these parameters for this study.   The DFT-calculations used to derive the thermochemical properties were performed using the B3LYP functional [25]. This method combines exact HF exchange with the Becke generalized exchanged functional of Becke [26] and Lee, Yang, and Parr [27] correlation functional. For the B, H, O, and N atoms, all electrons were included using a modified variant of the Pople 6-311G**++ basis set [28, 29]. All calculations were performed using the Jaguar 7.8 program package [30].

11

The first step in calculating the heat of formation at the standard temperature ($\Delta H_{f,298K}$) for a given molecule (M) was to calculate the atomization energy ΣD_0, as given by Eq.

$$\Sigma D_0(M) = \sum_{atoms} \upsilon \varepsilon_0(X) - \varepsilon_0(M) - \varepsilon_{zpe}(M) \tag{1}$$

where $\varepsilon_0(X)$ is the total energy of atom X, υ is the stoichiometric coefficient for a given atom, $\varepsilon_0(M)$ is the total energy of molecule M, and $\varepsilon_{zpe}(M)$ is the zero point energy of molecule M.

Given the atomization energy of the molecule, along with the heats of formation for the constituent atoms, the heat of formation of molecule M at 0 K was computed according to Eq. . Subsequently, the heat of formation at 298 K was computed using Eq.

$$\Delta H_f(M,0K) = \sum_{atoms} \upsilon \Delta H_f(X) - \Sigma D_0 \tag{2}$$

$$\Delta H_f(M,298K) = \Delta H_f(M,0K) + \left[H_M(298K) - H_M(0K) \right] \\ - \sum_{atoms} \upsilon \left[H_X(298K) - H_X(0K) \right] \tag{3}$$

Using vibrational analysis, the specific heat and entropy of the molecule was calculated for a specified temperature. By generating data for a range of temperatures, the parameters for a fourth order curve fit of specific heat were calculated for two temperature ranges (200-1000 K and 1000-6000 K), as well as integration constants describing enthalpy and entropy, to be used in equilibrium and kinetics programs such as CHEMKIN [31].

Equilibrium calculations were performed using CHEETAH 4.0 [32] with the JCZS product library developed by Hobbs and Baer [33]. Chemical kinetic calculations were performed using CHEMKIN, release 4.0 [31]. To describe hydrogen oxidation and ammonia chemistry, the 95 reaction kinetic mechanism published by Lindstedt *et al.*[34] was used. The B/O/H reactions were described using the first 30 reactions in the mechanism published by Yetter *et al.*[13]. For some of the important reactions in AB decomposition, reaction rates have been proposed by Nguyen *et al.* [35] using *ab initio* QC calculations and RRKM theory. At 1 atm, the Arrhenius reaction rate equations for AB hydrogen elimination and B-N bond breaking are given by Eq. and , respectively.

$$H_3NBH_3 \rightarrow H_2NBH_2 + H_2 \\ k = 3.841E+12 \cdot \exp\left(-35.60/_{RT} \right) \tag{4}$$

$$H_3NBH_3 \rightarrow NH_3 + BH_3 \\ k = 1.545E+12 \cdot \exp\left(-21.90/_{RT} \right) \tag{5}$$
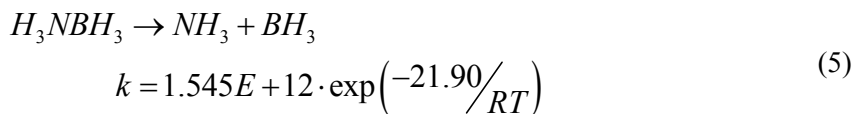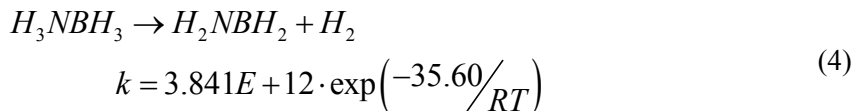
Nguyen *et al.* also studied the catalytic effect of BH_3 on hydrogen elimination from AB. QC calculations show that a collision with BH_3 can significantly reduce the energy barrier for hydrogen release. Therefore, a separate rate equation for this reaction was specified [35], as given by Eq. .

$$H_3NBH_3 + BH_3 \rightarrow H_2NBH_2 + H_2 + BH_3 \\ k = 6.330E+11 \exp\left(-22.40/_{RT} \right) \tag{6}$$
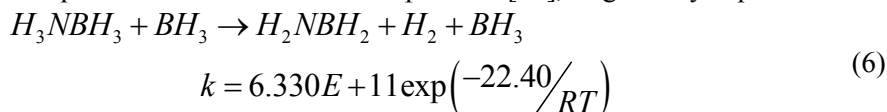
For a preliminary evaluation of reaction rate parameters, simple collision theory provides a simple, upper-limit estimation. Although this method of estimation is subject to a larger degree of uncertainty, it accomplishes the objective of establishing an initial set of rate constants which are physically reasonable and collectively self-consistent. According to simple collision theory, the frequency factor A may be written as in Eq., where $\wp$ is the steric factor, which is the ratio of successful collisions to total collisions, σ_{AB} is the hard sphere collision diameter for a collision between molecule A and molecule B, k_b is Boltzmann's constant, T is temperature, and μ_{AB} is the reduced mass.

$$A = \wp\, \sigma_{AB}^2 \left(\frac{8\pi k_b T}{\mu_{AB}} \right)^{1/2}; \quad \mu_{AB} = \frac{m_A m_B}{m_A + m_B}; \quad \sigma_{AB} = \frac{1}{2}\cdot\left(\sigma_A + \sigma_B\right) \tag{7}$$

The collision diameter where σ_A and σ_B are the hard sphere diameters of the colliding molecules. Hard sphere diameters for well known species were taken from Kee *et al.* [36], while those not available in the literature (most boron containing species) were estimated using a semi-empirical relationships first proposed by Hirschfelder and Eliason [37]. The general form for this relationship is given by Eq. , where $\bar{r}$ is the mean atom radius and A and B are constants. Hirschfelder and Eliason [37] proposed a relationship for diatomics where A=4/3 and B=1.8 Å. Svehla [38] extended the relationship to triatomics with constants of A=10/9 and B=1.7 Å. Based on values for σ in the literature [36, 38], this formula was extended to larger molecules (four to eight atoms) for this study, where constants of A=8/23 and B=2.95 Å were found to match well with data for a wide range of larger molecules. Values for $\bar{r}$ were taken from Clementi *et al.* [39].

$$\sigma_N = A\left(\sum_i^N \bar{r}_i \right) + B \tag{8}$$

One particularly important reaction not previously studied is the second hydrogen elimination step from AB. To estimate the reaction rate for this step, a more accurate approach was taken. Using a transition state search in Jaguar 7.8 with B3LYP/6-311G**++, a transition state for hydrogen elimination from H_2NBH_2 was found, as pictured in Figure 1. The reaction rate was then calculated, using the initial and transition state description, in the ChemRate program [34]. An Arrhenius rate equation was determined, as shown in Eq..

$$k_{H_2NBH_2 \rightarrow HNBH + H_2} = 5.488E+13 \exp\left(-83.97/RT \right) \tag{9}$$

83 kcal

31 kcal
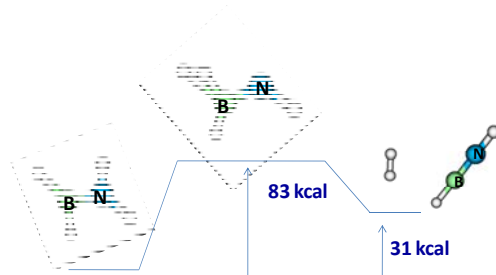
Figure 1: Reaction coordinate of hydrogen elimination from H_2NBH_2, showing the reactant, transition state, and product, as calculated with Jaguar 7.8 using B3LYP/6-311G++**

Figure 2 shows the equilibrium products as a function of temperature for a stoichiometric reaction of AB and molecular oxygen at a pressure of 1 atm. Over the range of temperatures shown, the main equilibrium products always consist of gaseous H_2O, N_2, and to a lesser extent, H_2. However, the species

containing boron atoms changes significantly over this range. Below 650 K, the majority of boron exists as solid phase HOBO. Between 650 and 900 K, boron exists mostly as gaseous $B_3H_3O_6$ combined with gaseous $B_3H_3O_3$ and liquid phase B_2O_3. Liquid B_2O_3 is the primary boron containing species from 900 K, until gaseous HOBO overtakes it around 1700 K.
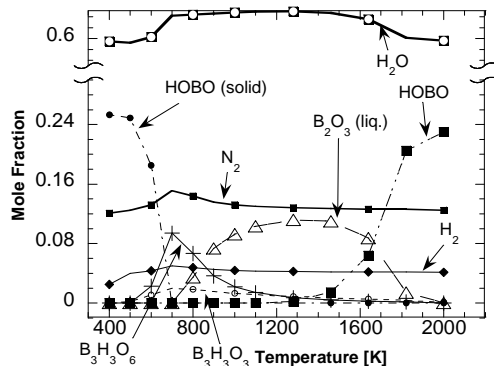
Figure 2: Mole fractions of equilibrium products of a stoichiometric reaction of AB and molecular oxygen at a pressure of 1 atm

Figure 3 (a.)-(c.) shows snapshots from a temperature ramping NVT MD simulation starting with 20 AB and 45 O_2 molecules in a 2.5 nm periodic cube, with an imposed heating rate of 0.00522 K/fs. The composition was determined as a stoichiometric mixture according to Eq. . It should be noted that the stoichiometric mixture ratio remains the same regardless of whether the boron forms B_2O_3 or HOBO.

$$NH_3BH_3 + \frac{9}{4}O_2 \rightarrow \frac{1}{2}N_2 + HOBO + \frac{5}{2}H_2O \qquad (10)$$
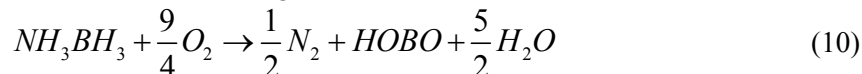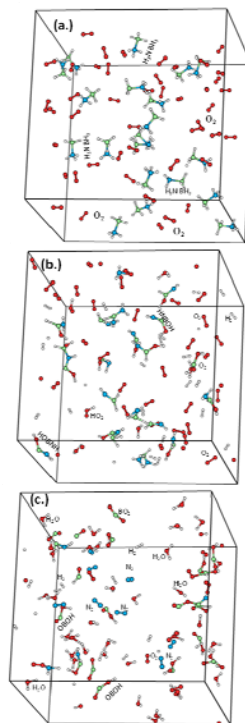
Figure 3: Snapshots from a temperature ramp simulation with 20 AB molecules and 45 O2 molecules. (for color figure, green=boron, blue=nitrogen, white=hydrogen, red=oxygen) showing a.)initial minimized geometry b.)T=2500 K c.) T=5000 K

Figure 3 (a.) shows the initial geometry with a 2.5 nm transparent periodic cube, where the molecules have been randomly placed and subsequently energy minimized. Figure 3 (b.) shows a snapshot at the middle of the simulation, where the thermostat is set to 2500 K, and Figure 3 (c.) shows the final frame of the simulation with thermostat setting of 5000 K. At the point in the simulation which Figure 3 (b.) pictures, the AB molecules have all been dehydrogenated leaving no AB molecules and a significant amount of molecular hydrogen in the system. Most of this H_2 has not started to react with the oxygen, but there are some H_2O and HO_2 molecules in the system. Several of the dehydrogenated AB molecules have been attacked by oxygen, forming HNBOH molecule. In Figure 3 (c.), it can be seen that many of the expected equilibrium products have been formed. Molecular hydrogen has been converted to H_2O, the majority of nitrogen exists as N_2, and the boron exists primarily as HOBO.

Figure 4 shows a plot of the major species observed versus temperature for the temperature ramping NVT MD simulation pictured in Figure 3. Consistent with MD simulations on AB in the absence of oxygen, some of the AB is converted to NH_3 and BH_3 through B-N bond cleavage in the low temperature range. The NH_3 and BH_3 do not oxidize, and the B-N bonds begin to reform as the temperature increases beyond 1250 K. Around 1000 K, H_2 begins to be generated through the uni-molecular hydrogen elimination from AB. Just as shown previously in the snapshots, H_2 molecules are oxidized to form H_2O, while the B-N containing molecules undergo a reaction sequence, which ultimately ends up producing N_2 and HOBO.

15
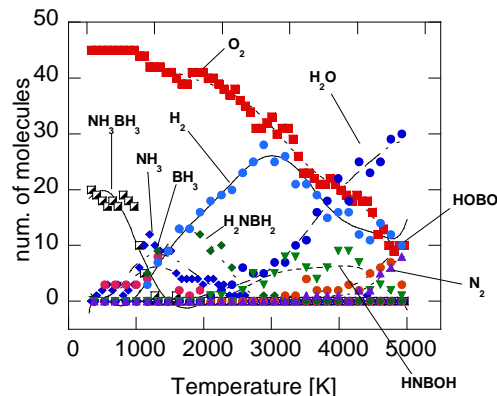
Figure 4: Temperature ramping MD simulation of AB and oxygen molecules

Figure 5 is a flow diagram describing the reaction sequence through which AB progresses to form the equilibrium products H_2O, N_2, HOBO, and possibly B_2O_3 in the MD simulations. As mentioned previously, the B-N bond in AB is relatively weak and tends to break at low temperatures, but as their concentrations become greater the reverse reaction quickly becomes dominant and AB is reformed. The reaction sequence of the AB molecule is down the left side of the diagram, undergoing a first and then second hydrogen elimination, contributing to a large concentration of H_2 in the system, and resulting in the HNBH molecule. The strain energy for the HNBH molecule to undergo hydrogen elimination is too great, and the B-N bond in this molecule is quite strong (~170 kcal, as determined by a coordinate scan in Jaguar 7.8 using B3LYP/6-311G**++). For the reaction to proceed further towards the equilibrium products, the boron side of this molecule will react with O_2 or radicals formed from H_2/O_2 chemistry, since the boron atom is electron deficient and the B-H bond is the weakest in the molecule. The MD simulation results show the HNBOH molecule to be a major product. The B-N bond is still relatively strong in the HNBOH molecule, with a bond dissociation energy of 143 kcal/mol. However, the B-N bond must be severed in the conversion to the equilibrium products. Investigating the minor species formed in the MD simulations reveals that the boron side of HNBOH is still likely to react with OH, O, and O_2, while the nitrogen side lowers its energy by forming another bond with a hydrogen, leading to the formation of what turns out to be a very low energy species, $H_2NB(OH)_2$. The B-N bond energy for $H_2NB(OH)_2$ has been reduced to approximately 111 kcal, making it the weakest bond in the molecule. The unfavorable entropy of this molecule means that it easily dissociates at high temperatures. B-N bond cleavage results in the formation of an NH_2 an $B(OH)_2$. The $B(OH)_2$ molecule can easily form HOBO with a hydrogen extraction by the NH_2. The pathways for N/H species to N_2 are well studied and can be described by reactions found in the literature [34]. Furthermore, depending on the system temperature, it may be favorable for HOBO to be converted to B_2O_3 and H_2O, the pathways of which have also been previously reported [13].
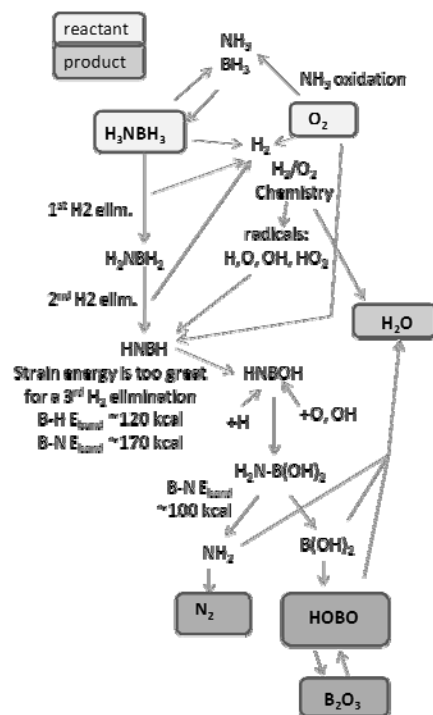
Figure 5: Flow chart describing the pathways of AB oxidation, formulated through ReaxFF MD simulations of AB and O₂.
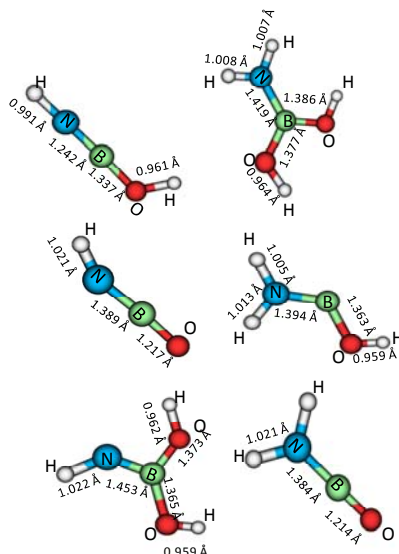
Figure 6: Molecular geometries of B/N/H/O species, calculated using Jaguar 7.8 [24] with the B3LYP functional and 6-311G**++ basis set

Figure 6 contains the molecular geometries of B/N/H/O species that were deemed relevant to the kinetics of AB oxidation from the MD simulations and for which prior data was not available. Table 1 reports the atomization energy, heat of formation and entropy of formation for molecules shown in Figure 6, as well as previously studied molecules relevant to this study, as calculated with DFT calculations using the B3LYP functional and the 6-311G**++ basis set. Although it is known that B3LYP is not the most accurate method for calculating energies (post hartree-fock methods such as CCSD are generally considered to have higher accuracy for energy calculations), it is a very reliable and efficient method and

gives satisfactory results for this initial study. As mentioned above, the H₂NB(OH)₂ molecule exhibited a very low heat of formation (-179.90 kcal/mol at 298 K), the lowest of the molecules examined here. However, equilibrium calculations still show this molecule is not a favored product due to the effect of entropy.

Table 1: Thermochemical parameters calculated using Jaguar 7.8 [30] with the B3LYP functional and 6-311G**++ basis set and Eq. -, compared to values from the literature [a][41] [b][23] [c][22]

| Molecule | Molecular Energy [Hartrees] | Zero Point Energy [kcal] | ΣD_0 [kcal] | $\Delta H_f(0K)$ [kcal/mol] | calculated | | literature | |
					$\Delta H_f(298K)$ [kcal/mol]	S(298K) [cal/mol*K]	$\Delta H_f(298K)$ [kcal/mol]	S(298K) [cal/mol*K]
HOBO	-176.0402181	12.75	427.59	-122.98	-123.65	58.04	-133.99[a]	57.3[a]
NH₃	-56.576047	21.52	273.55	-6.56	-8.24	48.16	-10.97[a]	46.07[a]
BH₃	-26.621103	16.40	267.91	22.56	25.49	48.55	25.50[a]	44.90[a]
B₂O₃ (gas)	-275.620437	11.87	637.89	-191.04	-191.26	69.47	-199.53[a]	67.82[a]
H₃NBH₃ (gas)	-83.25008	43.70	568.90	-11.45	-15.85	59.43	-13.5[b],-19.95[c]	58.3[c]
H₂NBH₂	-82.07418	30.04	475.01	-21.09	-23.84	55.91	-15.9[b],-23.2[c]	54.78[c]
HNBH	-80.83477	14.89	342.75	7.64	12.05	37.27	12.8[b], 11.0[c]	41.62[c]
HNBOH	-156.13090	18.90	469.67	-60.44	-61.43	62.41	-	-
H₂NBO	-156.166813	20.06	491.05	-81.82	-83.10	61.28	-	-
H₂NB(OH)₂	-232.696329	37.86	747.79	-176.19	-179.90	69.13	-	-
HNBO	-155.477472	11.55	382.17	-24.70	-25.28	59.80	-	-
H₂NBOH	-156.708865	27.11	508.97	-47.98	-50.21	63.59	-	-
HNB(OH)₂	-232.002435	29.12	636.27	-116.45	-119.28	69.47	-	-

Figure 7 shows the results of a constant pressure, constant energy chemical kinetics calculation performed in CHEMKIN 4.0 [31]. The initial mixture consisted of a stoichiometric mixture of AB and air. The mechanism contains the reactions from the literature as discussed earlier [13, 34], as well as 52 new reversible reactions, which are listed in Table S1 in supplemental material. At very early times, not visible in Figure 7, the B-N bond breaks in AB, quickly inundating the system with NH₃ and BH₃. As in the MD simulations, the reverse reaction quickly becomes important and the NH₃ and BH₃ are converted back to AB. At the same time, the AB hydrogen elimination reaction takes place, converting all of the AB to H₂NBH₂ and H₂ after approximately 1 ms. The H₂ is slowly consumed through reaction with O₂, injecting some radicals into the system and forming H₂O, which leads to an increased temperature. After approximately 20 ms, H2NBH2 begins to be converted to HNBH and more H₂O. The mole fraction of HNBH steadily increases until just before the rapid oxidation event at 62 ms, where it is converted to HOBO and N₂. A sensitivity analysis shows that the most important elementary reaction in the overall reaction progress is the chain branching $H + O_2 \rightarrow OH + O$, while reactions that compete for the consumption of H atoms, such as $HBNH_2 + H \rightarrow HNBH + H_2$ and $H_2BNH + H \rightarrow HNBH + H_2$, are the most inhibiting to the ignition of the system.
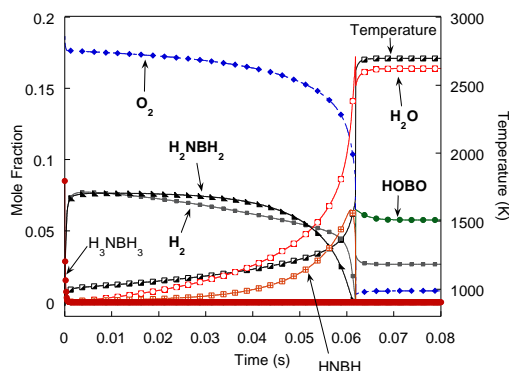
Figure 7: Plot of species mole fraction and temperature versus time for a constant pressure and energy kinetics calculation performed in Chemkin 4.0

Due to its high hydrogen content, AB has the potential to increase performance if used as a fuel in chemical propulsion applications. Molecular dynamics simulations have been performed to examine the oxidation of AB using a previously developed ReaxFF reactive force field developed to describe B/N/H/O chemistry [11]. The results of these simulations were used to identify chemical pathways, important intermediate species, and a series of elementary reactions for the conversion of AB and molecular hydrogen to equilibrium species. DFT calculations were performed using the B3LYP functional and the 6-311G**++ basis set in the Jaguar 7.8 software to calculate thermochemical properties of unknown species. Estimated reaction rates were combined with known reactions to assemble a chemical kinetic mechanism for AB oxidation. This mechanism was used to perform constant pressure and enthalpy kinetics calculations. These calculations show the reaction proceeds as follows: rapid decomposition of AB (H_3NBH_3) to form hydrogen and H_2NBH_2, reaction of the hydrogen to form radicals and H_2O and raise the temperature, dehydrogenation of H_2NH_2 to form HNBH, and finally, an ignition event which rapidly converts the intermediates to the equilibrium products .

These results will be used to design experiments to further investigate and validate the reaction kinetics of AB oxidation. Through refinement procedures, critical reactions in this mechanism will be identified and targeted for more accurate reaction rate estimate using *ab initio* methods, such as transition state theory.

B. Confined Rapid Thermolysis Studies of Ammonia Borane (with Stef Thynell, Penn State University)

Contemporary AB research, recently reviewed by Staubitz *et al.* [42], is primarily concerned with generating hydrogen for use in proton-exchange fuel cells, and using catalysis or other methods to provide increased hydrogen release at low temperatures. The thermal decomposition of AB, first studied by Hu *et al.* [43], has recently been investigated in a series of publications emanating from a group at Friedberg University of Mining and Technology [44, 45, 46]. These studies rely mostly on combination of TGA/DSC experiments.

The first of these studies [44] shows that for sufficiently slow heating rates (0.05 K/min), or isotherms above 70ºC for sufficient time (~30 hours), AB fully completes the first decomposition step below its melting temperature (104ºC) [44], demonstrating that at the low limit of heating rate, AB can fully undergo its first exothermic decomposition step without changing phase. Following the lengthy isotherms ranging from 70-90 ºC, the resulting condensed-phase product was determined to be polymeric aminoborane [(NH₂BH₂)ₓ] [44]. At increased heating rates, the compound will melt prior to the bulk of the decomposition, with gas release resulting in a vigorous foaming.

Additionally, the investigations of Wolf *et al.* [44] and Baitalow *et al.* [45] at slow heating rates (≤ 5 K/min) show that the percent mass loss increased with an increasing heating rate, while the volume

19

of evolved gas (as measured by water displacement) was independent of heating rate. Assuming hydrogen was the only product released into the gas phase, Baitalow *et al.* measured approximately 2.2 mol H_2/mol of AB when heating up to 190ºC, corresponding to a total mass loss of 14.3 percent for all heating rates [45]. At a heating rate of 1 K/min, the gravimetric mass loss recorded was roughly 15 percent, corresponding closely with their volumetric measurement of hydrogen. However, at a heating rate of 5 K/min, the gravimetric mass loss was approximately 23 percent, about 1.6 times the mass of the measured hydrogen [45]. This result from Baitalow *et al.* [45] demonstrates that a certain percentage of the decomposition gases are either condensable at room temperature or are water-soluble. Furthermore, the amount of these condensable/water-soluble products increases with increasing heating rate. Gas-phase FTIR/MS studies performed in conjunction with these TGA/DSC studies give evidence that these products consist of monomeric aminoborane (BH_2NH_2), borazine (c-$[BHNH]_3$), and small amounts of other BNH_x species [45].

Stowe *et al.* [47] have studied the mechanism of thermal decomposition of AB below its melting point by probing the solid phase using nuclear magnetic resonance (NMR) spectroscopy. Using the NMR data, they have proposed a mechanism through which the AB can react to form polymeric amino-borane (PAB) and release hydrogen into the gas phase. The NMR spectra show the reaction is initiated with the formation of a "mobile" phase of AB, which then leads to the formation of an ionic compound, the diamoniate of diborane or DADB $[(NH_3)_2BH_2]^+[BH_4]^-$. It is suggested that the more reactive DADB will react with the surrounding AB, resulting in hydrogen release and amino-borane polymerization.

Another detailed study of AB decomposition has recently been published by Frueh *et al.* [13], in which materials characterization techniques are used in addition to TGA/DSC analysis to understand the chemical pathways of AB decomposition. This study claims to observe a third hydrogen release at a temperature of 1170°C, with significantly slower reaction rate than the first two hydrogen releases. The resulting material after prolonged heating was determined to be hexagonal boron nitride through the use of several material characterization techniques [48].

For energetic materials, the kinetic decomposition pathways may be highly dependent on the heating rate. For example, Oyumi and Brill found that with RDX decomposition, changing the external heating rate results in a shift from CH_2O and N_2O as the main decomposition products at low heating rates to HCN and NO_2 at high heating rates [49]. Therefore, to understand the decomposition behavior of propellant ingredients, it is widely recognized that the process must be studied using both slow and rapid heating conditions. Previous works [43-46] have only examined decomposition at slow heating rates ($\leq$10 K/min), where the time scale for reaction is on the same order as the time scale for heating. In this work, the decomposition of AB is studied using confined rapid thermolysis (CRT). In this experiment, the sample is heated at rates of approximately 2000 K/sec to a set temperature where diagnostics of the isothermal decomposition are performed. TGA/DSC experiments are also performed to investigate changes in mass loss and heat release with increased heating rate.

The ammonia borane used in this study was purchased from Boroscience International. The material was specified to be 98% pure by the supplier using proton and ^{11}B NMR spectroscopy. Its physical appearance is that of a white powder.

The CRT experiment was previously described in [50]. In this experiment, a small amount of material (~0.5 mg) is heated in a narrow space between two flat surfaces. Two copper rods, 53 mm in height and 15.6 mm in diameter, are heated to a preset isothermal condition, using high-watt density cartridge heaters. The copper rods are then compressed against the sample holder, consisting of a retaining ring and thin metal foils, using a pneumatic piston cylinder. The sample holder maintains a sealed 300 μm gap between the heaters, except for a rectangular slit that allows decomposition gases to escape into the cool atmosphere and into the modulated beam of the FTIR. The CRT apparatus is used in conjunction with two diagnostic tools to examine the gas-phase species: rapid scanning FTIR transmission spectroscopy, and time-of-flight mass spectrometry (ToF-MS). These two diagnostic tools complement one another and are most effective when used in conjunction.

For the CRT/gas-phase FTIR spectroscopy, the setup is contained in a constant pressure chamber filled with N_2. The modulated FTIR beam, which enters and exits the chamber via ZnSe windows, passes

through the decomposition gases that emanate from a rapidly heated sample. The Bruker IFS 66/S FTIR spectrometer is programmed to acquire the transmissivity spectrum with a spectral resolution of 2 cm^{-1} and a temporal resolution of 50 ms.

As previously described by Chowdhury *et al.* [51], the ToF-MS measurements take place with an identical CRT heating system inside a low-pressure chamber. A commercially available ToF-MS spectrometer is used. Several stages of vacuum are used to generate a molecular beam from the evolved decomposition gases. The gases first pass through a 100 μm orifice into the first stage, pumped down to 10^{-4} Torr. Subsequently, the gases pass through a 1 mm Ni skimmer to the second stage, pumped to 10^{-6} Torr, and a 0.5 mm slit to a third stage, pumped to 10^{-7} Torr. Next, an electron beam, with an impact ionization energy set at 70 eV, is incident on the molecular beam for a period of 3 μs. The resulting positive ions created by the interaction of the two beams are accelerated across a known potential (250 V between grid plates, 2.5 kV total potential). Since the potential and distance traveled are well known, the mass-to-charge ratio is found by measuring the "time of flight."

AB decomposition results in a significant amount of condensed-phase products. To identify and characterize condensed-phase species, an FTIR/KBr pellet technique was used. A small amount (~0.5 mg) of AB was heated at a known temperature for a known period of time in the CRT apparatus described above. The resulting condensed-phase products remaining on the metal foil were then mixed with ~150 mg of KBr powder. The resulting mixture was then pressed into a pellet. The pellet is placed inside a housing, purged with N_2, and aligned with the modulated FTIR beam. The same FTIR spectrometer acquires the transmissivity spectrum, where the spectrum for a pure KBr pellet serves as the background. In addition to examining the residue left on the metal foil after heating, a glass slide was used to collect products in the gaseous product stream which can easily condense out at room temperature. A diagram showing the position of the glass slide is pictured in 8. After being collected, the condensate is removed from the glass slide by grinding with KBr powder. The sample is then pressed into a KBr pellet, for later FTIR analysis.
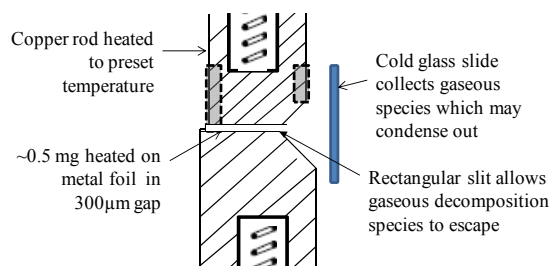
Figure 8 Diagram showing the position of glass slide for collecting condensate from gaseous decomposition products

Thermal analysis was conducted using a simultaneous TGA/DSC apparatus (Netzch STA-449 Jupiter), which has a silicon carbide furnace with a maximum temperature of 1550ºC and a maximum heating rate of 50 K/min. The samples were placed in alumina crucibles covered with thin alumina lids that had a small hole to release the evolved gases. Sample masses were approximately 2.5 mg for each test. The sample mass was limited by the amount of material swelling during decomposition.

The sample chamber, which is vacuum-tight, was evacuated and backfilled with an argon atmosphere prior to each measurement, and was continuously purged with argon during the experiments. A top-loading, low-drift balance with a resolution of 1 μg measures the change in sample mass. Two S-type thermocouples are attached to a platinum sample carrier, which holds both a reference and sample crucible, to measure heat flow from the sample. The onset melt temperatures of pure metal samples of indium, tin, zinc, aluminum and gold were used to calibrate the temperature measurements. Prior to each experiment, a baseline measurement is made to compensate for buoyancy and specific heat effects in the TGA and DSC measurements, respectively.

Figure 9 shows a plot of signal intensity for different mass-to-charge (m/z) ratios, as measured by CRT/ToF-MS. Also included in this figure are the species assignments corresponding to each mass-

to-charge ratio. The first species to appear in the signal are H_2^+ (m/z=2) and NH_3^+ (m/z=17), followed shortly after by m/z=28 attributed to either $NH_2{}^{10}BH_2{}^+$, $NH_2{}^{11}BH^+$, or $NH^{11}BH_2{}^+$. Subseqently, strong peaks are shown at m/z=27 and 29, which may correspond to $NH^{10}BH_2$ or $NH^{11}BH^+$ and $NH_2{}^{11}BH_2{}^+$, respectively. Mass-to-charge ratios of 27, 28, and 29 can all be attributed to the fragmentation spectrum of molecular H_2NBH_2. At significantly later times, signals at m/z=53, 80, and 81 are detected, suggesting the presence of borazine (c-$[NHBH]_3$). At a thermolysis temperature of 180°C, the AB is consumed very quickly indicated by the early decrease in the evolution of ammonia.
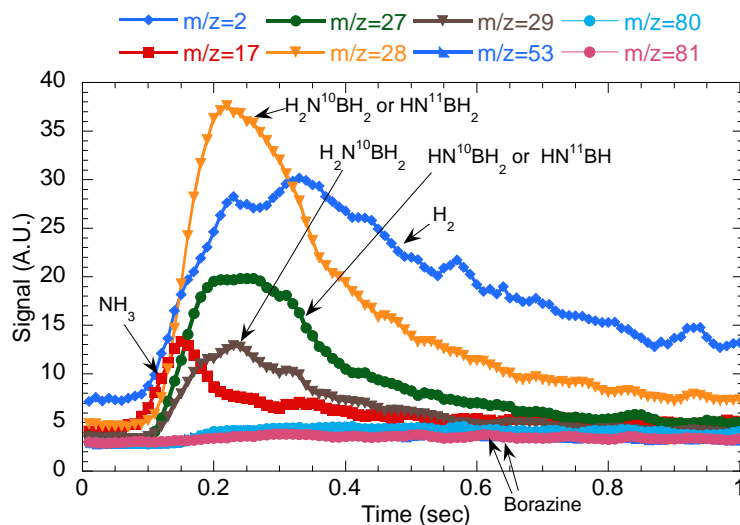
Figure 9: Mass to charge ratio signals for ToF-MS of decomposition products from AB at 180°C

Figure 10 shows a series of FTIR spectra from the CRT experiment at 160°C with 0.6 mg of AB. The first spectrum, taken at 650 ms, shows two very strong peaks at 965 and 930 cm^{-1} and some slightly weaker peaks at 1083 and 993 cm^{-1}, indicating the presence of ammonia (NH_3). In the second spectrum, taken at 750 ms, the ammonia peaks have increased in strength, and quite a few new peaks have also appeared. Peaks in the region of 3300-3500 cm^{-1} are indicative of N-H stretching frequencies and the peaks at 3479 and 3451 cm^{-1} are attributed to the asymmetric and symmetric N-H stretches of H_2NBH_2. The peaks from 2400-2600 cm^{-1} can be attributed to B-H stretching. The peaks at 2597 and 2493 cm^{-1} match well with the asymmetric and symmetric B-H stretching frequencies reported in the literature [52, 53]. Multiple peaks for each B-H stretching mode likely arise due to the presence of two stable boron isotopes (^{11}B and ^{10}B) in relatively high quantities. Likewise, the frequencies for B-N stretching can be attributed to peaks at 1368 cm^{-1} (^{10}B-N) and 1340 cm^{-1} (^{11}B-N), as they match well with data from the literature for the H_2NBH_2 spectrum [52]. The peak at 1625 cm^{-1} also matches well with values reported in the literature [52, 53], and it is attributed to -NH_2 scissoring.

22
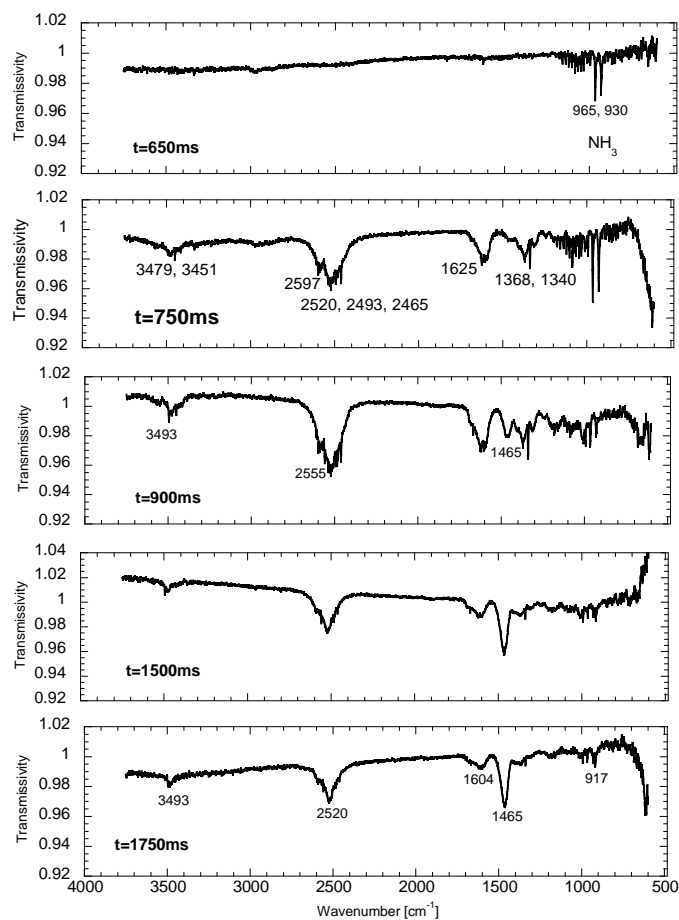
Figure 10: FTIR transmission spectra of the gaseous decomposition products from a 0.6 mg sample of AB heated to 160°C in the CRT experiment.
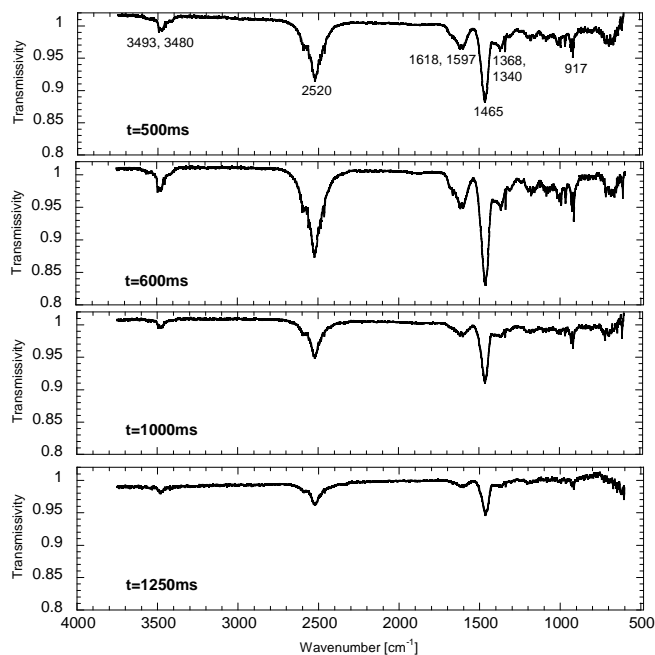
Figure 11: FTIR transmission spectra of the residue from AB pyrolysis at 160°C subsequently heated to 250°C in the CRT experiment

The third spectrum, taken at 900 ms, shows the ammonia peaks declining while the aforementioned H_2NBH_2 peaks stay at about the same intensity. New peaks are apparent in this spectrum at wavenumbers of 3493, 2555, and 1465 cm^{-1}, indicating the presence of a new substance. The intensity of the H_2NBH_2 peaks decreases in the subsequent spectra, and at 1750 ms, they have nearly vanished. The prominent peaks in the final spectra (3492, 2520, 1465, and 917 cm^{-1}) all correspond with the very strong peaks observed by Niedenzu *et al.* [54] for the gas-phase IR spectrum of borazine (c-(NH-BH)$_3$).

Figure 11 shows the FTIR transmission spectra of the gas-phase products resulting from the residue of the previously described experiment (0.6 mg sample of AB rapidly heated to 160°C) being rapidly heated to 250°C in the CRT experiment. The first spectrum shown, taken at 500 ms, has peaks which provide evidence that both aminoborane (H_2NBH_2) and borazine (c-(NH-BH)$_3$) are produced. The peaks at 1368 and 1340 cm^{-1}, also evident in the previous spectra, are attributed to the ^{10}B-N and ^{11}B-N stretches in H_2NBH_2. The very strong peak at 1465 cm^{-1} is attributed to B-N stretching in the borazine molecule. The feature at 2520 cm^{-1} is a combination of the N-H stretching peaks for both molecules, while the peaks at 3480 and 3493 cm^{-1} are attributed to the B-H stretching for H_2NBH_2 and borazine, respectively. A prominent peak attributed to -NH$_2$ symmetric bending of H_2NBH_2 is observed at 1618 cm^{-1}. The other strong peaks in the spectrum, at 1597 and 917 cm^{-1}, were previously observed in the FTIR spectrum of borazine [54]. The second spectrum in the sequence, taken 100 ms later, shows all the peaks in the spectrum growing in intensity. No significant new peaks are observed. Subsequent spectra taken at 1000 and 1250 ms show the peaks for H_2NBH_2 diminishing, followed by a decrease in the borazine peaks in the final spectra. It is of note that no peaks corresponding to ammonia appear in the spectra, suggesting that AB is not present in the residue.

Figure 12 shows a sequence of FTIR transmission spectra taken of the condensed-phase residue which remained on the foil after AB thermolysis in the CRT experiment. The spectrum labeled "0 sec" corresponds to unheated AB as received from Boroscience International. The subsequent spectra were acquired from the condensed-phase residue of decomposed AB after being heated for a known period of time. For all of the spectra in , the sample was heated at 140°C.

The absorption bands in the spectra from 3000-3500 cm^{-1} can be attributed to N-H stretching vibration. An expanded view of this region is shown in Figure 13. The peaks in the neat AB spectrum at

24

3253 and 3194 cm^{-1} correspond well with previously reported wavenumbers for asymmetric and symmetric N-H stretching for AB in a KBr pellet [55]. After heating at 140°C for 4 sec, the original peaks appear to still be present, with the symmetric N-H stretch slightly shifted. However, a new peak has appeared at 3305 cm^{-1}. After further heating, the peaks from the neat AB diminish compared to the new feature, resulting in a broad absorption curve with a peak at 3291 cm^{-1} after 12 sec. Previous studies have observed absorption peaks attributed to N-H stretching in polymers amino-borane in this range (3300 cm^{-1} by Komm *et al.* [56] for $(H_2NBH_2)_x$, 3301 cm^{-1} by Boddeker *et al.* [57] for $(H_2NBH_2)_5$). For amine boranes, the frequency of N-H vibration increases with increasing B-N bond order, as Frueh *et al.* [48] have noted. This provides evidence that the AB has dehydrogenated and formed PAB.
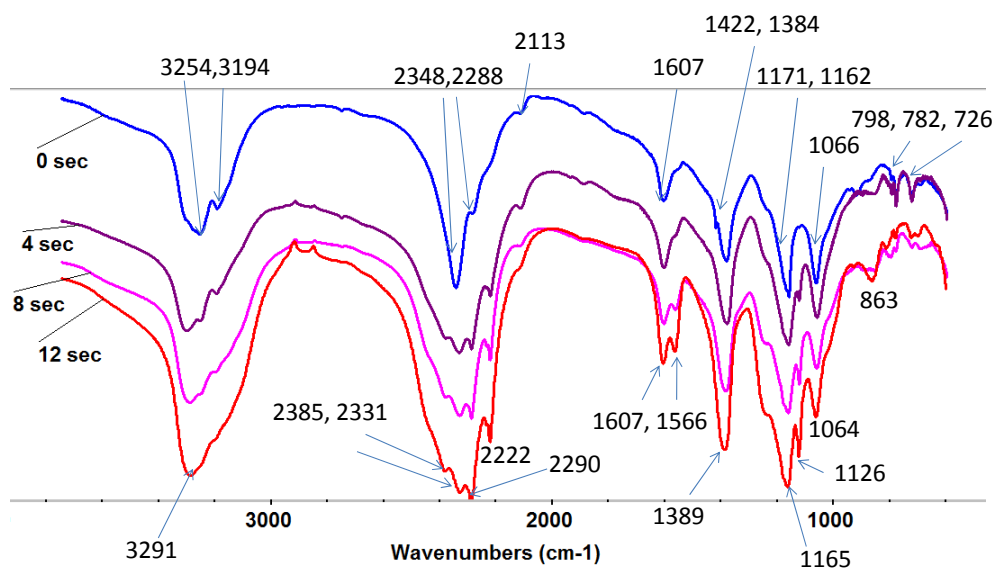
Figure 12: Overlayed time sequence of FTIR spectra from condensed phase AB residue from CRT experiments at 140°C. Residue was mixed with KBr and pressed into a pellet.
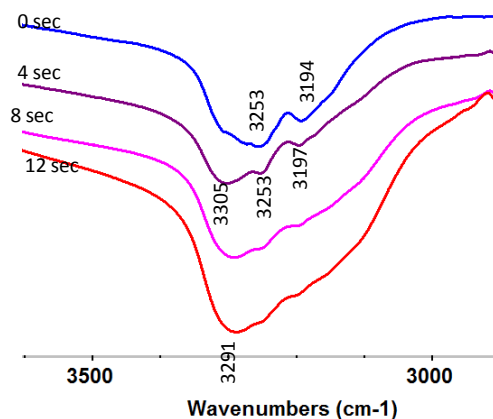
Figure 13: N-H stretching frequencies in AB and AB residue for various heating times at 140°C

Figure 14 shows the absorption bands attributed to B-H stretching between 2000 and 2500 cm^{-1}. For the neat AB, asymmetric and symmetric B-H stretching frequencies are observed at 2348 and 2288 cm^{-1}, slightly higher than those reported in the literature (2330 and 2280 cm^{-1} [55]). After just 4 sec of

heating, the spectral features have changed significantly in this region. New peaks are observed at 2385, 2331, 2290, 2236, and 2222 cm⁻¹. These peaks continue to make up the spectra after 8 and 12 sec of heating. These peaks seem to correspond best with those reported by Baumann *et al.* [46] for $(BNH_x)_z$ polymer (decomposition products of $(H_2NBH_2)_x$), suggesting the AB has undergone more than one H_2 elimination.
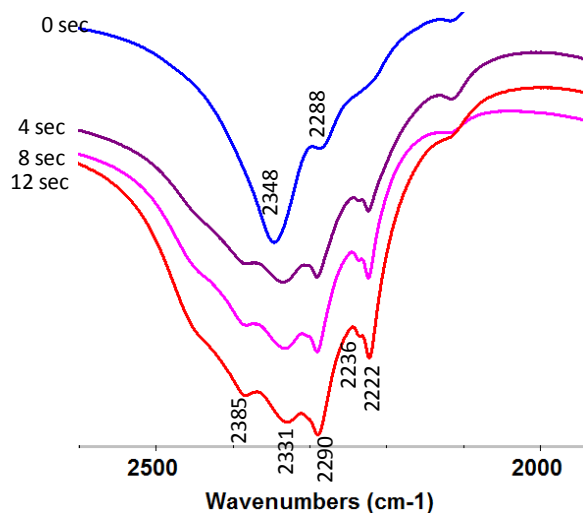
Figure 14: B-H stretching frequencies in AB and AB residue for various heating times at 140°C
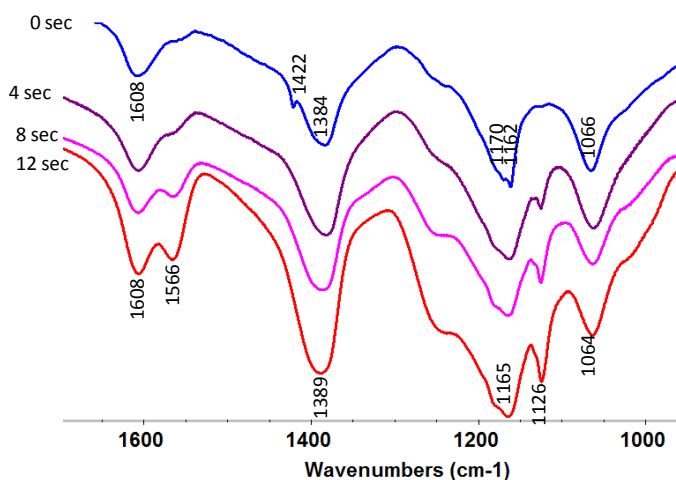
Figure 15: Fingerprint region of the FTIR transmission spectrum for AB and AB residue from samples heated at 140°C for varying amounts of time

Figure 15 shows an enlarged view of the FTIR spectrum from 1650-1000 cm⁻¹, in which the upper part of what is often referred to as the "fingerprint" region. In this region, there is usually present the fundamental vibrational modes due to molecular bending. The neat AB shows peaks at 1608 cm⁻¹, and 1384 cm⁻¹, which correspond well with values reported in the literature for NH_3 deformation [55, 58]. The peak at 1422 cm⁻¹ in the neat AB has not been reported in the literature, but is tentatively attributed to N-H rocking. The peaks at 1170 and 1162 cm⁻¹ closely match wavenumbers in the literature for BH_3

26

deformation [55, 58], as does the peak at 1066 for the NBH rock in AB. Spectra of the AB residue all show a peak at 1566 cm^{-1}, which closely matches the spectral location reported by Boddeker *et al.* for NH$_2$ deformation in the cyclic (H$_2$NBH$_2$)$_2$ [57]. The peak at 1422 cm^{-1} vanishes when the AB is heated, and the peak at 1384 cm^{-1} shifts to the left and is located at approximately 1389 cm^{-1}. It is probable that this peak is no longer related to NH$_3$ deformation, but instead can be attributed to B-N stretching, which occurs near 1400 cm^{-1} for double B-N bonds [46, 48, 57]. The features in neat AB at 1170 and 1162 cm^{-1} are broadened after heating and result in a peak shifted to 1165 cm^{-1} after 12 sec. A peak at 1126 cm^{-1} appears upon heating and grows relative to the other peaks at longer heating time. This peak could be related to BH$_2$ bending, and a similar peak was reported by Boddeker *et al.* [57] for cyclic (H$_2$BNH$_2$)$_4$. Lastly, it appears that the peak attributed to NBH rocking is still present after heating, and after 12 sec it has shifted slightly to 1064 cm^{-1}. It should be noted that some small shifts in band location may be attributed to changes in the association of molecules in the condensed phase.
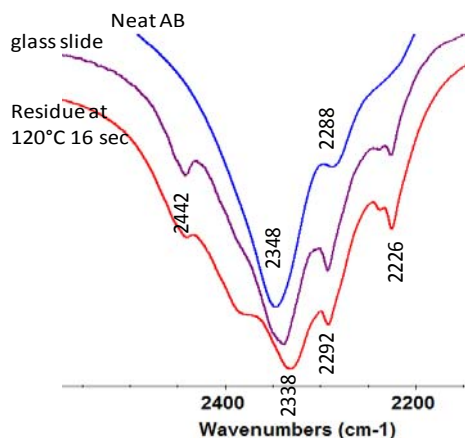
Figure 16: FTIR transmission spectrum showing B-H stretching frequencies measured from neat AB, condensate collected on a glass slide, and residue removed from sample foils after 16 seconds at 120°C
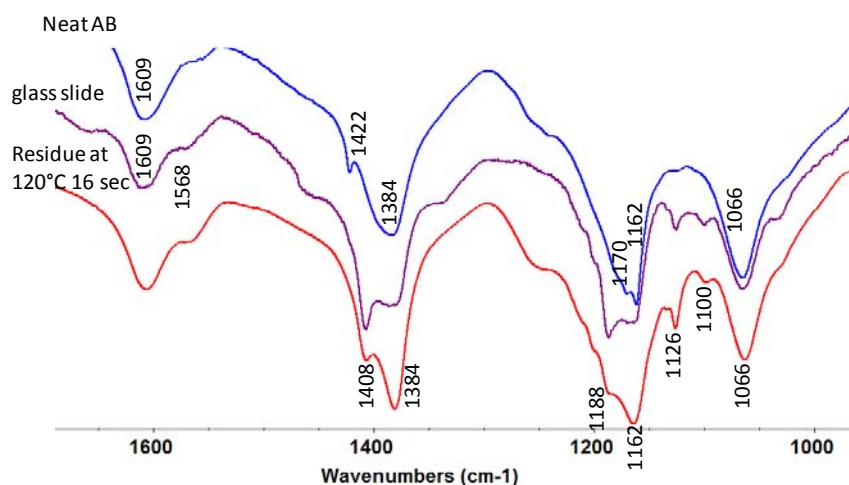
Figure 17: FTIR transmission spectrum showing fingerprint region for neat AB, condensate collected on a glass slide, and residue removed from sample foils after 16 seconds at 120°

27

Figure 16 shows the FTIR spectrum in the B-H stretching region for the condensate collected on the glass slide, as compared with neat AB and the residue from rapid thermolysis at 120°C for 16 seconds. The peaks in the condensate correspond closely with those in the residue, especially those at 2226, 2292, and 2442 cm^{-1}. The shoulder which appears in the residue around 2380 cm^{-1} is notably absent in the condensate, and the strongest absorption peak is shifted to higher wavenumbers, closer to that found in the neat AB. Figure 17 shows the fingerprint region for the condensate, neat AB, and thermolysis residue from heating at 120°C for 16 seconds. The spectrum corresponding to the condensate again matched well with the condensed phase residue of AB after heating at 120°C in this region. As in the thermolysis residue , the spectrum of the condensate showed the shifting of the N-H rocking absorption peak at 1422 cm^{-1} to 1408 cm^{-1}. Both of these spectra also showed the appearance of peaks at 1568 cm^{-1}, 1188 cm^{-1}, and 1100 cm^{-1}. Many of the peaks from neat AB are still observed in both the residue and condensate. These results suggest that the condensate has roughly the same composition as the condensed phase residue at early times. They both appear to be comprised of some AB along with dehydrogenated amino-borane polymers. The implications of this result are that H_2NBH_2 in the gaseous products will readily condense out on a cold surface and begin to polymerize. Also, this result suggests that some AB will sublimate into the gas phase, but it decomposes too fast to be observed, even by the fast diagnostics used in the gas phase CRT experiments.
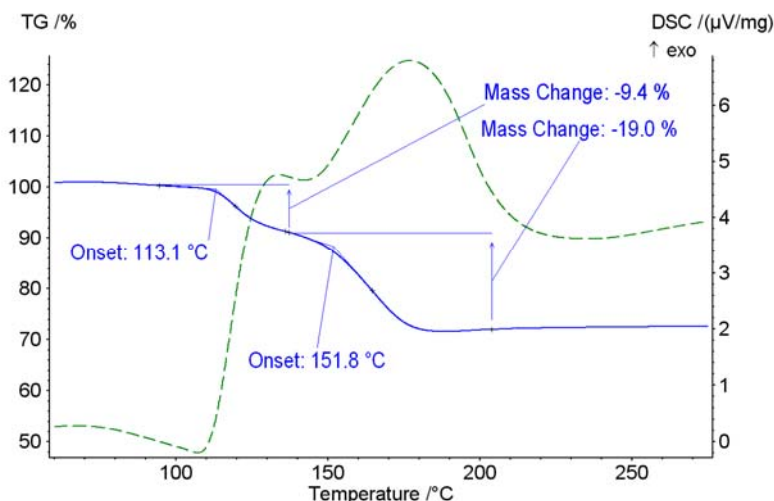
Figure 18: Thermo-gravimetric and differential scanning calorimetry data for AB heated at a rate of 20 K/min in an Argon atmosphere

Figure 18 shows data typical of a TGA/DSC experiment with ammonia borane. The case plotted in is from a test with a heating rate of 20 K/min. Two distinct mass losses appear in Figure 18. The first, with an onset temperature of approximately 113ºC, corresponds to a mass loss of 9.4 percent of the initial mass. The second mass loss corresponds to 19.0 percent of the initial mass, and has an onset temperature of roughly 152ºC. AB samples were heated up to 1400ºC; however, the signal output from either the TGA or DSC instrument do not reveal any noteworthy changes above 200ºC. This is inconsistent with the work of Frueh *et al.* [48], who report a slow mass loss starting at 1170°C. The shape of the mass loss curve corresponds well with those reported by Baitalow *et al.* [45] for lower heating rates (1 and 5 K/min). Also, in agreement with the work of Baitalow *et al.*, the percent mass loss increases with increased heating rate. is a scatter plot of the percent mass loss as a function of heating rate with data from this study and Baitalow *et al.* [45]. These data show that mass loss is nearly logarithmic function of heating rate over the range of 2-50 K/min.

To build on previous studies of AB decomposition at low heating rates [44, 45, 46, 48], we have investigated decomposition at high heating rates. Knowledge of decomposition pathways at high heating rates is important for studying the combustion of propellant ingredients. The TGA mass loss data shows that the mass loss continues to increase logarithmically with heating rates up to 50 K/min. The increased mass loss is presumable due to a greater amount of condensable or water-soluble decomposition products as observed by Baitalow *et al.* [45] for lower heating rates.

CRT/FTIR/ToF-MS experiments, where samples are heated at rates of approximately 2000 K/sec to an isothermal condition, were performed to further investigate the effect of high heating rates on the decomposition products. The data from the ToF-MS reveal that di-hydrogen (H_2), ammonia (NH_3), monomeric aminoborane (H_2BNH_2), and borazine (c-[NHBH]$_3$) emerge into the gas phase. The FTIR transmission spectroscopy measurements support the presence of these species. Aside from ammonia, Baitalow et al. [45] identified all these species at low heating rates. Ammonia is likely produced from the cleavage of the B-N bond in AB, as shown in Eq. . This is a coordinate bond, which has a relatively weak dissociation energy (31.3 kcal/mol [59]). The cleavage of this bond has been shown to be important at low temperatures in MD simulations [60]. After careful examination of the acquired FTIR spectra, borane (BH_3) has not been detected in the gas-phase. This is likely due to its high reactivity, suggesting that it takes part in condensed-phase reactions rather than escaping into the gas phase. By contrast, the fairly un-reactive NH_3 much more readily escapes the solid or liquid matrix.

$$NH_3BH_3 \rightarrow NH_3 + BH_3$$

(11)

The production of gaseous ammonia at high heating rates may be part of the reason for increase mass loss at high heating rates. A larger effect is likely related to the rate of formation of high molecular weight polymers. As noted by Wolf *et al.* [44], the condensed-phase products following the first hydrogen release are mostly polymeric aminoborane or PAB ([NH$_2$BH$_2$]$_x$). With low temperature isotherms (>90°C) or low heating rates, the AB molecule releases an H_2 molecule prior to its melting temperature, and the resulting NH_2BH_2 molecule is able to polymerize with like molecules. Stowe *et al.* [47] have suggested this process is initiated by the formation of the ionic compound DADB. The activation energy for such polymerization processes is typically negative. Thus, for a slow heating rate, where temperature will remain lower for longer times, polymerization is enhanced. At higher heating rates, AB will melt prior to decomposing. Furthermore, since heating is much more rapid than the reaction, the decomposition will occur at a higher temperature, where polymerization is slower and less favorable thermodynamically. As the time scale for polymerization increases, more monomeric aminoborane will be able to diffuse into the gas phase, therefore increasing the amount of mass lost to the gas phase at higher heating rates and higher temperatures. The collection of condensate with the glass slide shows that gaseous monomeric aminoborane will condense out and polymerize on a cold surface. The spectra of the condensate also show evidence that some AB may be present, even though it is not detected with the fast gas phase diagnostics. This suggests that some AB may sublime, but it is rapidly converted to H_2NBH_2 and H_2 in the gas phase.
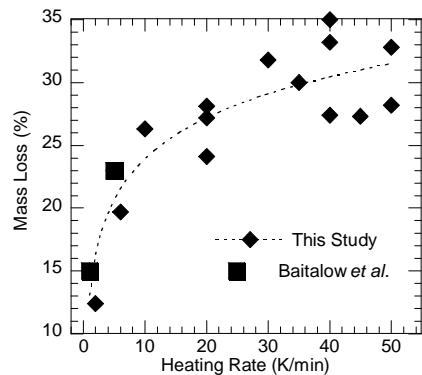
Figure 19: Percent mass loss versus heating rate for TGA experiments with AB

Hydrogen elimination from PAB has been reported to occur above 130°C [46], and condensed phase polyimino borane or PIB ([HNBH]$_x$) is known to be formed as a result. Furthermore, the gas phase FTIR measurements in this study show that monomeric aminoborane and borazine evolved from the residue of AB decomposition, likely consisting of PAB and PIB. The pathways for the conversion of PAB and PIB to borazine have been studied by Nutt and McKee [61]. Figure 20 shows a schematic of the pathways for AB decomposition. As indicated, the formation of PAB is favored at low heating rates, while higher heating rates favor gaseous monomeric aminoborane.
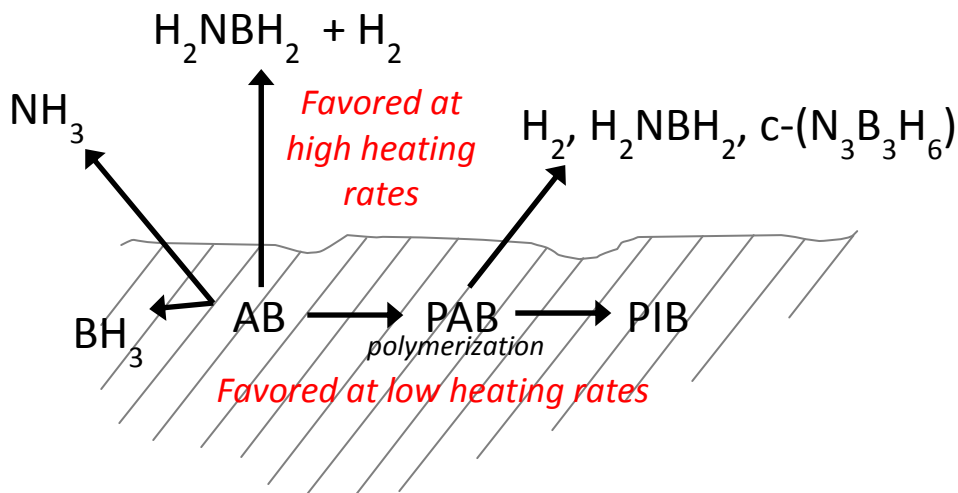
Figure 20: Schematic of condensed phase thermolysis of AB and evolved gas phase products.

Since propellant ingredients will experience rapid heating in practical applications, it is important to study the decomposition pathways under similar heating rates, as these processes can be rate dependent. Confined rapid thermolysis was used to investigate the decomposition of AB at high heating rates. In this experiment, AB samples were rapidly heated to a preset temperature level, where decomposition was examined under isothermal conditions. This type experiment differs from that of TGA/DSC, where the heating rate is slow and the temperature varies continuously. Studies of the gas-phase products by FTIR spectroscopy and by ToF-MS show the evolution of H_2 and NH_3 followed a short time after by H_2NBH_2. At later times, borazine (c-$N_3B_3H_6$) is observed. Aside from NH_3, these products have all been previously observed to evolve from decomposition at low heating rates [45]. While the

amount of hydrogen evolved has been shown to remain the same, the total mass of evolved products increases when the sample is more quickly heated to a temperature above its decomposition point. Condensate collected on a cold glass slide in the stream of gaseous decomposition products has an FTIR spectrum with matches closely with that of polymeric aminoborane ($[H_2NBH_2]_x$).

III.   Modeling and Simulation of Thermo-Chemical Behavior of Nano-Energetic Materials (Georgia Tech)

A.   Molecular Dynamics Simulations of Physicochemical Behavior of Aluminum, Nickel, and Nickel-Coated Nanoaluminum Particles

Aluminum particles are extensively used in many propulsion and energy-conversion applications, due to their favorable energetic properties [62]. They are covered by an amorphous oxide layer, which is typically 0.5-4 nm thick [63].The specific thickness of the oxide layer depends on the temperature of the particle and the duration of exposure to the oxidizing environment. When the particle is exposed to the oxidizing gas for a sufficient period, the oxide layer thickness saturates at a value of 4 nm [64]. The oxide layer protects the particle from further attack by the oxidizer molecules. Aluminum particles with diameter greater than 100 μm ignite only upon melting of the oxide layer at 2350 K [65]. This results in a long ignition delay and a slow rate of energy release. It is thus desirable to reduce the ignition temperature of micron-sized aluminum particles.

The formation of the oxide layer on aluminum particles can be significantly inhibited by applying transition metal coatings, which have higher melting points than the aluminum [5]. For example, the bulk melting point of nickel is 1728 K. Foley et al. [66] synthesized nano-aluminum powders by thermal decomposition of an alane-adduct solution in the presence of a titanium catalyst under an inert atmosphere. The resulting material was used to reduce complexes of gold, nickel, palladium, and silver. The reduction process yielded nano-aluminum particles coated with transition metals. Typically, an oxide layer of the transition metal is formed, which can have thickness on the order of few nm [66-67]. Among all transition metals considered in Foley et al.'s study, nickel resulted in the highest active aluminum content. Encapsulation of aluminum particles with a nickel shell results in lower ignition temperatures, due to inter-metallic reactions between aluminum and nickel atoms [68]. For example, the ignition temperature of a 2.38 mm aluminum particle in air decreases from 2350 to 1313 K when the oxide layer is replaced with a nickel coating. Temperature runaway is also observed in inert environments [68]. The substitution of a nickel coating for the oxide coating increases the flame speed of an aluminum particle dust in air by a factor of 1.5-4 [69]. Nickel-coated aluminum particles can potentially be employed to manufacture nickel aluminides (Ni_xAl_{1-x}), which are attractive for use in aircraft turbines due to their good strength characteristics, excellent corrosion and oxidation resistance, and high melting points [70]. A better understanding of its thermo-chemical behavior is, thus, helpful for propulsion and material synthesis applications.

Nano-sized particles have unusual energetic properties due to their high percentage of surface atoms and the excess energy associated with these atoms [71-73]. As the particle size decreases from 30 to 3 nm, the percentage of surface atoms increases from 5 to 50 % [74]. The melting temperature of a nano-aluminum particle increases from 473 K at 2 nm to a bulk value of 937 K at approximately 8 nm [75]. The ignition temperature can be as low as 933 K, possibly due to polymorphic phase transformations in the oxide layer and/or melting of the aluminum core [63,76]. The oxide layer, however, occupies a significant portion of the particle mass at nano-scales. For example, a 38 nm aluminum particle has ~47.5 wt. % oxide [77]. For combustion applications, therefore, it is desirable to replace the oxide coating with such favorable metallic coatings as nickel. Nickel atoms can participate in oxidation and intermetallic reactions, thereby resulting in a significant reduction in the ignition delay.

Molecular dynamics (MD) simulations can be used to provide insight into the melting and ignition characteristics of nano-scale materials. Puri and Yang [75] performed MD simulations to analyze the effect of particle size on melting of nascent aluminum particles. The thermo-mechanical behavior of oxide coated aluminum particles has also been analyzed [78]. Molecular dynamics simulations on nickel-coated aluminum particles have thus far, however, been limited. Most efforts were made to study the possibility of fragmentation of the shell caused by core melting at a fixed core/particle size [79, 80], with little attention paid to diffusion and inter-metallic reactions [80, 81].

Systematic studies of the effect of particle size on the physiochemical processes after melting of the core are yet to be performed. In the present study, the thermochemical behavior of nickel-coated aluminum particles is investigated via MD simulations over a wide range of temperatures to characterize melting, diffusion, and inter-metallic reactions. The core diameter of the particles of interest is in the range of 3-12 nm, and shell thicknesses of 0.5, 1, 2 and 3 nm are considered. Special attention is paid to quantify the effect of the core diameter and nickel shell on relevant physiochemical phenomena.

In the present study, both isobaric-isothermal (NPT) and isochoric-isoenergetic (NVE) ensembles are employed. NPT ensemble is used to study the thermochemical behavior of the particle in the presence of external heating at a constant pressure condition, while NVE ensemble is used to investigate self-heating of the particle due to inter-metallic reactions under adiabatic conditions. In NPT ensemble, a system of N atoms is coupled to an external source by introducing additional variables into the Lagrangian. Assuming that atoms behave as classical point-like masses, the Lagrangian, L, is expressed as

$$L_{NPT} = \sum_i \frac{m_i s^2 V^{2/3} \dot{q}_i^2}{2} - U\left(V^{1/3} q_i\right) + \frac{M\dot{V}^2}{2} - PV + \frac{Q\dot{s}^2}{2} - gk_B Tlns, \qquad (12)$$

where M is a constant fictitious mass associated with the volume of the system, m the mass of the atom, q_i the generalized coordinate, V the volume, treated as a dynamic variable, P the pressure, U the potential energy, T the temperature, Q the inertia factor, g a parameter, k_B the Boltzmann constant, and s the degree of freedom of the thermostat. In this method, volume is treated as a dynamic variable [82] and the parameter s controls heat exchange between the system and the reservoir [83]. Substituting the Lagrangian in the Euler-Lagrange equation [23], the equations of motion take the form

$$M\ddot{V} = -P + \frac{s^2}{3V}\left[V^{2/3}\sum_i m_i\dot{q}_i^2 - V^{1/3}\sum_i F_i q_i\right],$$

$$m_i\ddot{q}_i = \frac{V^{-1/3}F_i}{s^2} - \frac{2m_i\dot{V}\dot{q}_i}{3V} - \frac{2m_i\dot{s}\dot{q}_i}{s},$$

$$Q\ddot{s} = sV^{2/3}\sum_i m_i\dot{q}_i^2 - \frac{gk_B T}{s}, \qquad (13)$$

where $\dot{q}_i$ and $\ddot{q}_i$ denote the first-order and second-order derivatives of q_i with respect to time, and F_i is the net force on atom i. In NVE ensemble, the Lagrangian is the difference between the kinetic and potential energies of the set of atoms. The resulting equation of motion is given by

$$m_i\ddot{q}_i = -\frac{\partial U}{\partial q_i}. \qquad (14)$$

The above system of equations is numerically integrated using a fifth-order predictor-corrector algorithm. The time step is chosen as 1 fs because the time scale of vibration of atoms is of the same order. Negligible improvement in the model results is obtained when the time step is reduced from 1 to

0.1 fs. The heating rate is another important adjustable parameter. Shibuta and Suzuki [85] analyzed the effect of the cooling rate on the solidification of metal nano-particles using MD simulations. The solidification temperature decreased with increasing cooling rate. In the present work, a parametric study was conducted to determine the optimum value of the heating rate in the range 10^{-3}-10^{-1} K/fs. The result is shown in Fig. 21. The time step places restriction on the minimum value of the heating rate. The analysis reveals that a heating rate lower than 10^{-2} K/fs increases the total computational time dramatically with only little change in the model results, while a higher value leads to substantially different results. As a result, a heating rate of 10^{-2} K/fs is adopted in the present study.
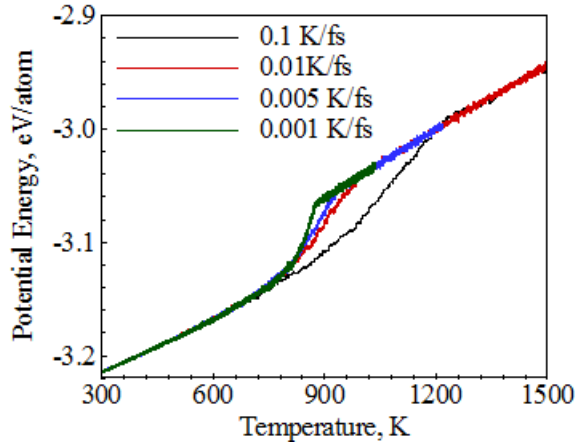
Figure 21: Variation of potential energy of 7 nm (10976 atoms) aluminum particle with temperature at different heating rates

To calculate macroscopic properties of the system from the positions and momenta of all atoms, an ensemble average is required [84]. The pressure is calculated using the virial equation of state, as a function of temperature and forces experienced by all the atoms [86].

$$P = Nk_BT + \left\langle \frac{1}{3}\sum_{i=1}^{N} r_i \cdot F_i \right\rangle, \tag{15}$$

where r_i is the position vector of atom i. The melting point of the system is identified based on the variations in the potential energy, Lindemann index, thermal displacement, and translational-order parameter. The Lindemann index, δ, is a measure of the root-mean-square fluctuations of the inter-atomic distance, and is given by [87]

$$\delta = \frac{2}{N(N-1)}\sum_{i<j} \frac{\sqrt{\left\langle r_{ij}^2 \right\rangle_t - \left\langle r_{ij} \right\rangle_t^2}}{\left\langle r_{ij} \right\rangle_t}. \tag{16}$$

It is expected to increase abruptly during melting. The translational-order parameter, λ, is expressed as [88]

33

$$\lambda = \frac{1}{N}\sqrt{\left(\sum_{i=1}^{N}\cos(k.r_i)\right)^2 + \left(\sum_{i=1}^{N}\sin(k.r_i)\right)^2},$$

$$k = \left(\frac{(2N)^{1/3}\pi}{L}\right)(-1,1,1), \tag{17}$$

where k is an arbitrary vector of the lattice and L is the side length of the simulation domain. In solids, atoms simply translate about their lattice positions, and hence, there is a perfect order in the crystal. Such order, however, disappears in a liquid state, and the corresponding translational-order parameter is reduced by an order of magnitude. The thermal displacement is defined as

$$\delta_{t,i} = \sqrt{\left(r_i - r_{0,i}\right)^2}, \tag{18}$$

where the subscripts i and 0 refer to atom i and the initial state, respectively. Upon melting, the aluminum atoms diffuse into the nickel shell. The onset of diffusion is marked by the sudden increase in the core radius, r_c [79]

$$r_c = \sqrt{\frac{5}{3N}\sum_{i=1}^{N_{Al}}\left(r_i - r_{cm}\right)^2}, \tag{19}$$

where r_{cm} is the position vector of the center of mass.

Potential Function

To close the formulation, the potential energy of the system of atoms needs to be specified. For metals, the majority of the potential functions are based on the embedded atom method [89]. In this method, the energy needed to embed an atom in the electron gas is included to capture the physics of metallic bonding. One such potential function, which is formulated by Cleri and Rosato [90], has been fitted to the structural and thermodynamic properties of bulk aluminum and nickel. It takes the following form:

$$U = \sum_{i=1}^{N}\left(\sum_{j\neq i}V_{ij} - \sqrt{\sum_{j}\rho_{ij}}\right), \tag{20}$$

where V is the pair-potential function and ρ the electron density function. The first term describes the electrostatic interactions between the atoms, while the second term accounts for the energy needed to embed an atom in the electron gas. The pair-potential and electron density functions are expressed as

$$V_{ij} = A_{\alpha\beta}\exp\left(-p_{\alpha\beta}\left(\frac{r_{ij}}{r_{\alpha\beta}^0}-1\right)\right),$$

$$\rho_{ij} = \xi_{\alpha\beta}^2\exp\left(-2q_{\alpha\beta}\left(\frac{r_{ij}}{r_{\alpha\beta}^0}-1\right)\right). \tag{21}$$

Table 2 Parameters for potential function [91, 92]

	Ni-Ni	Al-Al	Ni-Al
A(eV)	0.0376	0.1221	0.0597
ξ (eV)	1.0700	1.3160	1.2898
p	16.9990	8.6120	15.714
q	1.1890	2.5160	1.1550
r_0 (Å)	2.4910	2.8637	2.5001

The parameters in the potential function are given in Table 2 [91, 92]. Previous studies indicate that the potential function can predict the structure, phase stability, and thermodynamic properties of Ni-Al alloys (especially, B2-NiAl and Ni_3Al) with reasonable accuracy. Furthermore, considerable success has been achieved in simulations thermal behaviors of aluminum particles coated with Ni and Ni_3Al using this potential function. As a result, it is employed in the present study.

Pure Aluminum and Nickel

The theoretical framework is employed to calculate the structural and thermodynamic properties of aluminum and nickel. An FCC lattice is adopted to calculate the initial position vectors for a known number of atoms. For bulk materials, a periodic boundary condition is enforced in all the three spatial directions. A free-surface boundary condition is, however, prescribed for nano-particles. The crystal is allowed to equilibrate at 300 K prior to the heating simulation.

Bulk Materials

The properties of surface-free bulk systems of aluminum and nickel are first treated. The lattice constant and cohesive energy are calculated by equilibrating the crystal in an NVE ensemble. To determine the melting point and latent heat of melting, the crystal is heated externally in an NPT ensemble. Table 3 shows calculated values of the cohesive energy, lattice constant, and latent heat of melting and compares them with experimental data. The discrepancy is less than 2 %, demonstrating the accuracy of the potential function. Figure 22 shows the melting of 4000-atom bulk aluminum in vacuum. Melting is observed at 1060 K, at which point sharp variations occur in the translational-order parameter and Lindemann index. Such a trend is characteristic of the structural melting phenomenon, which is observed for surface-free materials [96]. Note that the fluctuations that are typically observed in MD simulations decrease

Table 3 Cohesive energy, lattice constant, and latent heat of melting of bulk materials

	Aluminum		Nickel	
	Model	Experiment[93-95]	Model	Experiment[93-95]
E_c (eV/atom)	-3.337	-3.340	-4.437	-4.435
a (Å)	4.048	4.050	3.491	3.520
ΔH_m (kJ/mol)	10.610	10.470	17.360	17.160
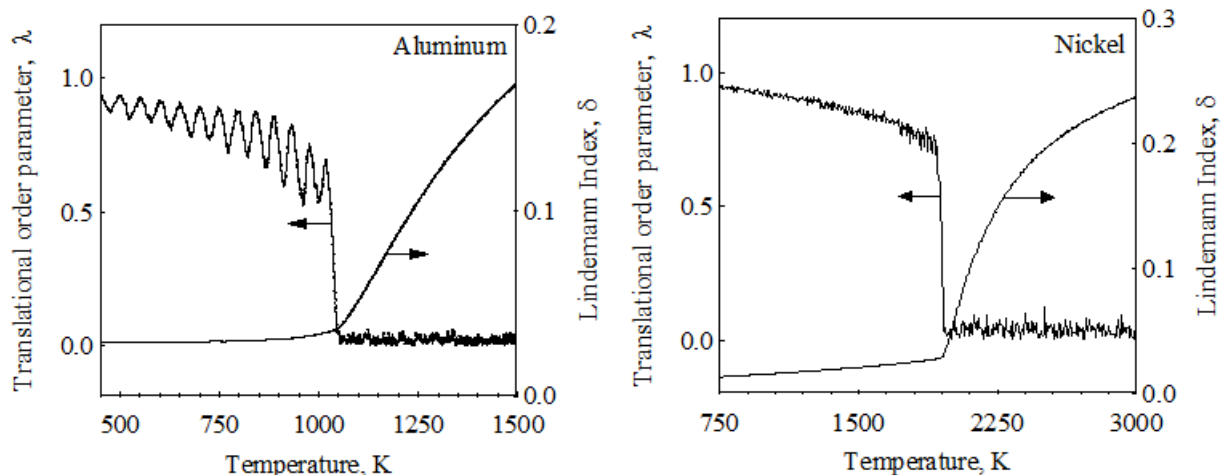
Figure 22 Translational order parameter (λ) and Lindemann index (δ) as a function of temperature showing the melting of bulk aluminum and nickel in vacuum

with increasing number of atoms. The system is superheated above the experimental melting point of bulk material by 127 K, which can be attributed to the absence of a nucleation site for melting. The structural melting point is typically greater than the thermodynamic counterpart by 20 % [96,97]. The resulting asymptotic value of the melting temperature of aluminum particles is 883 K, which differs from the experimental value by about 5 %. A similar pattern is observed for bulk nickel, as shown in Fig. 22. It melts at 1950 K, which is higher than the thermodynamic melting point by 222 K. The asymptotic heterogeneous melting point of 1625 K is 6 % lower than the experimental value.

Nascent Nano Particles

　　　The melting of nanoscale particles is examined over a size range of 1.5-12 nm. Figure 23 shows the variation with temperature of the potential energy and Lindemann index of a 7 nm aluminum particle consisting of 10976 atoms. Melting occurs at 810 K. For a particle, the surface acts as a nucleation site for phase transition and the melting front propagates to the interior regions of the core. Hence, the phase change is manifested by a gradual increase in the
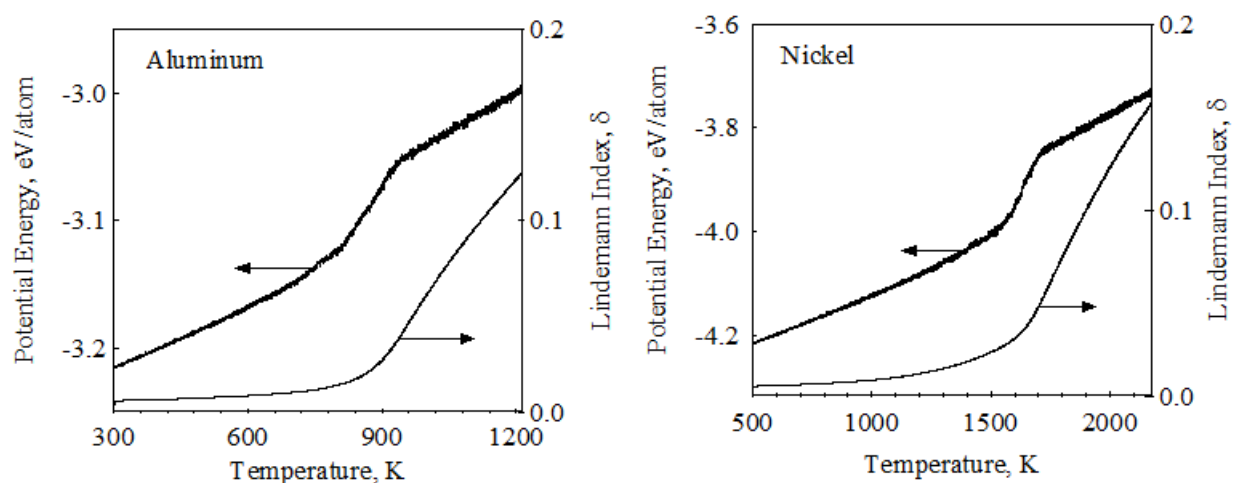
Figure 23 Potential energy and Lindemann index (δ) as a function of temperature showing the melting of 10976-atom aluminum (7 nm) and nickel (6 nm) particles in vacuum

36
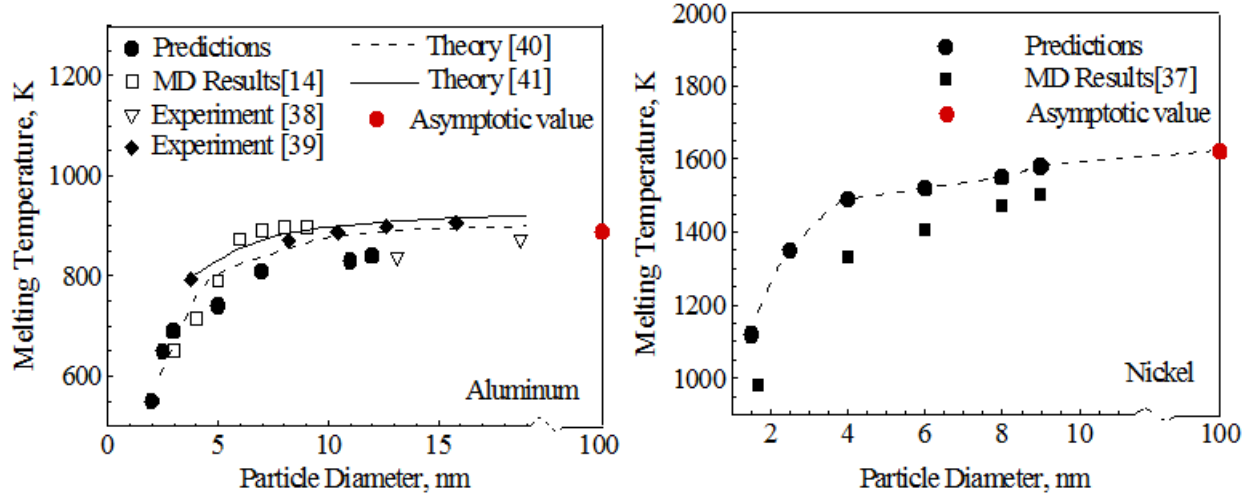
Figure 24 Effect of particle size on melting of aluminum and nickel particles

properties, as opposed to the abrupt changes found in a bulk material. A similar trend is observed for the nickel particle, except that melting takes place at a higher temperature of 1540 K. Figure 24 shows the effect of particle size on the melting of aluminum and nickel at nano-scales. It also shows comparison with the results of previous MD simulations [75,98], experiments [99,100], and theoretical studies [101,102]. The theoretical curve in Ref. [40] corresponds to the case in which only the Ginzburg-Landau (GL) equation is employed. For nano-sized particles, surface pre-melting phenomenon is observed. Since the percentage of surface atoms increases with decreasing particle size, a larger particle melts at a higher temperature. Note that the dependence of the melting point on particle size becomes much weaker for diameters greater than 5 nm. Eckert et al. [99] synthesized nanocrystalline aluminum powders by mechanical attrition in argon, hydrogen, and oxygen atmospheres. A similar reduction was observed in the melting point with decreasing grain size. It is rather surprising that the predicted values exhibit excellent agreement with experimental data, since the model under-predicts the bulk melting point by 5 %. This may be attributed to the fact that the heating rates in the simulations are orders of magnitude higher than those employed in the experiments [103]. Furthermore, the theoretical and experimental melting points increase more gradually than those in MD simulations. This is completely justified, since the percentage of surface atoms in the particle follow a similar trend. Qi et al. [98] calculated the melting points of nickel particles as a function of particle size using the quantum-corrected Sutton-Chen potential. As can be seen, the Cleri-Rosato potential function offers more accurate values of the melting point of nickel particles.

Nickel-Coated Aluminum Particles

The theoretical model is also employed to analyze the thermo-chemical behavior of nickel-coated aluminum particles. Figure 25 shows the initial structure of nickel-coated aluminum particle with a core diameter of 12 nm and shell thickness of 1 nm. A spherical nickel particle of known dimension is first generated. A spherical void is then created in the interior of the nickel particle to accommodate the aluminum core. The resulting particle is equilibrated at 300 K prior to the heating simulation. Table 4 shows the values of the core diameter (d_c), shell thickness (δ_s), total number of atoms (N), and number of aluminum atoms (N_{Al}). The core diameter varies in the

37
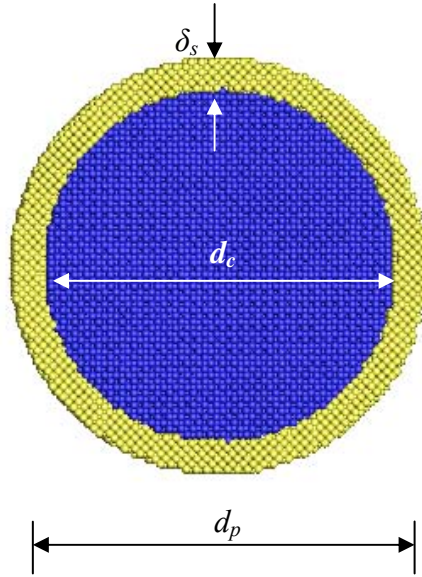
Figure 25 Initial crystal structure of nickel-coated aluminum particle ($d_p = d_c + 2\delta_s$)

range of 3-12 nm, and three different shell thickness of 0.5, 1, 2, and 3 nm are considered. The aluminum atomic fraction increases with increasing core size and decreasing shell thickness.

Table 4 Configuration of nickel coated nano-aluminum particles

d_c, nm	δ_s, nm	N	N_{Al}	X_{Al}
3	0.5	2909	874	0.30
3	1.0	7187	874	0.12
3	2.0	17440	874	0.05
3	3.0	37065	874	0.02
5	1.0	15496	4081	0.26
6	1.0	20914	6380	0.30
6	0.5	12760	6380	0.50
8	1.0	39435	15504	0.39
12	1.0	103737	53752	0.52
12	2.0	169899	53752	0.31
12	3.0	254614	53752	0.21

Baseline Simulation

To facilitate detailed discussion on the thermochemical behavior of nickel-coated aluminum particles, a particle with a core diameter of 12 nm and shell thickness of 1 nm is first considered. Figure 26 shows the variation of the Lindemann index and potential energy of the core with temperature. Melting of the core is characterized by the change in the parameters, beginning at 1000 K. The predicted melting point is higher than that of a nascent particle, which is approximately 880 K. It is, however, lower than the structural melting point of bulk aluminum, 1060 K. The latter represents the upper limit for the core melting point, since it is the
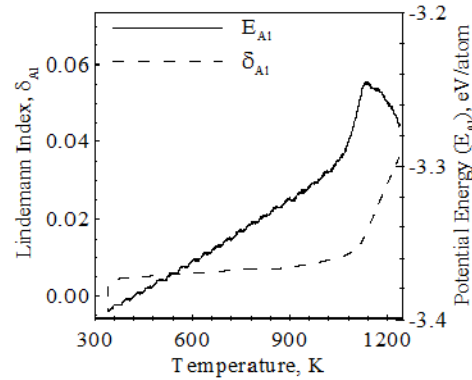
Figure 26 Lindemann index, δ_{Al}, and potential energy of the aluminum core as a function of temperature for a 14 nm particle with a 1 nm thick nickel shell

temperature at which the crystal undergoes catastrophic mechanical failure. The melting point elevation for a coated nano-particle has been observed in previous experimental [97,104-107] and theoretical [108,109] studies. The enhanced thermal stability of an encapsulated core is attributed to the epitaxial core-shell interface and/or to the pressure build up. The former is present in the particles considered in the present study, as seen in Fig. 25. In an uncoated particle, the surface atoms, which have higher energy than the atoms in the interior region, can vibrate easily. For a coated particle, the shell restricts the vibration of the interfacial core atoms, which have lower energy than those in the interior region. As a result, a significant increase in the melting point is observed.

Figure 27 shows the snapshots of the particle at 300 and 1100 K. Melting causes a

1100 K

Molten core
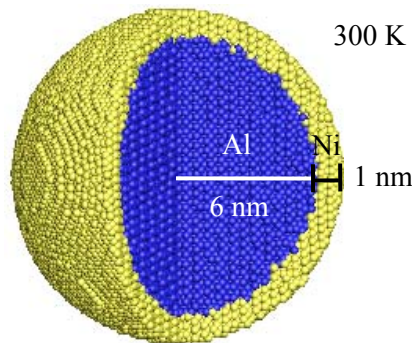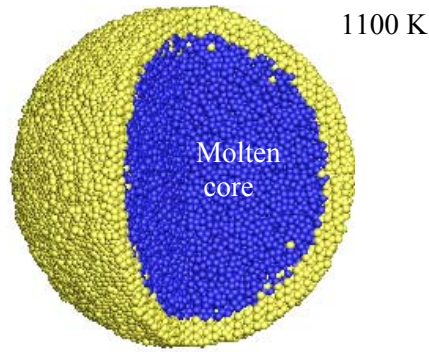
Figure 27 Snapshot of the particle before (300 K) and after (1100 K) core melting

significant change in the crystal structure of the core. At 300 K, a well-defined structural order is present, but no such order is observed at 1100 K. The crystal structure of the shell is negligibly affected. Figure 28 shows the variation of the core radius with temperature. The sudden increase
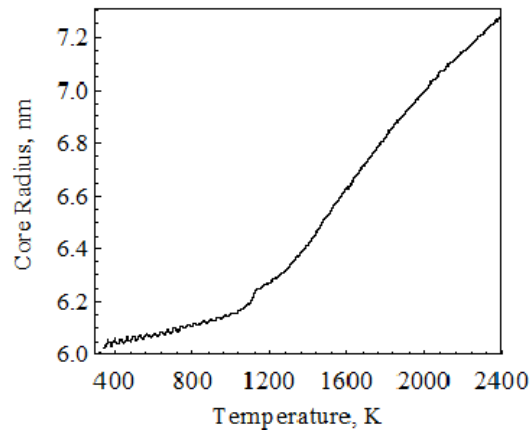
Figure 28 Core radius as a function of temperature for 14 nm particle with a 1 nm thick Ni shell

in the core radius at ~1000 K may be attributed to the volume dilation of the core associated with melting. Note that the aluminum core dissolves nickel atoms at the interface. The aluminum atoms continue to diffuse into the shell, which causes the core radius to increase monotonically. Figure 29 shows the diffusion processes occurring in the particle over the temperature range of interest (300-2400 K). Aluminum atoms diffuse into the shell and nickel atoms diffuse into the core, resulting in the formation of a homogeneous alloyed particle. The diffusion processes prevail upon melting due to the higher mobility of the melted atoms. Note that complete
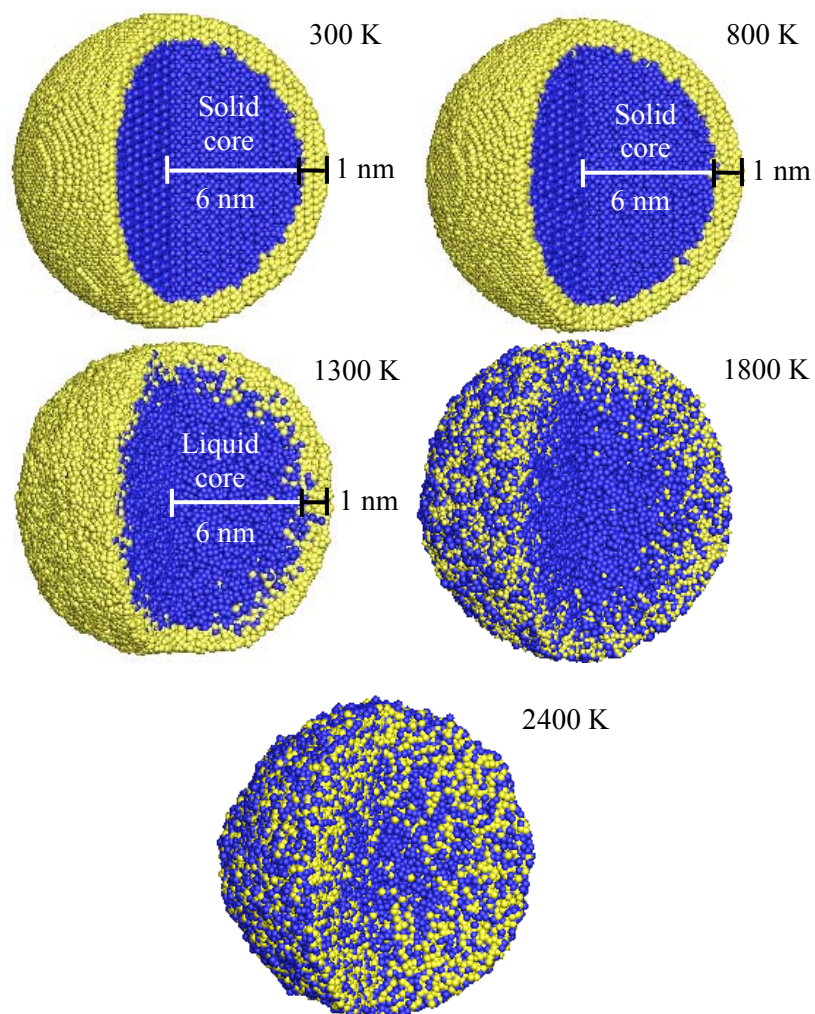
Figure 29 Snapshots of 14 nm particle showing melting and diffusion processes

homogenization is not observed at 2400 K, suggesting that higher temperatures are required for complete mixing of the core and shell atoms. Figure 30 shows the variation of the average potential energy of the particle with temperature. The potential energy rises, attains a plateau, and then decreases. This trend is a characteristic of the core-shell particle structure, and is not observed for nascent particles. The result suggests the formation of low-energy species from the following exothermic inter-metallic reaction:
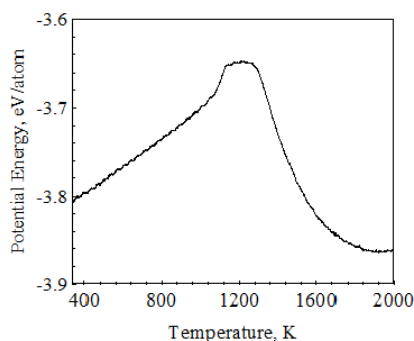
Figure 30 Average potential energy of the particle as a function of temperature for core diameter of 12 nm and shell thickness of 1 nm

$$Ni + Al \rightarrow NiAl. \tag{22}$$

The heat of formation of NiAl is 62 kJ/mol at room temperature [110]. The initial rise in the potential energy is caused by the transfer of energy from the heat reservoir to the particle. The plateau represents the stage at which this energy supply is counterbalanced by the formation of the low-energy species, NiAl. The subsequent decrease indicates the preponderance of the inter-metallic reactions.

Note that the interfacial aluminum atoms mix with nickel atoms even at room temperature. If the particle is heated externally to a temperature at which the reactions begin to occur rapidly, it can ignite, provided that the rate of chemical heat generation is greater than that of heat loss to the ambient environment. An energy balance is performed to estimate the equilibrium temperature of the particle upon completion of the inter-metallic reactions at adiabatic conditions. The result is compared with the value obtained from the MD simulation. The thermodynamic energy balance takes the form

$$H_{reac}\left(T_i\right) = H_{prod}\left(T_{ad}\right), \tag{23}$$

where H_{reac} is the enthalpy of the reactants calculated at an initial temperature, T_i, and H_{prod} the enthalpy of the products evaluated at the adiabatic reaction temperature, T_{ad}. The initial temperature is taken as 1250 K, which corresponds to the point at which the potential energy begins to decrease. The enthalpy of the reactants, H_{reac}, is given by

$$H_{reac} = H_{Al}^{1250K} + H_{Ni}^{1250K} + H_{m,Al}. \tag{24}$$

The enthalpies of Al and Ni are calculated as 22.85 and 24.82 kJ/mol, respectively, and that of the melting of aluminum is taken as 10.71 kJ/mol. The enthalpy of the products is expressed as

$$H_{prod} = \left(1 - \frac{t_i A}{V}\right) H_{f,NiAl}^{298K} + C_{p,NiAl}\left(T_{ad} - 298\right) + H_{m,NiAl} \tag{25}$$

where A is the interfacial area, V the core volume and t_i the thickness of the interfacial zone. The interfacial core atoms participate in alloying reactions prior to melting of the core, thereby resulting in a decrease in the energy content of the particle. The fraction of the core volume that has already reacted depends on the interfacial area-to-core volume ratio and the thickness of the interfacial zone. The latter is approximated to be 0.7Å [80]. The specific heat and enthalpy of melting of NiAl are taken as 55 J/mol-K and 63 kJ/mol, respectively [111]. The equilibrium temperature calculated using Eqs. (13) and (14) is 2388 K. In other words, the particle is self-heated from 1250 to 2388 K due to the heat release from inter-metallic reactions.

Figure 31 shows the variation of the temperature of the particle with time under adiabatic conditions calculated using MD simulations. The initial position and velocities of atoms are those obtained from the heating simulation in an NPT ensemble at 1250 K. The particle is heated from 1250 to ~2300 K due to exothermic intermetallic reactions of aluminum and nickel atoms over a period of 100 ps. One of the reasons for the discrepancy is that equilibrium is not attained within a time period of ~100 ps. After a time period of 50 ps, the temperature increases very slowly. The particle snapshots obtained in NPT simulations also support this argument. It is also important to note that the atomic species are no longer expected to interact with a ground electronic configuration, but with an excited one at higher temperatures. Therefore, classical many-body potentials reproduce interaction forces only with modest accuracy, and *ab initio* methods should be applied. Note that the particle temperature increases by ~1000 K over a time period of ~100 ps. The resulting intrinsic heating rate is ~ 10^{13} K/s, which is equivalent to particle ignition.

42
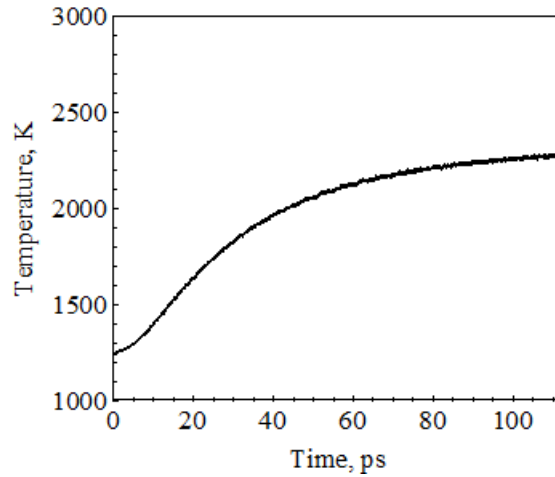
Figure 31 Temporal evolution of the particle temperature for core diameter of 12 nm and 1 nm thick shell

Effect of Core Size

The effect of core size is studied in the diameter range of 3-12 nm with a fixed shell thickness of 1 nm. Figure 32 shows the variation of the melting point of the core with the core diameter. It increases from 775 to 1000 K when the core diameter increases from 3 to 12 nm. Such a trend has also been observed in a previous study [78]. In all the cases, the presence of the nickel shell increases the melting point of the core. Figure 33 shows the snapshots of 8 nm particle colored by thermal displacement at different temperatures. As can be seen, the nucleation of the liquid phase begins at the core-shell interface and the melting front propagates to the
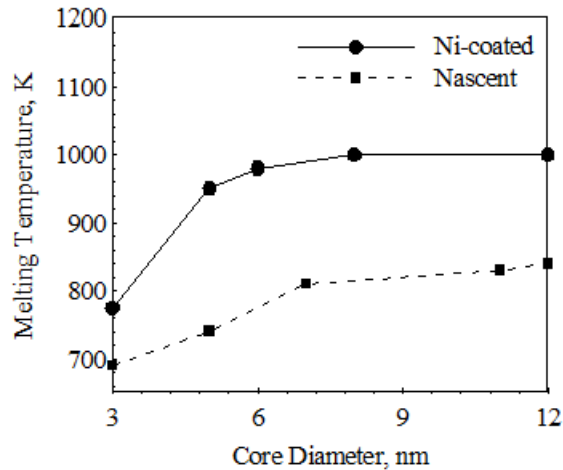
Figure 32 Effect of core diameter on the melting point of the core for a shell thickness of 1 nm

interior region of the core. The fact that heterogeneous nucleation at the interface dominates melting of superheated nano-particles has been observed previously in MD simulations [108]. Figure 34 shows the variation of the core radius with temperature for different core sizes. For a 3 nm core, the diffusion rate of aluminum atoms increases suddenly at 1400 K, a phenomenon that is not related to the melting of the core. The nickel shell melts at 1350 K,

950 K · 1000 K · 1030 K · 1050 K · 1090 K

δ_t, nm · 0.8 · 0.6 · 0.4 · 0.2
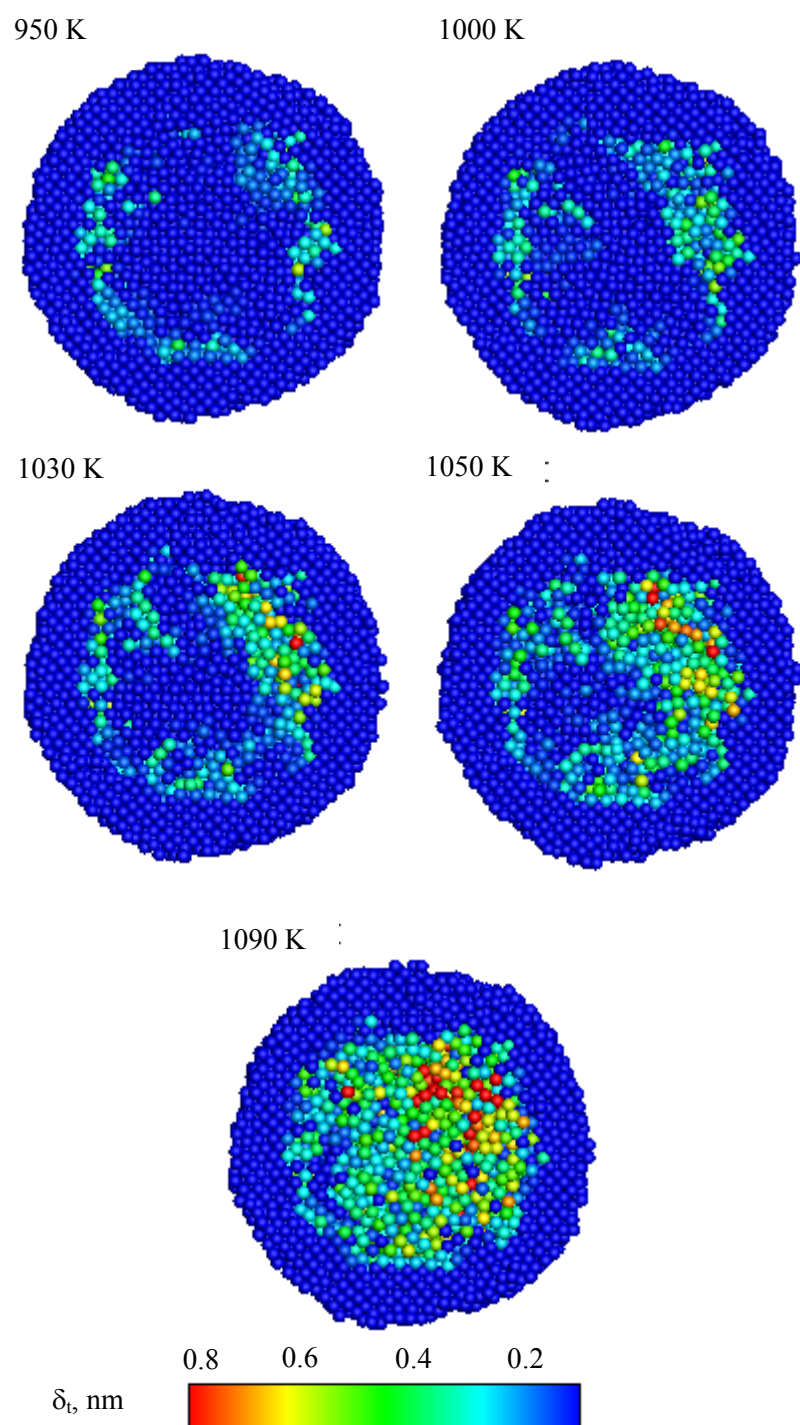
Figure 33 Particle snapshots showing thermal displacement of core atoms at different temperatures for 8 nm particle with 1 nm shell
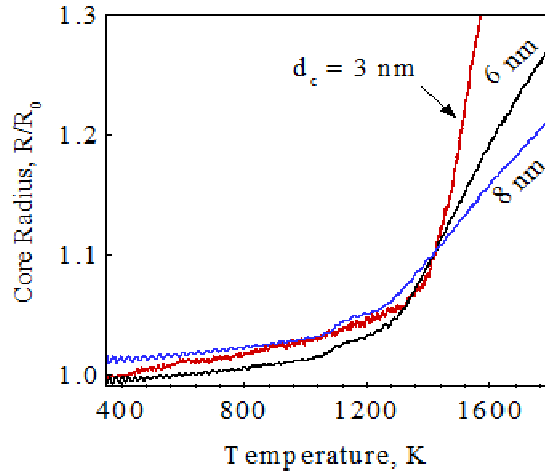
Figure 34 Normalized core radius as a function temperature for shell thickness of 1 nm

which is lower than the bulk melting point of nickel, 1728 K. Unlike a particle, a shell can begin to melt both at the surface and at the core- shell interface. The nickel shell with a molten aluminum cluster is less stable than a pure nickel particle of the same size [97]. For larger core diameters, the aluminum atoms begin to diffuse outwards at lower temperatures. Figure 35 shows the variation of the average potential energy of the particle with temperature. The magnitude by which the potential energy decreases is proportional to the core size. In other words, the smaller the core, the lower the chemical heat release due to the inter-metallic reactions. The temperature at which the potential energy begins to decrease may be identified as the ignition temperature. The calculated values are in the range of 1280-1480 K, which are near the melting point of the shell.
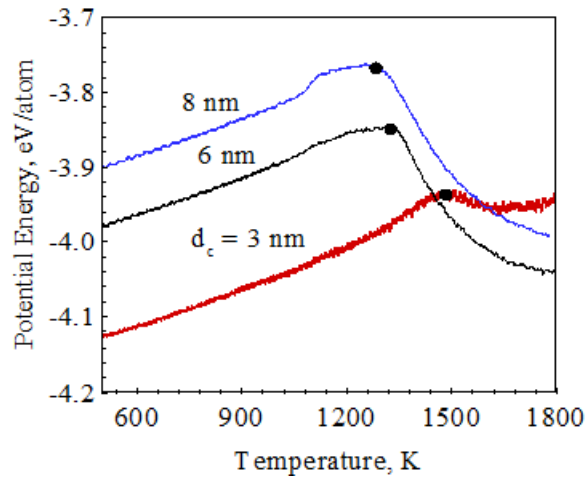
Figure 35 Effect of core diameter on the potential energy for a shell thickness of 1 nm

Simulations in NVE ensembles are performed to calculate the equilibrium temperature of the particle upon completion of the inter-metallic reactions for different core sizes. Figure 36 shows the effect of core diameter on the adiabatic reaction temperature of the particle. At a fixed shell thickness, the reaction temperature decreases with decreasing core size. For smaller cores, the temperature rise due to the inter-metallic reactions is relatively low. To understand the
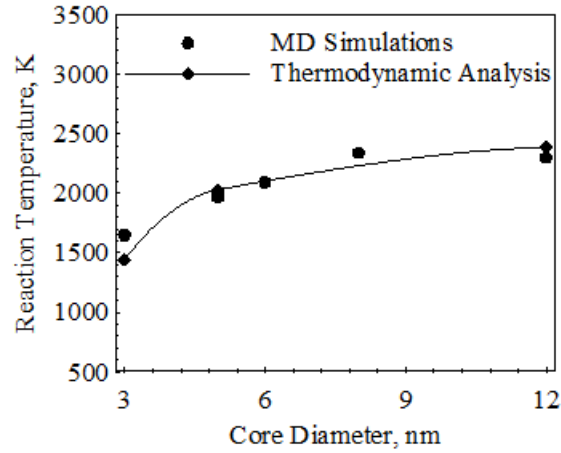
Figure 36 Effect of core diameter on adiabatic reaction temperature for 1 nm thick shell

relevant physiochemical phenomena, a companion thermodynamic analysis is also performed and the result is included in the figure. Figure 37 shows the equilibrium phase diagram for the Ni-Al system. The particle composition determines the inter-metallic compounds that are formed. For 3 nm core, the aluminum atomic fraction is 0.12 (nickel-rich). The resulting product is a mixture of Ni_3Al and Ni. For this case, the chemical reaction can be expressed as

$$7.2\,Ni + Al \rightarrow Ni_3Al + 4.2\,Ni. \tag{26}$$
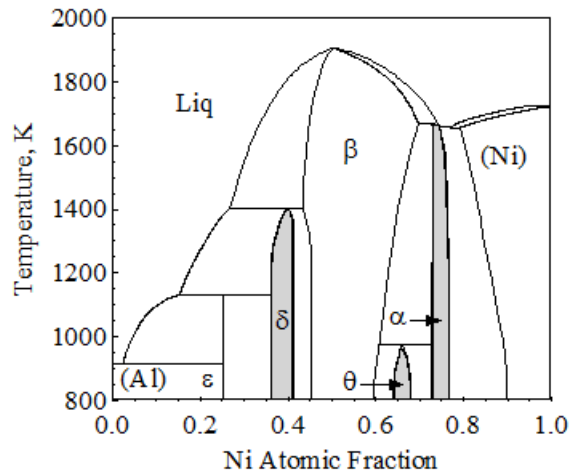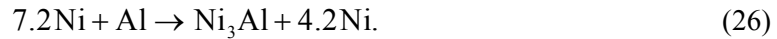
Figure 37 Ni-Al phase diagram (ε : NiAl$_3$, δ: Ni$_2$Al$_3$, β: NiAl, θ: Ni$_5$Al$_3$, and α: Ni$_3$Al) [112].

In the present analysis, the specific heat, enthalpy of fusion and heat of formation of Ni_3Al are taken to be 130 J/mol-K, 50 kJ/mol, and -164 kJ/mol, respectively [52]. The results support the fact that the adiabatic reaction temperature decreases with decreasing core size. This can be attributed to the following reasons. First, residual Ni atoms remain in the products, which do not participate in the reactions. Second, although the interfacial zone thickness is held constant, the fraction of interfacial core atoms increases with decreasing particle size. As a result, a greater percentage of core atoms have already reacted for a smaller core. Such an effect was also observed for aluminum-coated nickel particles [80]. For aluminum-rich particle, inter-metallic compounds such as NiAl$_3$ are formed. The situation is

46

typically encountered for aluminum-coated nickel particles. The ensuing thermal behavior is expected to be different.

Effect of Shell Thickness

      The effect of shell thickness is examined in the range of 0.5-3.0 nm. Figure 18 shows the melting point of the aluminum core as a function of shell thickness. The core melting point is not significantly affected by variations in the shell thickness in the size range of concern.
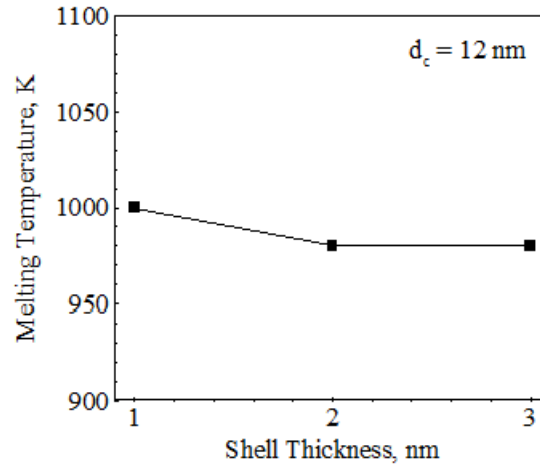
Figure 38 Effect of shell thickness on the melting temperature of the 12 nm core

Calculations indicate that the core is under compression (positive pressure on the order of 1000 MPa) and the shell under tension. A similar trend was also obtained for homogeneously heated oxide-coated aluminum particles [114]. Levitas [115] proposed a melt dispersion mechanism, which is valid at very high heating rates ($> 10^6$ K/s). According to this theory, the shell is ruptured by the tensile stress exerted by the core and the molten aluminum clusters are dispersed in the surrounding environment. In the present study, melt dispersion is not observed, thereby suggesting that the stresses are relaxed. One possible mechanism for such a phenomenon is the diffusion of aluminum atoms. Previous studies [116,117] indicate that the independence of melting temperature with shell thickness result from stress relaxation. It is, thus, not surprising that the
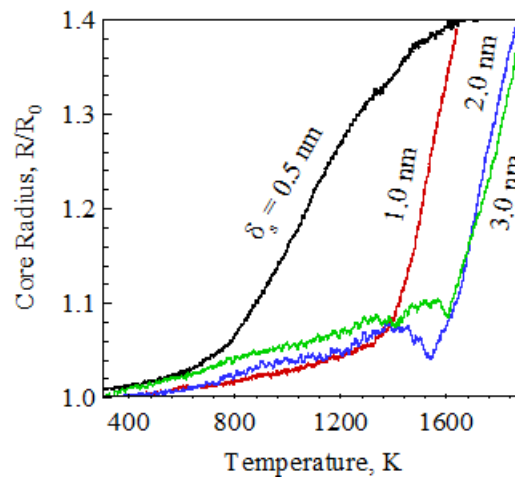
Figure 39 Variation of the core radius with temperature for a core diameter of 3 nm and shell thickness in the range of 0.5-3 nm

47

melt dispersion mechanism is not observed for nickel-coated aluminum particles. Figure 39 shows the core radius as a function of temperature for a core diameter of 3 nm and shell thickness of 0.5, 1, 2, and 3nm. Diffusion is facilitated for thinner shells. For a 0.5 nm shell, the core radius increases significantly upon melting of the core at 800 K. The core atoms, however, begin to diffuse out only at 1400, 1500, and 1600 K for shell thickness of 1, 2 and 3 nm, respectively. For a core diameter of 3 nm, the results suggest that the ignition temperature increases from 800 to 1600 K, when the shell thickness increases from 0.5 to 3.0 nm. Figure 40
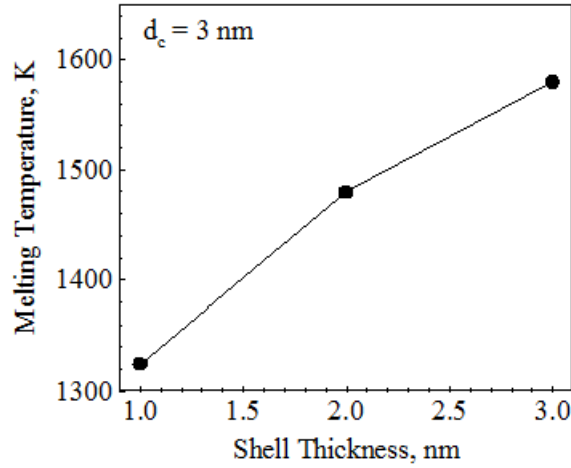
Figure 40 Effect of shell thickness on the melting temperature of the nickel shell for core diameters of 3 nm.

shows the effect of shell thickness on the melting point of the shell for core diameter of 3 nm. The shell melting point increases from a value as low as 1320 to 1580 K, when the thickness increases from 1 to 3 nm. In all cases, the melting point of the shell is lower than that corresponding bulk value of 1728 K. It is obvious that shell melting plays an important role in dictating the diffusion and ignition in nickel-coated aluminum particles.

The case of a particle covered by a very thin shell is of interest, since a previous study indicates the possibility of ignition near room temperature [81]. Furthermore, it is possible to create a particle with a reasonably large core size and a thin shell that features an equal number
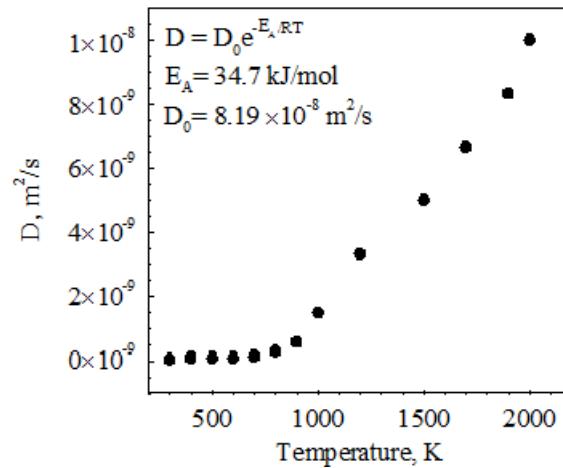
Figure 41 Diffusion coefficient of aluminum in nickel for a 7 nm particle with a 0.5 nm shell

of Al and Ni atoms. As a consequence, the energetic of inter-metallic reactions are easily tractable. In the present study, a 7 nm particle with a 0.5 nm shell is considered. The information about the diffusion coefficient of aluminum atoms in a nickel shell is useful, especially from the standpoint of development of macro-scale ignition and combustion models. Figure 41 shows the effect of temperature on the diffusion coefficient of aluminum atoms in a nickel shell. The diffusionprocess is very slow at temperatures lower than the melting point of the core. A sudden increase in the diffusion coefficient takes place after melting of the core. It exhibits a temperature dependence of the form

$$D = D_0 \exp\left(-\frac{E_A}{RT}\right), \tag{27}$$

 where E_A is the activation energy and D_0 is the pre-exponential factor. The curve-fit indicates a value of 34.7 kJ/mol for the activation energy and 8.19×10^{-8} m^2/s for the pre-exponential factor. The obtained diffusion coefficients can be used to study combustion of nickel-coated aluminum particles. Figure 42 shows the temporal evolution of the particle in adiabatic condition. The temperature increases suddenly upon melting of the core. The inter-metallic reactions result in particle heating from 300 to 1420 K. The results substantiate the fact that an aluminum particle coated by a thin nickel shell can be pyrophoric even in an inert environment.
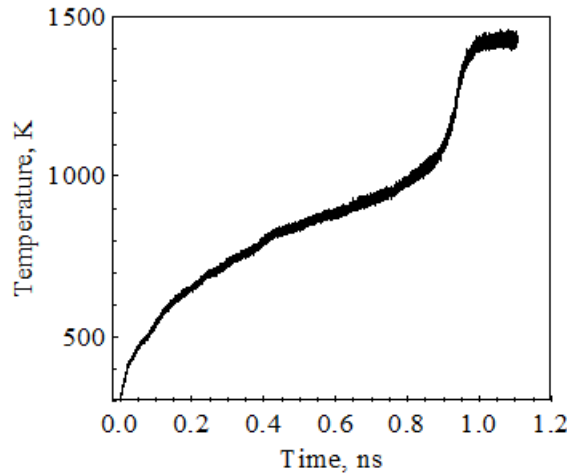
Figure 42 Temperature as a function of time for a 7 nm particle with a 0.5 nm thick shell under adiabatic condition

The thermo-chemical behavior of nickel-coated aluminum particles in the size range of 4-18 nm was studied using molecular dynamics simulations. The analysis was carried out in isothermal-isobaric and isochoric-isoenergetic ensembles using an embedded atom method. Emphasis was placed on analyzing the melting points of the core and shell, diffusion of atoms, and inter-metallic reactions. The aluminum core melted at a temperature greater than the melting point of a nascent aluminum particle due to the cage-like mechanical constraint imposed by the nickel shell. The melting point of the aluminum core increased from 775 K at 3 nm to 1000 K at 12 nm. It was not significantly affected by the variations in the shell thickness in the range of 1-3 nm. The melting point of the shell increased with increasing thickness, from a value as low as 1100 K at 1 nm to 1580 K at 3 nm. Melting was followed by diffusion of atoms and energy release due to inter-metallic reactions, which resulted in self-heating of the particle. The diffusion coefficient of aluminum atoms in the nickel shell had an exponential dependence on temperature, with an activation energy of 34.7 kJ/mol. The adiabatic reaction temperature of the particle increased from 1650 to 2338 K, when the core diameter increased from 3 to 8 nm. The calculated values

exhibited reasonably good agreement with predictions from a thermodynamic energy balance analysis. The results demonstrated that nickel-coated aluminum particles can ignite even in inert environments (or in the absence of an oxidizing gas). Future work will focus on the energetics of aluminum-coated nickel particles and the comparison with the results of nickel-coated aluminum particles obtained from the present study. Furthemore, a multi-scale model will be developed to study the flame propagation of nickel-coated aluminum particles. Results from MD simulations will be used to characterize the burning behavior of individual particles.

B. Combustion of Nano-Aluminum Particles and Liquid Water Mixtures (Georgia Tech with Penn State)

The combustion of aluminum particles in water is of relevance to many propulsion and energy-conversion applications. In metalized composite solid propellants, aluminum particles typically react with the combustion products of the polymeric binder and ammonium perchlorate, of which water vapor (H_2O) and carbon dioxide (CO_2) are two major species [118]. The problem is of particular interest for underwater propulsion, since the oxidizer (water) could be supplied from the environment [119]. The combustion of aluminum particles in water has also been studied in the contexts of hydrogen generation [120], nuclear reactor and industrial manufacturing safety [121], and underwater explosives [122]. The frozen mixture of aluminum particles and water (ALICE) is also under consideration for several energetic applications, due to its structural integrity ([123], [124]).
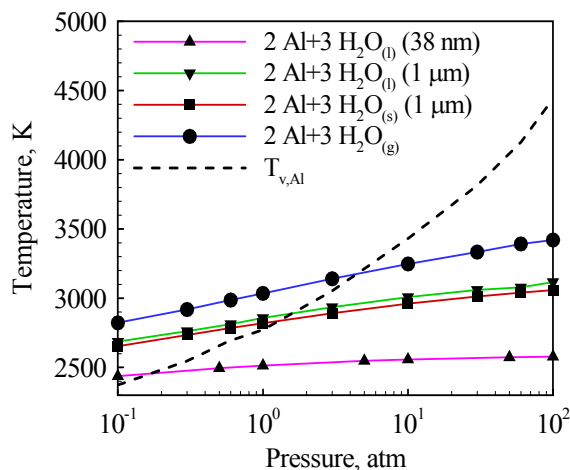
Figure 43 Effect of pressure on aluminum vaporization temperature and adiabatic flame temperatures for various oxidizers

The ignition and combustion characteristics of aluminum particles in water are different from those in oxygenated environments. Figure 43 shows the effect of pressure on the aluminum vaporization temperature ($T_{v,Al}$) and adiabatic flame temperature (T_f) of aluminum-water mixtures with different particle sizes and water in various thermodynamic states. The particles are assumed to be passivated, with an oxide shell thickness of 3 nm. The flame temperature is lower than the vaporization temperature for pressures over a "cut-off" value. For micron-sized particles, this occurs in the range of ~1-4 atm, depending on the thermodynamic state of water. For nano-sized particles, the cut-off pressure is as low as ~0.2 atm. This can be attributed to the fact that the inert oxide layer constitutes a greater portion of the particle mass at nano-scales; a 50 nm aluminum particle, for example, contains 32 wt. % oxide [122]. It should be pointed out that the actual flame temperature can be lower than the theoretical value, due to the effects of heat losses and incomplete combustion. As a result, in most practical cases, nano-aluminum does not vaporize and heterogeneous chemical reactions occur at the particle surface.

50

Figure 44 shows the effect of particle size on the ignition temperature of aluminum particles in water-vapor containing environments. Oxidation was studied by various methods including a thermogravimetric analyzer [125], electrical heating [126], shock tube [127], hydrogen-oxygen-argon burner [128], and arc burner [129]. Both spherical particles ([125], [127-129]) and wire samples [126] were considered. In the thermo-gravimetric experiments [125], the particles were heated at relatively low rates in the range of 1-20 K/min. The oxidizing gas consisted of 27 % H_2O and 73 % Ar. The reactions were observed at much lower temperatures in water vapor than in oxygen. Specifically, a stepwise weight change was observed at the melting point of aluminum (660 °C) and the particle is completely oxidized at ~1000 °C. Note that the experimental conditions are different in the referenced studies. For example, the heating rates in shock tube experiments [127] are much higher (~10^6 K/s) and the oxidizer concentration is different from those employed in other studies. It is also worthwhile to mention that the measured ignition temperature in burner ([128], [129]) and shock tube [127] experiments corresponds to the temperature of the gas. The ignition temperature depends on various parameters such as the particle characteristics, oxidizer concentration, and heating rate. For these reasons, the experimental data cannot be quantitatively compared directly. Nevertheless, it is true that the ignition temperature increases with increasing
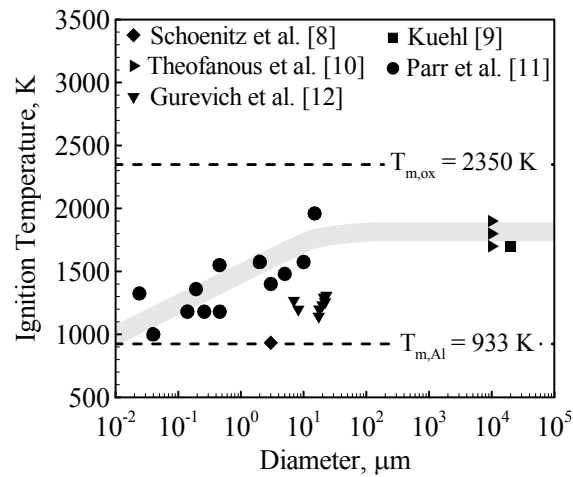
Figure 44 Effect of particle size on ignition temperature of aluminum particles in water vapor

particle size in the range of 10 nm-100 μm. Even for larger particles, it remains lower than the melting point of the oxide layer, 2350 K. This suggests that the ignition temperatures of aluminum particles in water vapor are lower than those in oxygen. The phenomenon may be attributed to the stabilization of γ-oxide polymorph [125] and/or formation of a weaker hydroxide layer on the particle surface [126].

Many of the desirable traits of nano-sized particles are due to the presence of a large percentage of atoms on the surface [130]. The percentage of atoms on the surface layer of an aluminum particle increases from 2 to 92 %, when the particle size decreases from 100 to 1 nm. The surface atoms have lower coordination numbers and higher energies than the atoms in the interior region of the particle. As a result, the thermophysical properties of nano-sized particles are significantly different from their corresponding bulk values. The melting temperature of nano-aluminum particles decreases from 933 to 473 K when the particle size decreases from 10 to 2 nm ([131], [1132]). Similarly, the melting point of the oxide layer can be lower than the bulk value of 2350 K; for a shell thickness of 2.5 nm the melting point of the oxide layer is 1313 K [133]. The ignition temperatures and burning times of nano-aluminum particles are also lower than their micron-sized counterparts [134]. Significant enhancement in the burning characteristics is, thus, expected, when nano-sized particles are used to formulate energetic materials [135].

The combustion of nano-sized aluminum particles and water has been studied experimentally for a relatively wide range of pressure and particle size ([122], [136], [137]). Results from earlier studies ([136],[137]) suggested that the presence of a gelling agent such as polyacrylamide is necessary to achieve self-sustained deflagration. Risha et al. ([122],[138]), however, demonstrated self-deflagration of aluminum-water mixtures in a constant volume optical pressure vessel. The particle diameters covered a range of 38-130 nm and the pressure range of interest was 0.1-10 MPa. The measured burning rates were found to be inversely proportional to particle size and exhibited a pressure dependence of the form $r_b = ap^m$, with the exponent in the range of 0.27-0.47. Both transport and chemistry were speculated to affect the burning behavior, but key mechanisms and parameters are yet to be explored [122]. In the present study, a theoretical model is developed to study the flame propagation of a quasi-homogeneous mixture of nano-sized aluminum particles and liquid water. Special attention is placed on the effects of particle size and pressure on the flame structure and burning property. Results suggest that the combustion of nano-aluminum/water mixtures is controlled by mass diffusion through the oxide layer of the particles. Reasonably good agreement with experimental data is achieved, demonstrating the validity of the proposed model.

Experiment

The burning rates of nano-aluminum/water mixtures were obtained in an argon environment using a constant volume vessel, as shown schematically in Fig. 45. The chamber, made of stainless steel, is equipped with four optical viewing ports, each having a 15.2 × 2.54 cm field of
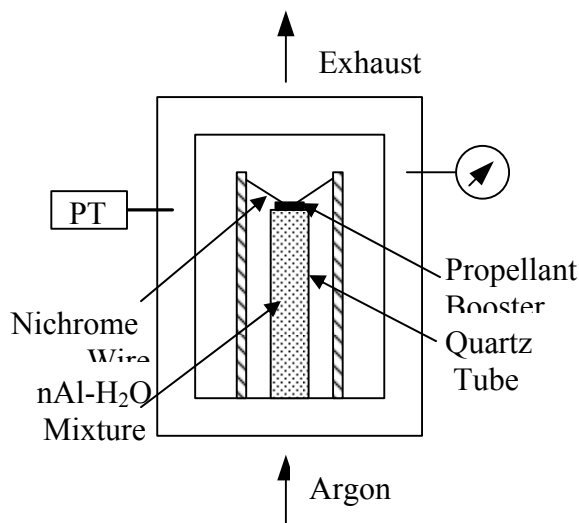
Figure 45 Schematic of constant-pressure strand burner with optical access

view. The 61-cm long chamber has an inner diameter of 22 cm and a total free volume of 23 liters; the relatively large volume minimizes the pressure variation caused by the generation of gaseous combustion products. The base plate has six feed-through ports to provide pathways for electrical signals and gas lines into the chamber. Nano-aluminum particles were obtained from Technanogy and Nanotechnology. They were mixed with stoichiometric amount of distilled water in a sealed plastic bag. Stoichiometry was calculated based on the active aluminum content in the particle. No gelling agent was employed. The mixture was then packed into a quartz glass tube (1 cm OD, 0.8 cm ID, 7.5 cm long). Ignition was achieved using a small ~1/8 in. thick propellant booster made of a homogenous double-base propellant (NOSOL 363) initiated by a resistance-heated nichrome wire threaded through the booster. The temporal evolution of the regressing luminous front was tracked and recorded using video equipment. Figure 46 shows captured images of stoichiometric mixture containing 80 nm particles burning at a pressure of 5.8 MPa. The flame front propagates through the packed mixture at a constant velocity. The measured

position-time curve was used to determine the burning rate of the strand. More details of the experimental set-up can be found in [122].
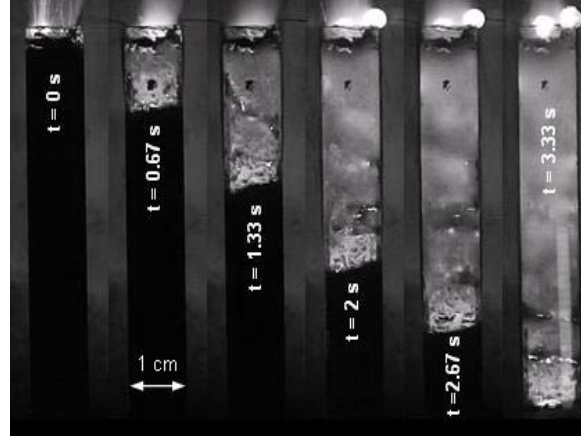
Figure 46 Captured images of stoichiometric aluminum-water mixture containing 80 nm particles burning at a pressure of 5.8 MPa

Theoretical Framework

The analysis considers one-dimensional, isobaric, and planar flame propagation in a chemically reacting system consisting of passivated nano-aluminum particles and liquid water. Note that the present study deals with the downward propagating flame. For other conditions, the released hydrogen gas is likely to affect the heat transfer to the unburned mixture. The aluminum-water mixture is a viscous paste with dense particle loading and significant particle-particle interactions, as opposed to dust clouds that feature dilute particle concentrations ([134], [139]). Furthermore, the gaseous oxidizer (water vapor) is produced *in situ* by vaporization, instead of being supplied externally. The particles are assumed to be uniformly sized and their agglomeration is neglected. Flame propagation, which takes place through thermal conduction, is accompanied by a variety of physicochemical processes, including water vaporization, chemical reactions, and mass, momentum and energy exchanges between the fluid and particle phases. The system is approximated to be pseudo-homogenous, so that the particles and surrounding fluid are in thermal equilibrium locally. Water vaporization occurs on an infinitesimally thin plane. Figure 47 shows the multi-zone flame structure considered in the present study. The entire spatial domain is divided into three zones to demarcate the regions in which phase transition and chemical reactions occur. The initial temperature of the mixture is 298 K. Water undergoes a thermodynamic phase transition at the vaporization front, $x = -\delta_v$, where the local temperature reaches the vaporization point, T_v. The particles start to burn once the ignition temperature, T_{ign}, is attained. Chemical reactions are neglected in the preheat zones.

The thermal conductivity of the mixture, λ_m, depends on the loading density and thermal conductivity of the particles. The following correlation provides the best fit to experimental data for a wide range of particle volume fractions [140]:

$$\lambda_m = \lambda_p \exp\left(\frac{-1.5\Phi_f}{1-\Phi_f}\right) \tag{28}$$

where λ stands for the thermal conductivity and Φ the volume fraction. The subscripts m, p, and

$$Al\text{-}H_2O_{(l)} \quad Al\text{-}H_2O_{(g)} \quad \begin{array}{c} Al\text{-}Al_2O_3\text{-} \\ H_2O_{(g)}\text{-}H_2 \end{array}$$

53
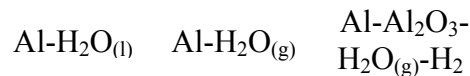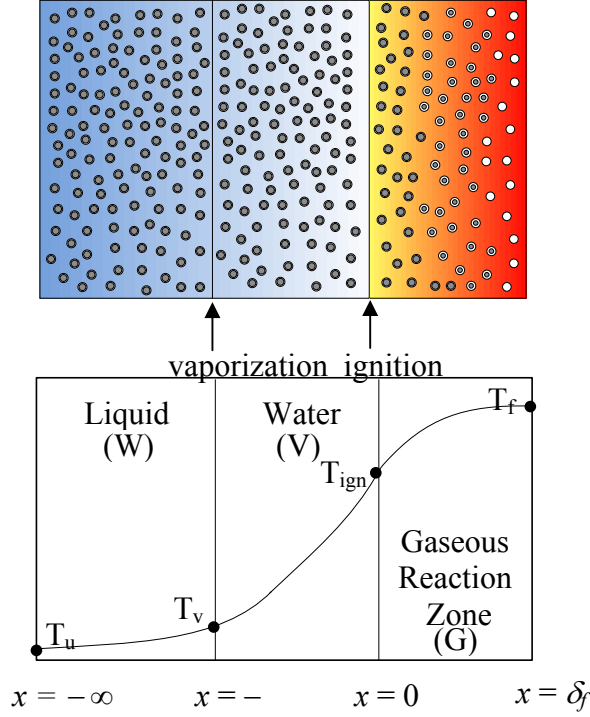
Figure 47 Physical model and multi-zone flame structure (● Al, ○ Al₂O₃)

f refer to mixture, particle, and fluid, respectively. Equation (28) assumes that the fluid is non-conducting when compared with the particle. This is a reasonable approximation, since the former value is two or three orders of magnitude lower than the latter. Furthermore, it is reassuring to note that the thermal conductivity predicted by the correlation agrees with the experimental data for a wide range of particle volume fractions. The oxide layer hampers the flame propagation, due to its inefficiency as a conductor of heat. The overall thermal conductivity of the passivated aluminum particle, λ_p, is calculated as follows [141]:

$$\lambda_p = \frac{\lambda_{Al}^2 R}{(r-R)\left[2\lambda_{Al}\ln a - 2\lambda_{ox}\ln a - \left(\lambda_{Al}^2 / \lambda_{ox}\right)\right] + r\lambda_{Al}}, \tag{29}$$

where

$$a \equiv \frac{b - \lambda_{Al}R}{b - \lambda_{Al}(R-r)}; \quad b \equiv 2(R-r)\lambda_{ox} + 2r\lambda_{Al}. \tag{30}$$

Here r is the radius of the aluminum core and R the outer radius of the particle. The subscripts *Al* and *ox* refer to aluminum and oxide, respectively. The thermophysical properties of water and hydrogen are given in Ref. [142], while those of aluminum and its oxide are taken from Refs. [143-145] and Ref. [146], respectively. Table 5 summarizes the property data at a baseline pressure of 3.65 MPa. All properties are evaluated at an average temperature in each zone. The enthalpy of vaporization and boiling point of water are calculated as a function of pressure. A continuum-

Table 5 Thermophysical properties of different species in three zones at baseline pressure of 3.65 MPa*

Species	Thermal conductivity, W/m-K			Specific heat, kJ/kg-K			Density, kg/m³		
	W	V	G	W	V	G	W	V	G
Aluminum	239	95	143	0.954	1.260	1.176		2700	
Aluminum Oxide	22.20	9.50	6.40	0.930	1.200	1.303		4000	
Liquid water	0.70	–	–	4.400	–	–	995	–	–
Water Vapor	–	0.07	0.12	–	2.330	2.580	–	8.58	5.17
Hydrogen	–	–	0.80	–	–	16.150	–	–	0.56

* $T_v = 519$ K, $T_{ign} = 1360$ K, $T_f = 1800$ K at $p = 3.65$ MPa
W: liquid water zone; V: water vapor zone; G: gaseous reaction zone

regime heat transfer model is considered, since the present study deals with pressures representative of those in practical propulsion systems. Free molecular effects are neglected without significant reduction in accuracy [123]. Mass and energy balances are enforced for a differential element in each zone. The resulting conservation equations are solved to obtain the burning rate and temperature distribution. The formulation is developed based on a coordinate system attached to the propagating flame.

Energy balance for the liquid water zone

The liquid water zone encompasses the region between the far field, $x = -\infty$, and the vaporization front, $x = -\delta_v$. The energy equation takes the form

$$\left(\rho_{Al} C_{p,Al} \Phi_{Al} + \rho_{ox} C_{p,ox} \Phi_{ox} + \rho_{lw} C_{p,lw} \Phi_{lw} \right) r_b \frac{dT}{dx} = \lambda_{m,W} \frac{d^2T}{dx^2}, \tag{31}$$

subject to the boundary conditions:

$$T_{x \to -\infty} = T_u ; T_{x=-\delta_v} = T_v ; \tag{32}$$

where ρ is the density, C_p the specific heat, r_b the burning rate, T the temperature, x the space coordinate, and δ_v the thickness of the vapor zone. The subscripts W, u, v, ox, and lw refer to the liquid water zone, unburned state, vaporization, oxide, and liquid water, respectively. An analytical solution to Eq. (31) is obtained for the temperature profile.

$$T = T_u + \left(T_v - T_u \right) \exp \left\{ k_W \left(x + \delta_v \right) \right\}, \tag{33}$$

where k_W is the ratio of the burning rate to the thermal diffusivity, defined as

$$k_W = r_b / \left(\lambda_{m,W} / \left(\rho C_p \right)_W \right), \tag{34}$$

55

where (ρC_p) denotes the volume-averaged product of the density and specific heat of the mixture. The temperature profile depends on the burning rate and thickness of the water vapor zone, both of which are not known *a priori*.

Energy and mass balance for the water vapor zone

Water vapor generated at the vaporization front, $x = -\delta_v$, flows through the interstitial space between particles. The conservation of mass of water is enforced to determine the velocity of water vapor at the vaporization front

$$\rho_{lw} r_b = \rho_{wv} v_{wv}. \tag{35}$$

Here, v is the gas velocity. The subscript wv denotes water vapor. Equation (35) can be used to express the energy equation in the following form:

$$\left(\rho_{Al} C_{p,Al} \Phi_{Al} + \rho_{ox} C_{p,ox} \Phi_{ox} + \rho_{lw} C_{p,wv} \Phi_{lw} \right) r_b \frac{dT}{dx} = \lambda_{m,V} \frac{d^2 T}{dx^2}, \tag{36}$$

subject to the interfacial conditions:

$$\begin{cases} x = -\delta_v : \lambda_m \dfrac{dT}{dx}\Big|_V = \lambda_m \dfrac{dT}{dx}\Big|_W + h_{fg} \Phi_{lw} \rho_{lw} r_b, \\[2mm] x = 0 : T = T_{ign}, \end{cases} \tag{37}$$

where h_{fg} is the enthalpy of water vaporization and T_{ign} the ignition temperature of nano-aluminum particles. The subscript V refers to the water vapor zone. The thickness of this zone is obtained by performing the heat-flux balance at $x = -\delta_v$:

$$\delta_v = \frac{1}{k_V} \log \left\{ \left(1 + \frac{\lambda_{m,V} k_V \left(T_{ign} - T_v \right)}{\lambda_{m,W} k_W \left(T_v - T_u \right) + h_{fg} \rho_{lw} \Phi_{lw} r_b} \right) \right\}. \tag{38}$$

The temperatures at the interfacial boundaries are matched to provide a closed-form solution to the energy equation:

$$T = \frac{1}{1 - e^{-k_V \delta_v}} \left[T_v \left(1 - e^{k_V x} \right) - T_{ign} \left(e^{-k_V \delta_v} - e^{k_V x} \right) \right]. \tag{39}$$

Energy balance for the reaction zone

The stoichiometric reaction of aluminum particles with water vapor is given by

$$2 Al + 3 H_2 O \rightarrow Al_2 O_3 + 3 H_2. \tag{40}$$
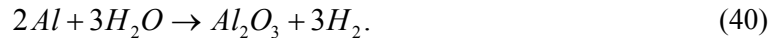
The properties are calculated by averaging their respective values of the reactant and product species. The energy equation can be expressed as [134]

$$\left(\sum_i \rho_i C_{p,i} \Phi_i \right) r_b \frac{dT}{dx} = \lambda_{m,G} \frac{d^2 T}{dx^2} + \frac{\rho_m Q_r}{\tau_b}, \tag{41}$$

where Q_r is the chemical energy release per unit mass of the mixture, and τ_b the particle burning time. The subscripts G, m and i refer to the reaction zone, mixture, and species i, respectively. To facilitate the analysis, the temperature and spatial coordinate are normalized as follows:

$$\theta = \frac{T}{T_u}, \quad y = \frac{x}{r_b \tau_0},$$

(42)

where τ_0 is the reference time scale defined as the particle burning time at a reference temperature. The location $y = 0$ is the ignition point of particles. Substituting the normalized variables defined in Eq. (42) into Eq. (41), the non-dimensional form of the energy equation is obtained

$$\frac{d^2\theta}{dy^2} - \kappa^2 \frac{d\theta}{dy} = -\mu\kappa^2 \left(\theta_{ign} - 1\right)\frac{\tau_0}{\tau_b}.$$

(43)

Here $\kappa = r_b \cdot \sqrt{\tau_0 / \alpha_{m,G}}$ is the normalized burning rate, with α being the thermal diffusivity. The normalized heat-release, μ, is written as

$$\mu = \frac{-\alpha_{m,G}\rho_m Q_r}{\lambda_{m,G}\left(T_{ign} - T_u\right)}.$$

(44)

The energy equation gives only a partial description of the underlying physicochemical phenomena in the reaction zone. In particular, an equation for the consumption of the particle mass is also needed.

Particle mass consumption in the reaction zone

The composition of the particle changes during the course of its reaction with water vapor. The aluminum content decreases progressively and a spherical oxide particle forms after complete oxidation. To characterize the combustion of individual particles, an equation for the particle mass consumption is considered

$$r_b \frac{dM_p}{dx} = -\frac{M_{p0}}{\tau_b},$$

(45)

where M_p is the particle mass. The subscript 0 refers to the initial state. Equation (45) can be re-written in terms of the particle size

$$\frac{d\left(d_p^3\right)}{dx} = -\frac{d_{p0}^3}{r_b . \tau_b},$$

(46)

where d_p is the particle diameter. For consistency, the particle diameter is normalized as follows:

$$\eta = \frac{d_p}{d_{p0}}.$$

(47)

Substituting the normalized variable defined in Eq. (47) into Eq. (46), the non-dimensional form of the particle mass consumption equation is obtained

$$\frac{d\eta^3}{dy} = -\frac{\tau_0}{\tau_b},$$

(48)

57

The following boundary conditions are specified to close the formulation:

$$
\begin{cases}
y = 0 : \lambda_m \dfrac{d\theta}{dy}\bigg|_G = \lambda_m \dfrac{d\theta}{dy}\bigg|_V , \quad \theta = \theta_{ign}, \quad \eta = 1 \\[4mm]
y = 1 : \dfrac{d\theta}{dy} = 0, \quad \eta = 0.
\end{cases}
\tag{49}
$$

The mass and energy balance equations in the reaction zone are solved numerically, with the burning rate treated as the eigenvalue. A shooting technique is employed to find the solution; the Newton-Raphson iteration method is used [147]. Numerical integration is achieved by means of the Rosenbrock method [147].

Heat release
The actual heat release from particle burning is lower than its theoretical counterpart due to incomplete combustion. The combustion efficiency of nano-aluminum/water mixtures is in the range of 80-100%, depending on the pressure and particle size [138]. Heat loss to the environment also occurs through thermal conduction and radiation. To incorporate these effects into the model, the normalized heat release is calculated based on the actual flame temperature. A simplified expression for the normalized heat release is obtained by integrating the energy equation, Eq. (16), and imposing the boundary conditions specified in Eq. (49)

$$
\mu = \frac{\kappa^2 \left(\theta_f - \theta_{ign} \right) + \dfrac{d\theta}{dy}\bigg|_G}{\left(\theta_{ign} - 1 \right)},
\tag{50}
$$

where the subscript f denotes the flame. Diakov et al. [148] studied the flame propagation of aluminum-water mixtures in a stainless steel chamber equipped with thermocouples at a pressure of 1 atm. The particle size is 100 nm and the oxide layer thickness is 1.84 nm. The measured flame temperature is 1800 K, which is significantly lower than the theoretical value of 2790 K for a particle size of 100 nm. The combustion efficiency is measured to be 87%. A similar scenario was observed for magnesium-water mixtures [149]. The combustion efficiency increases with decreasing particle size [138], although the adiabatic flame temperature is lower for smaller particles. For simplicity, a flame temperature of 1800 K is used to calculate the heat release for all particle sizes. Results of the sensitivity analysis indicate that the burning rate increases modestly with increasing flame temperature. At a pressure of 3.65 MPa and particle size of 38 nm, the burning rate increases from 5.59 to 6.85 cm/s when the flame temperature increases from 1800 to 2300 K.

Ignition temperature and burning time of particles
The present model requires, as input parameters, the ignition temperature and burning time of nano-aluminum particles. The ignition temperatures of Technanogy aluminum particles (24-192 nm) in water vapor vary between 1325 and 1360 K [128], as shown in Fig. 44. For convenience, we assume the ignition temperature to be 1360 K.

The combustion of aluminum particles involves mass diffusion through the gas-phase mixture and oxide layer, and chemical reactions between the aluminum atoms and oxidizer molecules. For micron-sized and larger particles, combustion is controlled by species diffusion through the gas-phase product mixture; the burning time follows $d_p^{1.8}$-law and exhibits weak dependencies on temperature and pressure [134]. For particles smaller than 1 μm, the pressure and temperature of the ambient gas

significantly influence the burning time [150], whereas the particle size exerts only a weak effect [134]. The latter trend may be attributed to the transition from the continuum to the free-molecular heat transfer regime [34] and/or sintering and agglomeration of particles. The present study deals with the conditions in the continuum regime, in which the burning rate is more size dependent. For nano-sized particles, surface tension leads to strong adherence of the oxide layer to the particle [152]. This phenomenon was also observed in molecular dynamics simulations [133].

The diffusion resistance provided by the oxide layer is several orders of magnitude greater than that of the gas-phase mixture. As a result, species diffusion through the oxide layer is the rate-controlling process [153]. Park et al. [154] studied the oxidation of nano-aluminum particles in air using single particle mass spectrometry for temperatures up to 1373 K. The measured oxidation rates exhibited reasonably good agreement with the results of the diffusion-controlled combustion model. The kinetically-controlled model, however, failed to capture the observed trends. These results support the hypothesis that the combustion of nano-sized aluminum particles is controlled by species diffusion processes rather than by chemical kinetics. To estimate the particle burning time, therefore, the diffusion coefficients of the reacting species in the oxide layer are required. They are, however, poorly known, and only with uncertainties of several orders of magnitude [155]. In the present study, the reaction time scale is approximated to be the particle burning time. This is physically justified because the energy release rate is dictated by the reactivity of the individual particles [134]. Theory suggests that the characteristic time scale for species diffusion through the oxide layer is inversely proportional to pressure and bears a d_p^2-relationship ([153], [154]). The observed particle size effect on the burning rate is obtained only if such a relationship is employed. A d_p^2-law is, thus, adopted for the burning time. The reference time scale is taken to be the burning time of a 24 nm aluminum particle and the pressure exponent in the burning time relationship varies between -0.3 and -1.0, depending on the ambient temperature ([128], [148]):

$$\tau_b = \frac{c\left[a_1 \exp\left(b_1 T\right) + a_2 \exp\left(b_2 T\right)\right] d_p^2}{p^m}, \tag{51}$$

$$m = a_3 \exp\left(b_3 T\right) + a_4 \exp\left(b_4 T\right), \tag{52}$$

where d_p is the particle diameter in nm and p the ambient pressure in atm. The constants are given in Table 6. The theoretical studies on oxidation of nano-aluminum particles also indicate that the diameter exponent in the burning time relationship is in the range 1.6-2.0 [155].

Table 6 Constants in burning time expression

Constant	Value
c	1.736×10^{-3}
a_1	204.650
b_1	-9.848×10^{-3}
a_2	1.842×10^{-4}
b_2	3.461×10^{-5}
a_3	7.075
b_3	-1.905×10^{-3}
a_4	4.023×10^{-1}
b_4	-3.120×10^{-4}

Analytical Model of the Mixture Burning Rate

      With judicious simplifications, it is possible to obtain an analytical expression for the burning rate [149]. The specific heat capacities of different species and thermal conductivities of the mixture in the three zones (see Fig. 47) are assumed to be equal. The energy equation can be written as

$$\left[\rho_p\left(1-\varPhi\right)+\rho_{lw}\varPhi\right]C_p r_b \frac{dT}{dx} = \lambda \frac{d^2 T}{dx^2}, \tag{53}$$

where $\varPhi$ is the volume fraction of water. For an aluminum-water mixture, $\varPhi$ takes the following form:

$$\varPhi = \frac{\rho_p}{\rho_p + \rho_{lw}}. \tag{54}$$

Equations (38) and (39) are combined to provide an expression for the heat flux at $x = 0$ in the preheat zone

$$\lambda \frac{dT}{dx}\bigg|_V = r_b\left[2\frac{\rho_{lw}\rho_p}{\rho_{lw}+\rho_p}C_p\left(T_{ign}-T_u\right)+\frac{\rho_{lw}\rho_p}{\rho_{lw}+\rho_p}h_{fg}\right]. \tag{55}$$

The heat flux at $x=0$ in the reaction zone is calculated by taking the spatial derivative of the analytical solution to Eq. (41)

$$\lambda \frac{dT}{dx}\bigg|_G = \frac{\lambda Q_r}{\tau_b r_b C_p}, \tag{56}$$

By matching the two heat fluxes at $x = 0$, an analytical expression for the burning rate is obtained

$$r_b = \sqrt{\frac{\lambda}{\rho_m C_p}\cdot\frac{2Q_r}{2C_p\left(T_{ign}-T_u\right)+h_{fg}}\cdot\frac{1}{\tau_b}}, \tag{57}$$

where ρ_m is the density of the unburned mixture. The parameters that dictate flame propagation are the thermal diffusivity of the mixture, enthalpy of reaction, ignition temperature, and burning time. The inverse dependence of the burning rate on particle size implies diffusion-controlled combustion ([122], [156]). Equation (57) resembles the Mallard-Le Chatelier formula [157] for the flame speed of a homogenous gas-phase mixture, except for the additional term accounting for the energy consumed to vaporize the water.

      The obtained closed-form expression, Eq. (57), is used to estimate the burning rate of a stoichiometric aluminum-water mixture. The particle size and pressure are taken to be 38 nm and 3.65 MPa, respectively. The mean specific heat of the mixture is taken as 2.36 kJ/kg-K. The thermal conductivity of the mixture in the reaction zone is calculated to be 1.21 W/m-K. The density of the mixture is assumed to be equal to the theoretical value of 1800 kg/m^3. The enthalpies of reaction and vaporization of water are taken as 4400 and 1737 kJ/kg, respectively. The burning time is calculated as 0.07 ms. Substituting these values into Eq. (57), the burning rate is estimated to be 7.28 cm/s, which is within the range of 4.66-7.78 cm/s observed in the experiments [138]. The obtained value is sensitive to changes in the burning time used in the model. For example, the burning rate increases from 7.28 to 8.6

cm/s, when the burning time decreases from 0.07 to 0.05 ms. The analysis demonstrates that the proposed model properly accounts for the underlying physicochemical processes. A more accurate result can be obtained by relaxing the simplifying assumptions.

Table 7 Characteristics of aluminum particles

Particle size, nm	Oxide layer thickness, nm	Al content, wt.%
38	3.10	54.3
50	2.10	68.0
80	2.70	75.0
120	0.48	96.5
130	2.20	84.0

Results and Discussion

The theoretical framework is employed to calculate the flame structure and burning rate of stoichiometric mixtures at different pressures and particle sizes. Table 7 shows the characteristics of the particles considered in the present study. The thickness of the oxide layer varies in the range of 0.48-3.10 nm. The active aluminum content decreases with decreasing particle size. The particle composition significantly influences the thermophysical properties of the mixture. As a result, it is important to use an appropriate value of the oxide layer thickness in the calculations. Figure 48 shows the temperature distribution for a stoichiometric mixture containing 38 nm aluminum particles at pressures of 1 and 10 MPa. The temperature increases from an initial value of 298 K in the preheat zone and attains a maximum value of 1800 K in the reaction zone. The thickness of the vapor and reaction zones decrease with increasing pressure. The temperature distribution is further altered by the fact that the vaporization temperature of water increases with pressure. An estimate of the reaction zone thickness is obtained by multiplying the flame propagation velocity and particle burning time. At a pressure of 1 MPa, the estimated value is 6 μm, which agrees reasonably well with the result of the present analysis.

Figures (49)-(51) show the effect of pressure on the burning rates for stoichiometric mixtures containing 130, 80, and 38 nm particles, respectively. For 130 nm particles, the burning rate
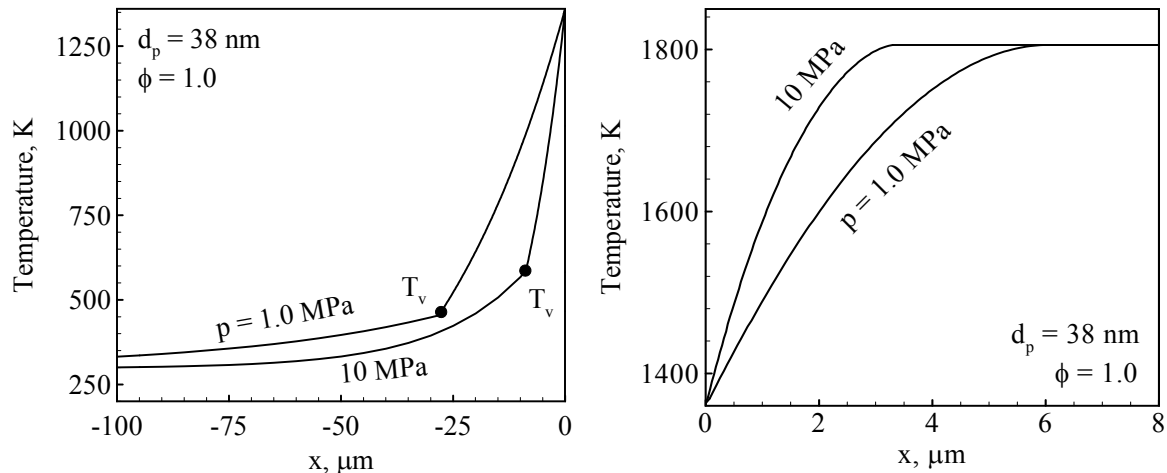
Figure 48 Effect of pressure on temperature distribution of stoichiometric Al-H2O mixture containing 38 nm particles in (a) the preheat zone; (b) the reaction zone

increases from 0.76 to 1.59 cm/s when the pressure increases from 1 to 10 MPa. A similar trend

is observed for the other two cases. For 38 nm particles, the presence of significant scatter in the burning rates can be attributed to the variations in the packing density of the mixture. The actual densities are in the range of 0.75-1.00 g/cm^3, which are lower than the theoretical value of 1.80 g/cm^3. Such a disparity is not observed for 80 and 130 nm particles, since fewer water molecules are absorbed on the particle surface. The burning rate decreases with increasing packing density [138]. It is, thus, not surprising that some of the measured burning rates are greater than the predicted values. The pressure exponent in the burning rate law is ~0.3, which agrees reasonably well with experimental data. In a typical composite solid rocket propellant, the burning rate increases with increasing pressure. A general explanation for this phenomenon is that the flame stand-off distance decreases with increasing pressure, thereby increasing the heat flow to the propellant surface ([158], [159]). In the current study, a visible flame appeared to be attached to the burning surface, since the particles undergo heterogeneous surface reactions. The observed pressure effect can be attributed to the fact that the particle burning time decreases with
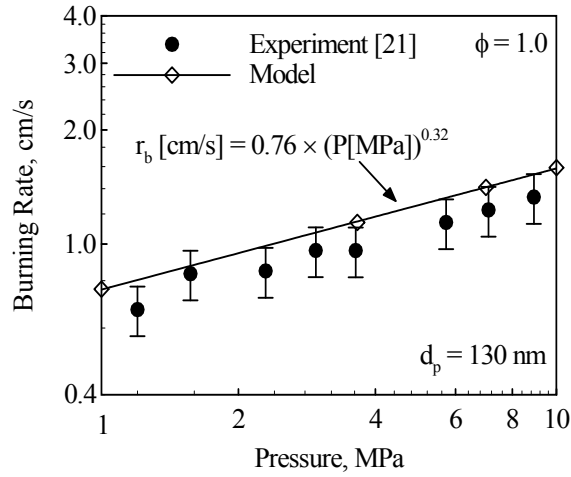
Figure 49 Effect of pressure on burning rates of stoichiometric Al-H2O mixtures containing 130 nm particles.
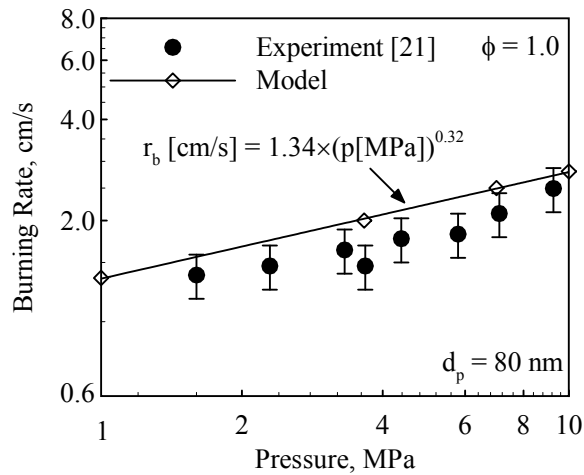
Figure 50 Effect of pressure on burning rates of stoichiometric Al-H2O mixtures containing 80 nm particles
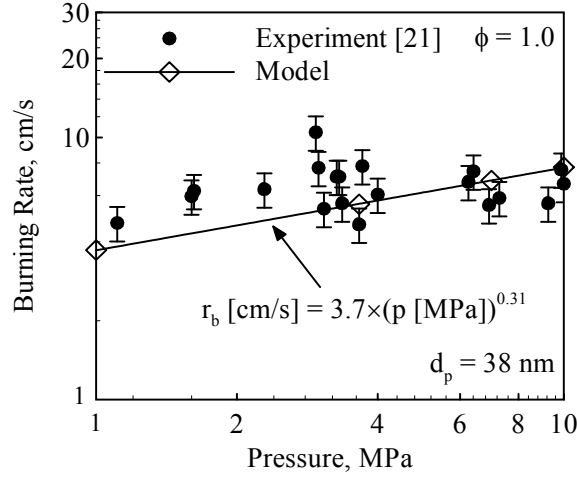
Figure 51 Effect of pressure on burning rates of stoichiometric Al- H2O mixture containing 38 nm particles.

with pressure. Figure 52 shows the effect of particle size on the burning rate for a stoichiometric mixture at a pressure of 3.65 MPa. The burning rate shows a particle size dependence of $r_b = a\, d_p^{\,n}$, with an exponent of -1.15. The experimental data suggest that the burning rate is inversely proportional to the particle diameter [138]. In the present analysis, the particle burning time is assumed to follow d_p^2-law. The actual diameter exponent in the burning-time relationship may be slightly lower than 2, when simultaneous diffusion of water vapor and aluminum are considered [155]. This may explain the observed disparity between the predicted and measured values of the diameter exponent. Figure 53 shows a comparison of the measured and calculated burning rates with those obtained using the following correlation:

$$r_b[\mathrm{cm/s}] = 98.8 \times (p[\mathrm{MPa}])^{0.32}(d_p[\mathrm{nm}])^{-1.0} \tag{58}$$
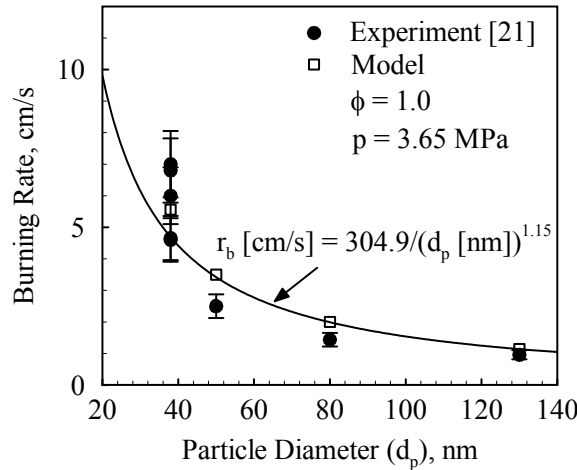
Figure 52 Effect of particle size on burning rate of stoichiometric Al-H2O mixture at 3.65 MPa.

Reasonably good agreement is achieved, which demonstrates the validity of the correlation for situations encountered in the current study. The results support the theory that the rate-controlling mechanism is the mass diffusion through the oxide layers of the particles. In the present analysis, entrainment of particles in the gas flow has been neglected. The experiments indicate that a significant number of particles remained

63

in the quartz tube instead of being transported out of the tube. This may be attributed to the inertial and gravitational forces, particle-particle interactions, and quartz tube wall effects. The region in which particle motion is likely to be important is the post-combustion zone, since the particles are under the continuous influence of the flow of the combustion gas (H_2). This can be incorporated into the model by considering the inertial and gravitational forces, interactions and collisions between particles, and confining effect of the quartz tube. The current model captures the main features of alumimum-water combustion, with reasonably good agreement between experimental data and model predictions.
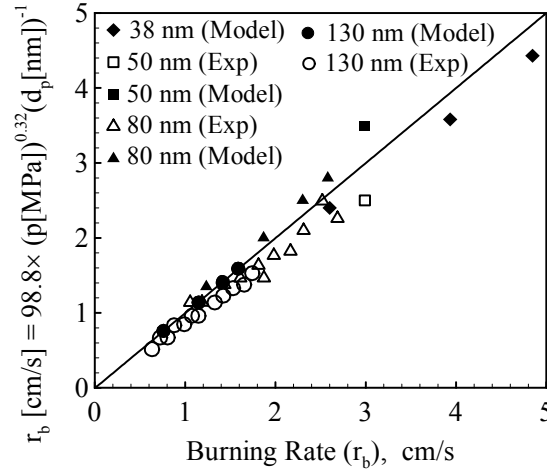
Figure 53 Measured and calculated burning rates vs. curve-fit values for different particle sizes and pressures, $r_b[\text{cm/s}] = 98.8 \times (p[\text{MPa}])^{0.32}(d_p[\text{nm}])^{-1.0}$

The combustion wave propagation of nanoaluminum-water mixtures was studied theoretically and experimentally for particles in the size range of 38-130 nm and over a pressure range of 1-10 MPa. A multi-zone framework was established to predict the burning and flame properties by solving the conservation equations in each zone and imposing mass and energy continuities at the interfacial boundaries. The flame propagation characteristics were measured by burning nanoaluminum-water strands in a constant-volume vessel. Emphasis was placed on the effects of particle size and pressure. An analytical expression for the burning rate was derived, and physicochemical parameters that dictate the flame behavior were identified. For conditions present in the study, the burning rate showed pressure and particle size dependencies of $r_b[\text{cm/s}] = 98.8 \times (p[\text{MPa}])^{0.32}(d_p[\text{nm}])^{-1.0}$. The flame thickness increased with increasing particle size and decreasing pressure. Results supported the hypothesis that the combustion of aluminum-water mixtures is controlled by mass diffusion across the oxide layers of the particles. Future work will specifically examine the effects of particle entrainment and agglomeration on burning properties of nanoaluminum-water mixtures.

C.   **Pyrophoricity of Nano-Aluminum Particles**

Aluminum particles are extensively used in propulsion and energy-conversion applications due to their high oxidation enthalpy, relative safety, and low cost [160]. When a nascent aluminum particle is exposed to an oxidizing environment at room temperature, the chemical reactions between the aluminum atoms and oxidizer molecules result in the formation of an amorphous aluminum oxide (Al_2O_3) layer on the particle surface [161]. Typically, the rate of heat-release due to these chemical reactions is lower than that of heat loss to the surrounding environment. As a result, the particle does not ignite and the thickness of the oxide layer saturates at a value in the range of 0.5-4 nm, depending on the temperature and duration of exposure to the oxidizing gas [161]. The oxide layer protects the aluminum core from further attack of the oxidizer molecules. The ignition temperature of passivated aluminum particles decreases from 2350 K

(melting point of the oxide layer) at 100 μm to 933 K (melting point of the aluminum core) at 0.1 μm [162]. The enhanced reactivity of nano-sized particles poses significant safety hazards. If the size of the particle is decreased below a critical value, the particle could ignite when exposed to an oxidizing gas at room temperature, a phenomenon known as pyrophoricity [163]. It is a major safety issue during particle manufacture, handling, and storage. It can also be employed for useful applications like decoy flare for defending heat-seeking missiles [164]. Reliable measurements or predictions of the critical particle size for pyrophoricity are of paramount interest.

Theoretical studies on metal pyrophoricity are very limited. Glassman et al. [163] postulated that a metal particle is pyrophoric if the chemical energy release is sufficient to vaporize the metal. A quasi steady-state energy balance was performed. For an oxide-layer thickness of 2.5 nm, the critical particle diameter was calculated to be 23 nm. The study ignored the effect of heat losses to the ambient environment and considered bulk material properties. For nano-sized particles, the melting and boiling points [165-171], heat of fusion [168-171], vapor pressure [172-174], ignition temperature [3], and heat of reaction [175] are substantially different from their respective bulk values. Puri [176] estimated the critical particle size by performing transient energy balance in conjunction with the use of size-dependent thermophysical properties. The oxidation was assumed to be controlled by diffusion of oxygen molecules through the gas-phase mixture to the particle surface. The estimated critical particle size is 20 nm. It is worth noting that once a monomolecular oxide layer is formed, the oxidation of nano-aluminum particles is governed by the Mott-Cabrera oxidation kinetics [177,178]. An essential feature of this model is that the metal electrons transverse the thin oxide layer either by thermionic emission or tunneling. The electrons ionize the adsorbed oxygen atoms to create an electrostatic potential between the oxide-oxidizer and oxide-metal interfaces. Figure 54 shows the induced electric field in the particle, which significantly lowers the energy barrier for metal ion diffusion, resulting in higher oxidation rates. Recently, the Mott-Cabrera oxidation kinetics was employed to study the pyrophoricity of nascent aluminum particles [179]. The critical particle diameter was estimated to be 68 nm, which is significantly greater than the values predicted by Glassman et al. [163] and Puri [176]. The study did not consider the size dependence of physicochemical properties. The sensitivity of the results to changes in the model parameters has not been investigated. In addition, the effect of the passivating oxide layer on pyrophoricity of particles needs to be examined.
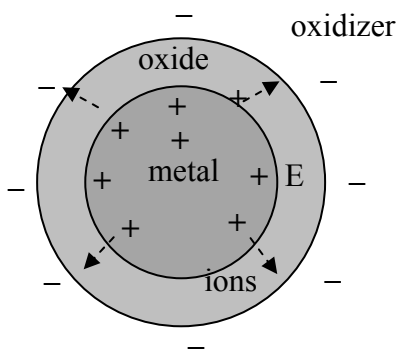
Figure 54 Electric-field across the oxide layer in a spherical nano-particle surrounded by oxidizer molecules (+ positive charge, − negative charge) according to the Mott-Cabrera mechanism [177].

In the present study, a more comprehensive analysis is performed by taking into account transient energy balance along with accurate evaluation of physicochemical properties of nano-sized particles. The oxidation mechanism is based on a recently developed Mott-Cabrera oxidation kinetics, which is applicable for spherical nano-particles [178]. The sensitivity of the model results to the choice of physicochemical properties of the particle and gas, polymorphic state of the oxide layer, parameters of the

Mott-Cabrera oxidation kinetics, and heat-transfer correlation is analyzed. Both nascent and passivated particles are considered. The temperature and pressure of the ambient environment are chosen as 300 K and 1 atm, respectively. Results from the present work are compared with those of previous theoretical and experimental studies. Reasonably good agreement with experimental data is achieved, thereby demonstrating the validity of the model.

Physicochemical Properties of Nano-Sized Aluminum Particles

The physicochemical properties of nano-sized aluminum particles are significantly different from their counterparts of the bulk material [21]. The fraction of atoms on the surface layer of an aluminum particle is given by

$$f = 1 - \left(1 - \frac{2\delta}{D}\right)^3,$$

(59)

where $\delta = 286$ pm and D the particle diameter. It increases from 2 to 92 %, when the particle size decreases from 100 to 1 nm. The surface atoms have lower coordination numbers and higher energies than the atoms in the interior of the particle, thereby leading to size-dependent properties. For example, the melting temperature of a nascent aluminum particle decreases from 937 K at 10 nm to 473 K at 2 nm [165]. The melting point, T_m, and the enthalpy of fusion, L_{fus}, of aluminum particles can be written as [171]

$$\frac{T_m(R)}{T_{m,b}} = \exp\left(-\frac{\alpha - 1}{R/R_0 - 1}\right),$$

(60)

$$\frac{L_{fus}(R)}{L_{fus,b}} = \frac{T_m(R)}{T_{m,b}}\left[1 - \frac{1}{(R/R_0 - 1)}\right],$$

(61)

where R is the particle radius, $\alpha = 1.9186$, and $R_0 = 0.9492$ nm. The subscript b refers to the bulk material.

Another thermophysical property of relevance to the present study is the boiling temperature, defined as the temperature at which the vapor pressure is equal to the ambient pressure. The vapor pressure of aluminum near the surface of a liquid droplet, p_D, is calculated using the Kelvin equation [172]

$$p_D = p_0 \exp(4\sigma v / k_B T D).$$

(62)

where D is the diameter of the particle, k_B the Boltzmann constant, and v the molar volume. The vapor pressure of aluminum over a flat surface, p_0, and the surface tension of aluminum, σ, are calculated respectively as follows [173,174]:

$$p_0 = p \exp\left(13.07 - \frac{36373}{T}\right),$$

(63)

$$\sigma = 948 - 0.202T,$$

(64)

where p is the pressure and T the temperature. Equations (62)-(64) are solved iteratively to calculate the boiling temperature as a function of the particle size. Figure 55 shows the result at
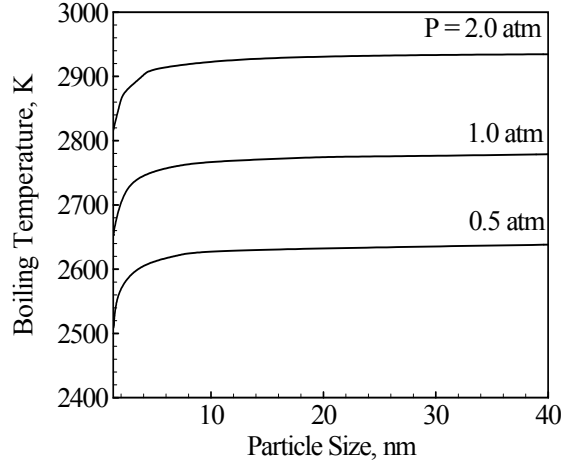
Figure 55 Vaporization temperature of aluminum as a function of particle size over a pressure range of 0.5-2.0 atm.

three different pressures of 0.5, 1, and 2 atm. The boiling temperature of aluminum increases with increasing pressure. It decreases significantly from the bulk value for particles smaller than 10 nm, a trend that is consistent with those observed for the melting temperature and enthalpy of fusion.

The heat of reaction is another physicochemical property that needs to be specified. It determines the energy release during the formation of the oxide layer on a nascent particle. The theoretical data available in Ref. [175] is curve-fitted to obtain a correlation for the heat of reaction of aluminum particles

$$\Delta H_r = -1690 + \frac{865.1}{D^{0.87}},$$ (65)

where ΔH_r is the heat of reaction and D the particle size in nm. The heat of reaction decreases with decreasing particle size. In other words, the oxidation reaction is less exothermic for smaller particles. This effect becomes more substantial for particles smaller than 10 nm.

Another parameter of concern is the density of the aluminum oxide, which exists in many metastable polymorphs. The hexagonally packed α-Al_2O_3 (corundum) has a density of 4 g/cm^3 [161]. Other polymorphs such as γ, δ, and θ phases have face-centered cubic (FCC) structures. The initial oxide layer covering the aluminum particle is amorphous [161]. The density of the amorphous oxide layer is taken to be 3.05 g/cm^3 [161].

Steady Homogenous Gas-Phase Reaction Theory

The analysis presented in Ref. [163] assumes homogeneous gas-phase combustion of aluminum vapor and oxidizing species. It neglects heat losses to the ambient environment and size-dependence of physicochemical properties. Under these assumptions, the critical condition for metal pyrophoricity was obtained by equating the chemical heat release to the sum of the energies needed to heat the particle to its boiling point and vaporize the metal [163]:

$$\frac{\left(1-(\delta/R)_{cr}\right)^3}{\left\{1-\left(1-(\delta/R)_{cr}\right)^3\right\}} = \frac{\rho_{Al_2O_3}\left\{\left(-H_{ox}^o\right)-\left(H_{T_b}^o - H_{298}^o\right)\right\}_{Al_2O_3}}{\rho_{Al}\left(H_{T_b}^o - H_{298}^o + L_{vap}\right)_{Al}},$$ (66)

67
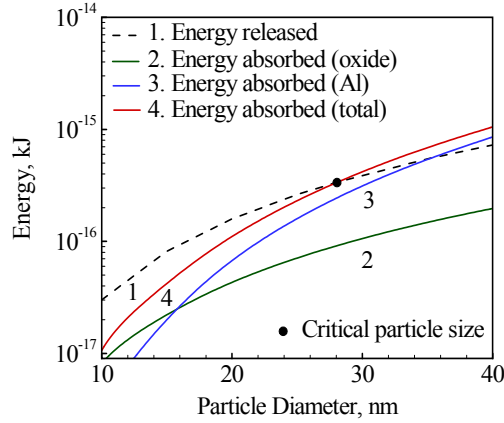
Figure 56 Energy distribution for the oxidation of aluminum particles with an oxide layer thickness of 2.5 nm: steady homogeneous gas-phase reaction theory with bulk material properties

where δ is the oxide layer thickness, ρ the density, T_b the boiling point of aluminum, L_{vap} the enthalpy of vaporization of aluminum, and H the enthalpy. The subscripts ox and cr refer to oxidation and critical condition, respectively. For the sake of comparison, bulk values of thermophysical properties are employed. They are obtained from the JANNAF tables and are given in Table 8 [181]. Figure 56 shows the calculated energy budget of the oxidation process for different particle sizes. The thickness of the oxide layer is chosen as 2.5 nm. The curves corresponding to the total absorbed and released energies intersect at a particle size of 28 nm. The predicted critical particle size agrees reasonably with the value of 28.6 nm reported in Ref. [163], thereby demonstrating the accuracy of the present calculation.

The size-dependent physicochemical properties are used to obtain a revised estimate of the critical particle size. The density of the oxide layer is taken as 3.05 g/cm^3

Table 8 Thermo-physical properties of bulk aluminum and alumina

Property	Value
Density of alumina	4000 kg/m^3
Density of aluminum	2700 kg/m^3
Heat release during oxidation, $-H^o_{298,ox}$	1675 kJ/mol
$H^o_{T_b} - H^o_{298}$	454 kJ/mol
$H^o_{T_b} - H^o_{298} + L_v$	381.67 kJ/mol
Aluminum melting point	940 K
Aluminum boiling point	2740 K
Alumina melting point	2327 K
Alumina volatilization temperature	4000 K
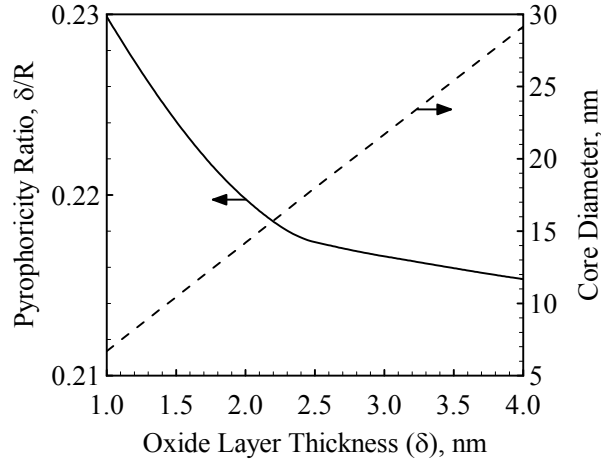
Figure 57 Critical pyrophoricity ratio and core diameter as a function of the oxide layer thickness: steady homogeneous gas-phase reaction theory with size-dependent properties

[161]. Figure 57 shows the variation of the critical pyrophoricity ratio, $(\delta/R)_{cr}$ and particle size with the oxide layer thickness. The former decreases with increasing oxide layer thickness. For an oxide layer thickness of 2.5 nm, it takes a value of 0.217. The corresponding critical particle diameter (inclusive of the oxide layer) is 23 nm, which is lower than the value of 28 nm predicted using the constant-property assumption. The effect of pressure on the critical particle size is also studied in the range of 0.5-2 atm Pressure plays a negligible role in the range of 0.5-2 atm. Note that the above estimates only serve as a guideline, since the analysis neglects the effects of heat losses and kinetics of oxidation of aluminum particles

Transient Heterogeneous Surface Reaction Theory

When a nascent particle is exposed to the oxidizing gas, the temperature, oxide layer thickness, and core diameter vary continuously with time. As a result, the steady-state assumption is not valid. Particle ignition is a transient process, and the corresponding ignition delay can be characterized by the point at which temperature runaway occurs. During ignition, the rate of chemical energy release competes with that of heat loss to the oxidizing gas. An unsteady energy balance is thus required to obtain an accurate estimate of the critical particle size for pyrophoricity. The analysis follows the approach adopted by Mohan et al. [179], but is extended to include the size and temperature dependencies of particle physicochemical properties. Application of the energy conservation leads to the following equation.

$$mC_p \frac{dT}{dt} = \dot{h}_{ox} - \dot{q}_{out}, \tag{67}$$

where m is the mass of the particle, C_p the specific heat of the particle, T the temperature, t the time, $\dot{h}_{ox}$ the rate of chemical energy release. The density and specific heat are calculated as a function of the particle temperature. The rate of heat loss to the surrounding gas, $\dot{q}_{out}$, consists of contributions from conduction and radiation, denoted by the subscripts c and r, respectively, as follows:

69

$$\dot{q}_{out} = \dot{q}_c + \dot{q}_r, \tag{68}$$

In the continuum regime, the conductive heat transfer between the particle and surrounding gas is controlled by energy diffusion, given by [182]

$$\dot{q}_c = 4\pi R \lambda_g \left(T - T_e \right). \tag{69}$$

where R is the particle radius and λ_g the thermal conductivity of the gas. The subscript e refers to the ambient condition. At a temperature of 1000 K and pressure of 1 atm, the mean free path of oxygen molecules is 223 nm, which is significantly greater than the particle size. As a result, the continuum heat transfer correlation ceases to be valid. In the free-molecular regime, the conductive heat-flux is replaced by the molecular heat flux, $\dot{q}_{mol}$, given by [183]:

$$\dot{q}_{mol} = \alpha \pi R^2 \frac{p_e \sqrt{8 k_B T_e / \pi M}}{2} \left(\frac{\gamma^* + 1}{\gamma^* - 1} \right) \left(\frac{T}{T_e} - 1 \right), \tag{70}$$

where M is the mass of the oxygen molecule, γ^* the adiabatic constant calculated at a temperature $T^* = (T+T_e)/2$, and $\alpha = 0.85$ the accommodation coefficient [184]. The radiation heat transfer can be calculated using the Stefan-Boltzmann relation:

$$\dot{q}_r = \varepsilon A \sigma \left(T^4 - T_e^4 \right), \tag{71}$$

where A is the particle surface area, σ the Stefan-Boltzmann constant, and $\varepsilon = 0.2$ the emissivity of the oxidized aluminum surface [185]. Equation (13) is strictly not valid for nano-sized particles.
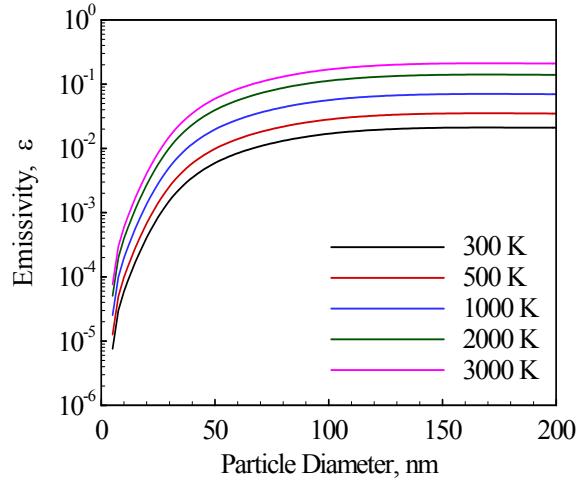
Figure 58 Effect of particle size on emissivity of aluminum nano-particles at different temperatures obtained using the magnetic dipole approximation theory [186]

The size and temperature dependencies of the particle emissivity must be considered. Figure 58 shows the effect of particle size on the emissivity of aluminum particles at different temperatures calculated using the magnetic dipole approximation theory given in Ref. [186]. The emissivity of nano-sized aluminum is several orders of magnitude lower than its bulk value. A more accurate value of the particle emissivity can be obtained by considering the electrical dipole contribution, which may become

70

significant at higher temperatures [187]. The analysis, however, indicates that the model results are insensitive to changes in the particle emissivity.

The heat-release term is calculated using the Mott-Cabrera oxidation kinetics [188]. Ermoline and Dreizin [189] incorporated the electric-field correction and effects of volume changes in a growing oxide layer and a shrinking aluminum core, and derived the following equations for spherical particles:

Table 9 Constants in Mott-Cabrera equations

Constant	Value
n	10 nm^{-2}
v	10^{12} s^{-1}
a	0.12 nm
φ_m	-1.6 V
W	2.6 eV
q	3e
Ω_1	-0.0166 nm^3
Ω_2	0.023 nm^3

$$\frac{d\delta}{dt} = \left[(\Omega_1 + \Omega_2) \left(\frac{R_c}{R} \right)^2 - \Omega_1 \right] nv \exp\left(-\frac{W}{k_B T} \right) \exp\left(-\frac{qa\phi_M}{k_B T} \frac{R}{R_c \delta} \right),$$

$$\frac{dR_c}{dt} = \Omega_1 nv \exp\left(-\frac{W}{k_B T} \right) \exp\left(-\frac{qa\phi_M}{k_B T} \frac{R}{R_c \delta} \right),$$

(72)

where R_c is the core radius and δ the oxide layer thickness. The model constants are given in Table 9. The rate of chemical heat release can be written as

$$\dot{h}_{ox} = 4\pi R_c^2 \rho_{Al} h_r \frac{dR_c}{dt},$$

(73)

where h_r is the heat of reaction. Equations (72) and (73) require the presence of an oxide layer on the particle. The formation of the monomolecular oxide layer on a nascent particle is extremely fast and can be treated as an adiabatic process [190]. A detailed justification is given in Ref. [190]. Our calculations indicate that the growth of the oxide layer is adiabatic up to a thickness of 0.3 nm. This further demonstrates the validity of the assumption. As a result, chemical equilibrium analysis can be performed to calculate the particle temperature upon the formation of the 0.3-nm thick (monomolecular) oxide layer. No such calculation is necessary for passivated particles. The energy balance based on chemical equilibrium analysis can be written as

$$\left(m_{Al} C_{p,Al} + m_{ox} C_{p,ox} \right) \left(T_f - 300 \right) + m_{Al} L_{fus,Al} = -m_{ox} h_{ox},$$

(74)

where T_f is the final temperature.

Results and Discussion

The theoretical framework described in Section 4 is used to analyze the pyrophoricity of nascent and passivated aluminum particles at nano scales. Initially, the nascent particle is assumed to be devoid of

71

the oxide layer. For passivated particles, the initial values of the oxide layer thickness in the range of 0.3-0.5 nm are considered.

Nascent aluminum particles

The growth of an oxide layer on a nascent aluminum particle is divided into two stages. In the first stage, a 0.3-nm thick monomolecular oxide layer is formed. A chemical equilibrium analysis is performed to calculate the particle temperature after the formation of the oxide monolayer. A companion transient energy balance analysis employing the Mott-Cabrera kinetics is conducted to determine the minimum ignition temperature for particles
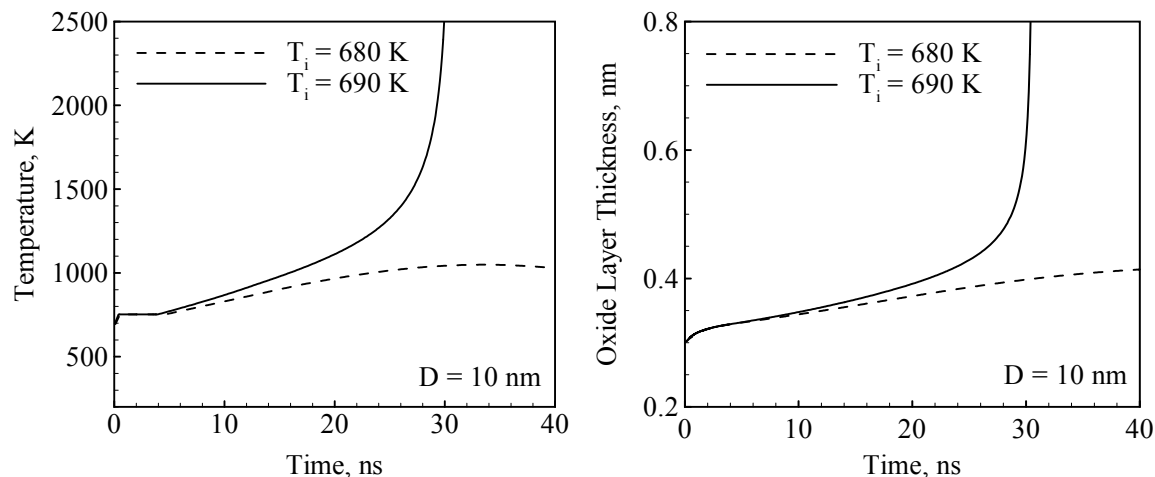
Figure 59 Variations of particle temperature and oxide thickness with time for a core diameter of 10 nm and oxide layer thickness of 0.3 nm.

encapsulated with a 0.3-nm thick oxide layer. Ignition is assumed to be achieved when the particle temperature increases monotonically beyond the melting point of the oxide film. If the ignition temperature is lower than the result of chemical equilibrium analysis, the particle can self-ignite due to heterogeneous oxidation reactions beginning at 300 K. It is, thus, considered to be pyrophoric. Figure 59 shows the variations of the temperature and oxide layer thickness with time for a particle with a core diameter of 10 nm. For an initial temperature of 680 K, the rate of chemical heat-release is not sufficient to balance the heat loss to the ambient environment. As a result, temperature runaway does not occur. The isotherm corresponds to the melting of the core at 750 K, which is lower than the bulk melting point of aluminum by 183 K. The oxide layer thickness follows a similar trend. When the initial temperature is chosen as 690 K, the temperature and oxide layer thickness increase sharply after a time period of 20 ns. The rate of chemical energy release is significantly greater than that of heat loss to the ambient environment. The same phenomenon takes place for all temperatures greater than 690 K. For a particle with a 10 nm core, the minimum ignition temperature is, thus, taken as 690 K. The sensitivity of the results to the ambient temperature stems from the fact that the reaction rate bears an exponential dependence on temperature. A similar analysis is performed for different particle sizes and the corresponding minimum ignition temperature is determined.

Figure 60 shows the comparison of the results of chemical equilibrium and transient energy balance analyses for two different cases. In the first case, bulk material properties calculated at room temperature are employed. A crystalline aluminum oxide layer with a density of 4.0 g/cm^3 is assumed to cover the active aluminum surface. In the second case, size and temperature dependent properties are used and an amorphous oxide layer with a density of 3.05 g/cm^3 is considered. The chemical equilibrium analysis indicates that the final particle temperature decreases with increasing particle size, since more energy is spent to heat a larger particle. The transient energy balance analysis, on the other hand, suggests

72

that the minimum ignition temperature increases with increasing particle size, since the rate of heat loss to the oxidizing gas is proportional to the particle surface area. The plateau-like feature indicates that the corresponding particles need to be pre-heated to the melting point of the core. These two curves intersect at the critical particle size, the specific value of which is different for the two cases. For
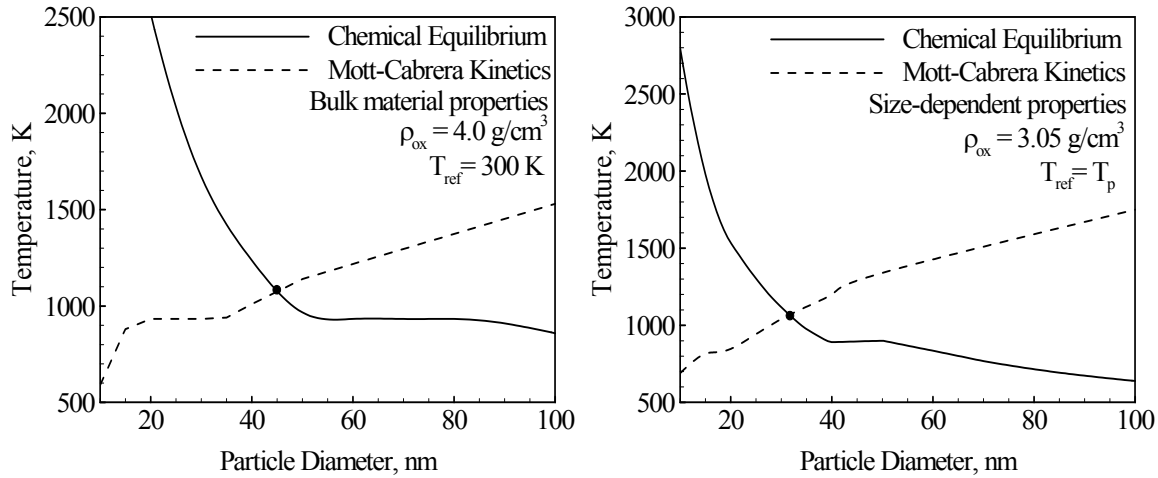
Figure 60 Particle temperature upon growth of 0.3 nm oxide layer and minimum temperature necessary for ignition for (a) crystalline oxide layer and bulk material properties at room temperature; (b) amorphous oxide layer with temperature and size dependent material

the first case, the calculated value is 45 nm, which is comparable with the estimate reported in Ref. [190]. For the second case, the critical particle size is predicted to be 32 nm. The model results were sensitive to the changes in the parameters of the Mott-Cabrera oxidation kinetics. For example, increasing the Mott potential from 1.6 to 1.75 V resulted in an increase in the critical particle size by 18 %. In the above analyses, the free-molecular regime heat transfer model is employed. Figure 61 shows the result when the continuum hypothesis is invoked. It overestimates the heat losses to the ambient environment. As a result, particles need to be heated to higher temperatures for ignition to occur. The calculated critical particle size of 18 nm is significantly lower than the value obtained using the model for the free-molecular regime. The continuum heat transfer correlation gives inadequate description of ignition and combustion of nano-sized particles. Table 10 shows the comparison between the predictions of different models
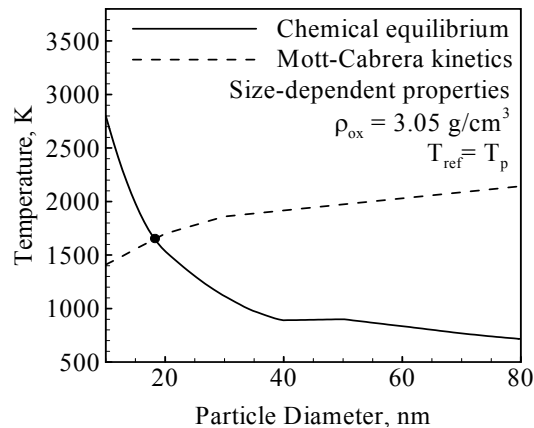
Figure 61 Critical particle size predicted using the continuum heat transfer correlation

and experimental data. Results from the present analysis exhibit reasonably good agreement with measurements.

Table 10 Critical particle size predicted by different models and their comparison with the experimental data

Model			Critical particle size, nm
Steady-state, homogeneous gas-phase reaction theory	Constant properties [163]		23
	Size-dependent properties		18
Transient heterogeneous surface reaction theory	Diffusion oxidation model [176]		20
	Mott-Cabrera kinetics	Free molecular	32
		Continuum	18
Experimental data [163]			30

In the above analysis, thermal accommodation coefficient was taken as 0.85. In reality, the accommodation coefficient is a temperature dependent parameter [187]. Figure 62 shows the result when temperature dependence of the thermal accommodation coefficient is considered. The accommodation coefficient decreases with increasing temperature and a result the critical particle size increases from 32 nm to 40 nm.
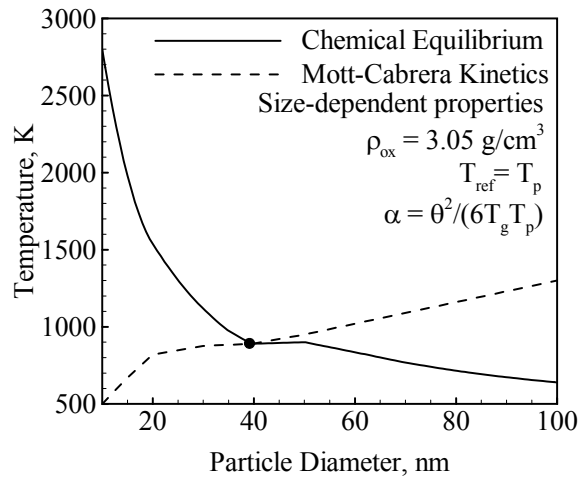
Figure 62 Critical particle size predicted using the free-molecular heat transfer correlation in conjunction with temperature dependent accommodation coefficient.

Passivated aluminum particles

The same approach outlined previously is adopted for passivated aluminum particles, except that the chemical equilibrium analysis is not employed. The oxide layer thickness is varied in the range of 0.3-0.5 nm. Figure 63 shows the temporal evolution of the temperature for particles with a core diameter of 3.8 and 6 nm along with an oxide layer thickness of 0.3 nm. At 300 K, temperature runaway is observed only when the particle size is 3.8 nm and, thus, the critical particle size is 3.8 nm. Figure 64 shows the

temperature evolution for a core diameter of 3.8 nm and shell thickness in the range of 0.3-0.5 nm. Particles with 0.4 and 0.5 nm thick oxide layers remain stable at 300 K, suggesting that oxide layers thicker than 0.3 nm render the particle to be non-pyrophoric. Aluminum particles are typically covered by an oxide layer, which can have
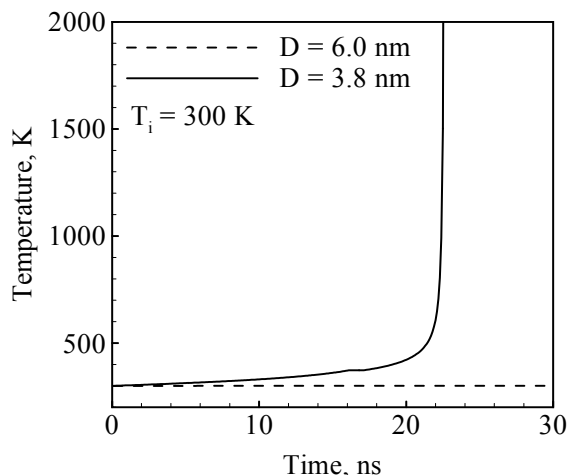
Figure 63 Variation of particle temperature with time for core diameters of 3.8 and 6 nm and oxide layer thickness of 0.3 nm.

thickness in the range of 0.5-4 nm [161]. Moreover, particles smaller than 3.8 nm are not of practical interest. As a result, commercially available passivated particles are found to be non-pyrophoric.
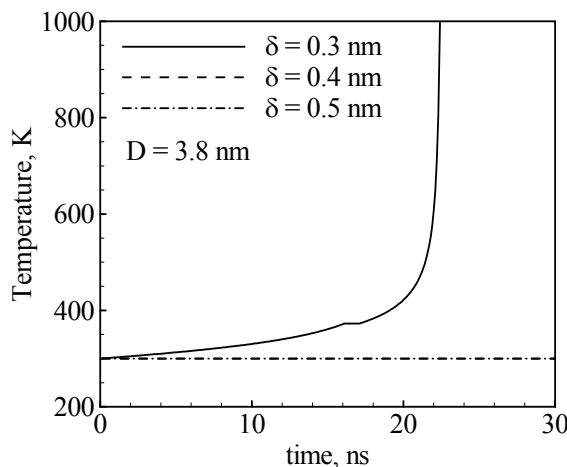
Figure 64 Variation of particle temperature with time for a core diameter of 3.8 nm and oxide layer thickness of 0.3, 0.4, and 0.5 nm

Pyrophoricity of nano-sized nascent and passivated aluminum particles in air was studied based on a transient energy balance analysis. The work considered radiation and molecular heat exchange with the surrounding environment and employed the Mott-Cabrera oxidation mechanism for the heterogeneous chemical reactions that occur on the particle surface. The size-dependence of physicochemical properties of the particle is also incorporated. Results suggested that nascent aluminum particles with diameters lower than 32 nm are pyrophoric. The critical particle size for particles passivated with a 0.3 nm thick oxide layer was calculated as 3.8 nm. Commercially available nano-scale aluminum particles with an oxide-layer thickness in the range of 0.5-4.0 nm were predicted to be non-pyrophoric. The model results

75

were sensitive to the choice of physicochemical properties, the Mott-Cabrera oxidation parameters, and the polymorphic state of the oxide layer. The continuum hypothesis gave inadequate description of pyrophoricity of aluminum particles at nano scales.

IV.   Experimental Studies on Nanometer Aluminum and Composite Micron Particles with Nanometer Features (Purdue University)

A.   Studies of the reaction of Aluminum with H_2O and H_2O_2

Over the past few years, the combustion of nano-aluminum/water (nAl/ H_2O) propellants has been widely reported, but further progress has been slowed for the following reason: the loosely correlated trends in combustion data are insufficient in guiding further research efforts, and they cannot be used to significantly improve the Isp observed in static rocket motor tests. It was previously found that different mixing techniques (hand, planetary and resonant mixers, duration and temperature), or equivalence ratio gave rise to different burning rates, but the influence of pH and rheology on nAl/ H_2O propellants was not considered. We have found in our studies that the effects of pH on nAl/ H_2O propellants are profound, and correlate well with viscosity, low pressure deflagration limits, burning rate exponents, and rocket motor performance. Our findings suggested that coagulation can influence the pressure exponent over a wide range of values (0.34–0.68). For particle diameters <1 μm, dispersion during mixing is affected more by electrostatic repulsion from charged ions than from mechanical agitation, and this is reflected through zeta potential and viscosity measurements at different pH levels. Additionally, we observed that pH has an influence on nAl/H_2O reaction kinetics during ignition, as the propellant transitions from low temperature oxidation to high temperature combustion.   See DOI: 10.1080/00102202.2012.759948 for more details. Also see DOI: 10.1002/prep.201200143 for other work characterizing safety, aging and equivalence ratio effects on nAl and water reactions.

We also completed studied involving the burning rate characteristics of hydrogen peroxide and micron-aluminum propellants. Theoretical calculations show that the sea level specific impulse of this simple binary mixture is comparable to standard composite propellant. In addition, the aluminum particle size, hydrogen peroxide concentration, and mixture ratio can be adjusted over a flat peak performance regime to attain specific thrust profiles and durations. We measured the burning rates in a windowed pressure vessel at pressures ranging from 7 to 14 MPa. Results show that mixture burning rates span from 0.5 to 4.5 cm/s at 7 MPa with power law burning rate pressure exponents ranging from 0.33 to 1.07. In this study, we focus a statistical analysis on the determination of the most influential variables affecting the burning rate and applied a thermal analysis to determine the combustion regimes of these mixtures. The statistical analysis provided a multivariate regression model for the logarithm of the burning rate with a correlation coefficient of 0.93. The model suggests aluminum diameter is the most important factor affecting the overall burning rate, and H_2O_2 concentration as the most influential variable on the burning rate pressure dependence. The burning rate dependence on theoretical combustion temperature shows two distinct combustion regimes attributed to kinetic and diffusion controlled combustion. A simple thermal analysis confirms the experimental burning rate pressure dependence observed for these two regimes. See DOI: 10.1016/j.combustflame.2012.10.001 for more details.

B.   Encapsulating Nanoscale Particles in Oxidizer Crystals

The addition of nanoparticles to composite propellant formulations theoretically leads to dramatically increased burning rate and combustion efficiency. However, nanoparticles have played a severely limited role in modern propellant formulation development thus far because of undesirable resulting properties. The literature is replete with examples of unworkable viscosities during processing, brittle finished products, poor combustion efficiency, and/or combustion stability problems during use. These issues ultimately are a result of the high surface area (25–250 m2g-1) of the nanoparticles preferentially adsorbing the liquid propellant binder components during processing, preventing complete

dispersion and reducing the capability of the binder matrix to retain other propellant ingredients. Including nanoscale Energetic crystals with nanoparticle inclusions were prepared and characterized, focusing on the nanosized iron(III) oxide-ammonium perchlorate system, generated using an ethyl acetate/acetone antisolvent:solvent system. We have shown that capture is dependent on antisolvent-to-solvent ratio; increased quantities of antisolvent lead to faster nucleation rates, smaller crystals, and improved capture. Additionally, the crystal habit formation is modified by the addition of nanoparticles, resulting in highly uniform rod-like crystal structures. Results with nanoaluminum-ammonium perchlorate and nanoaluminum-cyclotrimethylenetrinitramine (RDX) systems have shown similar capture behavior. See DOI: 10.1002/prep.201200142 for more details.

C.   Inclusion Materials in Micron Scale Aluminum

Micrometer-sized aluminum is widely used in energetics; however, performance of propellants, explosives, and pyrotechnics could be significantly improved if its ignition barriers could be disrupted. We report morphological, thermal, and chemical characterization of fuel rich aluminum polytetrafluoroethylene (70–30 wt-%) reactive particles formed by high and low energy milling. Average particle sizes range from 15–78 μm; however, specific surface areas range from approx. 2–7 m^2g^{-1} due to milling induced voids and cleaved surfaces. Scanning electron microscopy and energy dispersive spectroscopy reveal uniform distribution of PTFE, providing nanoscale mixing within particles. The combustion enthalpy was found to be 20.2 kJg-1, though a slight decrease (0.8 kJg-1) results from extended high energy milling due to α-AlF3 formation. For high energy mechanically activated particles, differential scanning calorimetry in argon shows a strong, exothermic pre-ignition reaction that onsets near 440 ºC and a second, more dominant exotherm that onsets around 510 ºC. Scans in O2-Ar indicate that, unlike physical mixtures, more complete reaction occurs at higher heating rates and the reaction onset is drastically reduced (approx. 440 ºC). Simple flame tests reveal that these altered Al-polytetrafluoroethylene particles light readily unlike micrometer-sized aluminum. Safety testing also shows these particles have high electrostatic discharge (89.9–108 mJ), impact (>213 cm), and friction (>360 N) ignition thresholds. These particles may be useful for reactive liners, thermobaric explosives, and pyrolants. In particular, the altered reactivity, large particle size and relatively low specific surface area of these fuel rich particles make them an interesting replacement for aluminum in solid propellants. See DOI: 10.1002/prep.201200102 for more details. Fluorinated graphite, poly(carbon monofluoride) (PMF), was also considered as an inclusion material because of its vastly different mechanical properties. See DOI: 10.1002/prep.201200202 for more details.

V.   Investigation of Solid Oxidizer and Gaseous Fuel Combustion Performance Using an Elevated Pressure Counterflow Experiment for Reverse Hybrid Rocket Engine (Penn State including Grant Risha, Penn State-Altoona, and Greg Young, Naval Surface Warfare Center, Indian Head)

Pressurized counterflow burner and static-fired motor studies were conducted to explore the possibility of a reverse hybrid system, having a solid oxidizer and gaseous fuel. Theoretical performance analysis indicates such a system may yield specific impulse and density specific impulse similar to composite solid propellants, yet with the added capability to throttle, shut down, and restart firings. Pressurized counterflow flame studies, conducted using pressed ammonium perchlorate (AP) pellets and gaseous ethylene, show three pressure dependent combustion regimes. These results, along with published results from Hightower and Price [188], Boggs [189], and Atwood et al. [190] are presented in Figure 65.
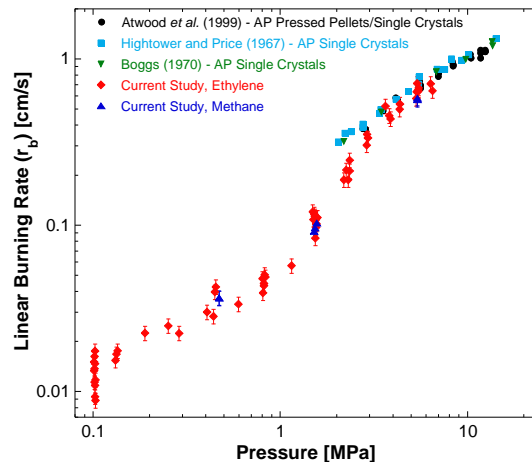
Figure 65 Counterflow burning rates as a function of pressure, compared to published data (Hightower and Price [188], Boggs [189], Atwood et al. [190]).

Ammonium perchlorate decomposition, for pressures below 1 MPa, is controlled by heat transfer from the resulting fuel/oxidizer diffusion flame, which forms between the fuel and decomposition products of AP. In this low pressure regime, the AP burning rate is found to increase with flame strain rate and pressure, yielding measured values between 0.1 to 0.5 mm/s. As pressure increases, the monopropellant flame moves closer to the oxidizer surface until the pressure reaches the self-decomposition limit near 3 MPa, at which point the monopropellant flame becomes nearly independent of the diffusion flame. Further increasing the pressure yields burning rates between 0.4 to 0.7 cm/s, which are consistent with the literature. Variation of flame strain rate under these conditions has little or no influence on the AP burning rate for the range of flow conditions tested. Similar studies conducted with methane suggest burning rates are not affected by fuel type. Lab-scale static motor firings were conducted to examine ignition, variation of fuel flow rate and initial motor pressure, and system performance. Results indicate that successful motor operation requires initial pressures capable of boosting the system into the higher burning rate regimes of AP. Ignition at low pressures results in long startup periods where the motor operates as a gas generator.

VI. Hierarchical Theoretical Methods for Understanding and Predicting Anisotropic Thermal Transport and Energy Release in Rocket Propellant Formulations (Thomas D. Sewell (PI), Chemistry, U. of Missouri-Columbia)

There is a strong push to explore possibilities for new explosives and propellants based on novel combinations of traditional polymer fuels, ionic salt oxidizers, metals, metal oxides, and CHNO energetic materials and less traditional materials such as nanoparticles, thermites, graphene, carbon nanotubes (CNTs), and boron, among others. While equilibrium thermodynamics calculations yield estimates of overall theoretical energy release for a given propellant formulation with arbitrary combinations of both traditional and exotic ingredients, they do not account for non-equilibrium spatio-temporal processes of transport and chemistry on "sub-continuum" spatial scales and mesoscopic interactions among the propellant ingredients that determine the energy release rates and performance. When gross theoretical considerations based on simple thermodynamic equilibrium are used to predict specific impulse and stability criteria for a given propellant formulation, those estimates often are poor and hence deemed not predictive when compared with results from experimental measurement and testing.

One approach for achieving theoretically based performance limits is to more carefully prescribe the interactions of the propellant ingredients in intimate contact and the nature of mixing and chemistry of reactants and products during microstructural decomposition and burning. Improved and systematic

78

descriptions that consider detailed non-equilibrium processes (when viewed at the macroscale or system level scale) can lead to better predictions and enable the generation of new propellant designs. New designs aimed at enhanced performance will use smaller and more precisely engineered particles, approaching the nanometer scale, to increase the proximity between interacting propellant ingredients; use orientation, placement, and the intrinsic anisotropy of material behaviors of the individual ingredients as a path toward thermal management of the system in the pre- or early-reaction stages; and use engineered microstructures on the representative volume element (RVE) scale and above to achieve desired mixing and reactive flow properties on the mm scale.

An attractive approach for developing new designs is to use self- and direct-assembly to generate highly controlled nano- and microstructure that will typically yield close intimacy but with additional degrees of freedom, corresponding to placement and orientation of ingredients, that will enable precise tailoring of properties. Such materials are usually layered or tiled, with well-defined orientable crystalline or quasi-crystalline properties. In general, such directed assemblies will exhibit anisotropy that extends beyond that associated with the individual ingredients. This allows one to exploit the intrinsic anisotropy in the mechanical and electromagnetic properties of individual propellant ingredients and moreover to impose *hierarchical* design at the nano- and microscales, a feature we refer to as *hierarchical anisotropy*. Together, these should make it possible to cause directionality in the overall reaction and energy release profile in propellants. Some possible methods of achieving this that we will study include use of anisotropic assemblies such as bundles of reacting linear chains of nanoparticles, anisotropic wave propagation engineered in *via* anisotropic crystalline structures, or anisotropic combustion engineered using highly anisotropic thermal conductors such as graphene sheets.

The efficacy of new propellants based on hierarchically anisotropic materials depends on structures in the unreacted material, but also on the influence of these structures in the decomposing and burning propellant. Therefore, it is useful to think of anisotropy at three levels:

1) Intrinsic anisotropy at the molecular up to the continuum microscale for pure constituents
2) Manufactured nano- and microscale anisotropy that is induced by manufacture specifications of the composition that identifies the material selection, gross stoichiometry, morphology, and constituent placement and orientation
3) Mesoscale anisotropy persistence during the physico-chemical structural decomposition, mixing, and reactive processes, templated by item 2), that results in locally anisotropic effects that appear homogenized at the engineering device-level scale that ultimately defines the performance characteristics of the propellant.

The goal of our effort is *a focused, integrated program of fundamental theoretical and computational research designed to yield understanding and predictive capability regarding anisotropic thermal transport and energy release in advanced rocket propellants*. The proposed research will contribute to a practical capability for the *a priori* design of smart, functional propellant materials based on intelligently designed polymer nanocomposite formulations augmented by non-traditional additives or passivation agents, possibly coupled to external fields.

Our approach is to develop a hierarchical theoretical framework that combines, with as much rigor as possible:

- Fundamental information from atomic-scale simulations
- Detailed continuum-based mesoscopic models of interfaces and interphases, phase transformations, multi-phase transport, and chemistry
- Explicit microstructure-resolved RVE scale and larger simulations that generate homogenized results induced by mesoscale constituents
- Development of approaches that define engineering-scale models for propellant combustion uniquely defined by the hierarchical structures from the molecular, micro-, and mesoscopic models. These engineering-scale models are the ones that can be used to make system performance estimates.

Atomic-scale methods – molecular dynamics (MD) and electronic structure theory – are being used to predict the details of:

- Thermo-mechanical and transport properties
- Thermodynamic phase diagrams
- Interfacial structure and processes
- Ignition chemistry in multiple phases and mixing regimes.

The simulations are being done for conditions of temperature, stress-/strain-state, and tensoral strain rate relevant to propellant ignition and initiation and are being provided to the mesoscale and continuum scale theorists for direct use in their models/predictions.

Mesoscopic continuum-based models are being developed for chemically reactive materials. The general approach taken follows standard methodologies used in the combustion community, but includes the complexities associated with anisotropy and heterogeneity that _must_ be considered to describe nano- and microscale physical processes and their effects on chemistry. Those include consideration of phase changes including solid-state polymorphism and transitions among solid, liquid, and gas; and tracking of key species diagnostic of or critical to the overall reaction kinetics. Multiphase diffusion of species and diffusion of oxidizing and metal ions in oxide melt solutions (often thought to be involved in metal, intermetallic, and thermitic reactions) are being included. The mesoscopic models will predict:

- Multiphase decomposition and reaction during chemical energy release at initially separate diffusive/reactive interfaces
- Volumetric reaction and gaseous combustion
- Formalism and constitutive theory used to describe reactants and their products that reflect the underlying material mechanics and physical chemistry of the constituents
- Emission outputs (spectra) for "tagged" species in the continuum simulations that can be used to generate synthetic spectra for comparison to experiment.

Thus, we will generate highly constrained model simulations of multiphase decomposition and combustion events for which model spectra output *can be compared directly* to both experiments and MD simulations to develop temporally and spatially accurate reaction kinetics.

On the basis of the mesoscopic models we are developing *RVE-scale methods* for simulating experimentally relevant configurations such as:

- 1-, 2- and 3-D laminates and plies
- Spherical core/shell particles
- Both periodic and stochastic microstructure with designated distributions of materials.

Ultimately we will simulate a piece of material sufficiently large to yield, in a proper homogenization over the "microscopic" ensemble, statistical distributions of properties that can be used in macro-scale models.

During the third year of the overall project, considerable effort was devoted to developing the fundamental methods to be applied in the successive years of the project. The work is essentially on track compared to what was proposed originally. A brief summary from each participating institution is provided below.

A. Development and implementation of atomic-scale methods for computing thermal-mechanical-chemical properties (Thomas D. Sewell and Donald L. Thompson**, U. of Missouri-Columbia)**

Efforts in the third year were focused on the development and implementation of atomic-scale methods for computing thermal-mechanical-chemical properties that will be provided directly to the mesoscopic (Matalon and Stewart at UIUC) and macroscopic (Ortiz at Caltech) modelers on the project. The materials, properties, and thermodynamic states were chosen in cooperation with those modelers. The major areas of emphasis at the University of Missouri-Columbia during the this year were:

- Anisotropic thermal conductivity in triclinic crystalline compounds

80

- Second-order elastic tensor for triclinic crystalline compounds for finite temperatures and pressures
- Calculations of plasticity in the basal plane of the crystalline energetic material TATB
- Melting point of anisotropic crystals, both at normal and elevated pressure
- Liquid state transport coefficients as functions of temperature and density
- Force field development for TATB and FOX-7
- Electronic structure predictions of the transformation from acid-base pairs (e.g., nitric acid and ammonia) to ion pairs (e.g., NH_4^+ and NO_3^-), that is, proton transfer, in small clusters of ammonium nitrate $(AN)_n$ and ammonium perchlorate $(AP)_n$ containing $n \geq 1$ formula units of AN or AP.
- Electronic structure calculations of the oxidation of Al by CO_2

Molecular dynamics (MD) and molecular mechanics (MM) simulations were used to predict the thermal and mechanical properties of the insensitive energetic material 1,3,5-triamino-2,4,6-trinitrobenzene (TATB) in both the crystalline and liquid states. Although it is not used as a propellant ingredient, TATB crystallizes in a triclinic space group (the lowest symmetry class) and, therefore, codes and analysis tools developed for TATB should be applicable to all other molecular energetic materials. Progress was also made toward the development of a flexible-molecule force field for 1,1-diamino-2,2-dinitroethene (FOX-7), which is of potential interest as a propellant additive.

Proton transfer is often thought to be an early reaction in the decomposition of inorganic salts such as ammonium nitrate (AN) and ammonium perchlorate (AP), which are commonly used oxidizers. As an initial stage of developing chemical decomposition schemes for AN and AP, electronic structure (quantum chemistry) calculations were performed to study the transformation from the stable acid-base pair for isolated formula units to stable ion pairs, as described in the bulleted list just above. In addition to calculations for pure $(AN)_n$ and $(AP)_n$, the effects of NH_3, AlH_3, and BH_3 molecules on cluster acid-base/ion-pair stability were studied.

B. Development of Mesoscale Simulations and Theory for Multi-Material and Polycrystalline and Microstructured Materials (Michael Ortiz, Caltech)

The work tasked to Caltech is concerned with the development of mesoscale simulations and theory for multi-material and polycrystalline and microstructured materials. Specific subtasks are the generation of useable, verified and validated material descriptions, mixtures and interfacial material interactions that can be directly incorporated into any larger continuum-based computational framework. A primary focus of the work specifically concerns the development of hierarchical theoretical methods for understanding and predicting anisotropic thermal transport and energy release in rocket propellant formulations. An even more specific focus concerns the development of understanding and predictive capability regarding anisotropic thermal transport and energy release in advanced rocket propellants, leading to a practical capability for *a priori* propellant design. Propellants have traditionally been modeled using hydrocodes that neglect entirely the strength of the material. However, recent work (Kroonblawd & Sewell, *J. Chem. Phys.*, 2013) has shown that the thermal conductivity of energetic materials such as TATB can be extremely anisotropic, with conductivity contrasts of orders of magnitude depending on transport direction. It seems likely that this extreme anisotropy should in turn result in a strong directional dependence of reaction-front speeds, a phenomenon that appears to be poorly understood at present. This acute sensitivity to local anisotropy in turn raises opportunities for the optimal design of microstructures resulting in enhanced engineering properties of propellants, such as specific impulse, a design tradeoff that also appears to be unexplored at present.

Work at Caltech to date has progressed on two different fronts, described next in turn.

	Molecular dynamics	**N.E. Stat. Mech.**
Configuration space	Phase space (q,p)	•Temperature field •Molar-fraction field
Governing equations	$\Sigma F = ma$	•Diffusive transport (heat and mass)
Spatial resolution	Atomic lattice	•Temperature grads. •Concentration grads.
Temporal resolution	•Thermal vibrations •Transition states	•Continuum dynamics •Diffusional transients
Time-scale bridging	Non-equilibrium statistical mechanics	
Spatial-scale bridging	Quasicontinuum method	

Figure 66 The paradigm shift: From Newtonian dynamics to diffusional transport (heat and mass)
Time step limited by diffusional time scale

Fundamental understanding of the effect of anisotropy on reaction-front speeds. The essential difficulty in developing such understanding is the multiscale nature of the phenomenon, which includes both atomic level rate-limiting processes, such as thermal vibrations and bond breaking, collisions, coupled to slow processes such as heat and mass transfer, viscosity and complex reactions paths. Indeed, the challenge of performing atomistic full-chemistry simulations over time-scales relevant to macroscopic chemical processes and diffusion-mediated phenomena constitutes a long-standing—yet stubbornly elusive—goal in computational science. For propellants, the time-scale gap is staggering, from thermal vibrations (femtosecond) to device operation (seconds). The spatial-scale gap is equally staggering, from atomic lattice scale (Angstroms) to device dimensions (m). And yet, neither of the limiting scales is sufficient to provide a good-enough handle for material and device design: On one had we wish atomistic realism across within reaction zone in order to account for complex difficult-to-predict reaction paths; on the other hand we wish to make contact with engineering systems and data. The fundamental question is, therefore: How to affect space-time coarse-graining (atoms to device) without introducing spurious physics and without essential loss of information? In effect, we wish for atomistic realism without the need to resolve the length scale of the crystal lattice and the time scale of thermal vibrations. We have addressed this challenge by jettisoning *ab initio* molecular dynamics if favor of non-equilibrium statistical mechanics. In this paradigm shift, phase space is replaced by atomic-level temperatures and molar-fractions, Newtonian dynamics by atomic-level heat and mass diffusive transport, the required spatial resolution is controlled by temperature and concentration gradients and the required temporal resolution is controlled by diffusional transients. The entire theory is derived consistently from: Jayne's maximum entropy principle, which enables the definition of atomic-level free entropies with non-uniform temperatures and molar fractions; and from a reformulation of Onsager kinetics at the atomistic level. The approach supplies atomistic realism and, in particular, it takes as input an arbitrary (empirical) interatomic potential. In addition, empirical kinetic equations may also be supplied at the atomistic level. The spatial resolution of the model is additionally adapted according to local resolution needs, from atomistic to continuum, using the quasicontinuum method (E.B. Tadmor *et al.*, *Phil. Mag. A*, **73**(6): 1529-1563, 1996). We are in the process of implementing the approach and applying it to a simple validation/test problem: the combustion of graphite. Graphite supplies a good test material as it exhibits two-order-of-magnitude contrast in the components of its thermal conductivity tensor. We specifically simulate a slab of graphite in contact with an oxygen reservoir, and track the combustion reaction as it progresses through the slab, the evolution of the temperature field, the elasticity of the unreacted graphite and the hydrodynamics of the reaction products. In order to account for chemical reactions we use a ReaxFF C-O interatomic potential available in LAMMS. The aim is to ascertain the fidelity of predictions of the dependence of the reaction-front speed on the orientation of the graphite lattice.
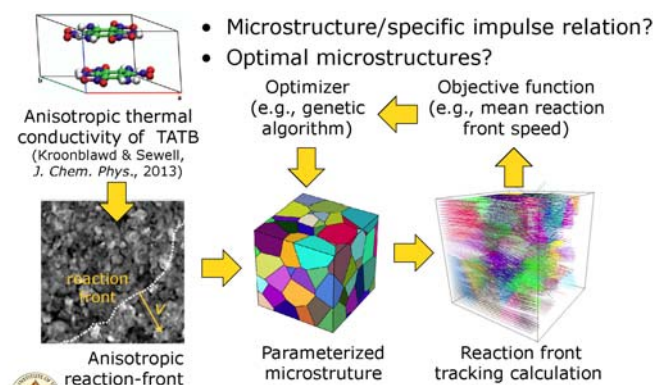
Figure 67 Propellant Microstruture

Development of methods to optimize propellant microstructures. The aim of this effort build on fundamental information from atomic-scale calculations, including orientation-dependent reaction-front speeds, in order to optimize parameterized propellant microstructures of interest, including composites comprising a Polymer binder, oxidizer granules and additives (e.g., NH_4ClO_4 Composite Propellant, APCP). Key design parameters to be optimized include volume fractions, textures and grain/inclusion morphologies. We connect micromechanical properties to overall propellant performance through front tracking simulations of the passage of reaction fronts through representative volume elements, thus determining effective/macroscopic burning rates. Such effective burning rates are subsequently optimized for maximum specific impulse. To date, we have completed the development and testing of a ray-tracing solver with capability for tracking the passage of reaction fronts through arbitrary locally-anisotropic spatial microstructures. At present, the local reaction-front speed depends on the local anisotropic thermal conductivities through a simple one-step reaction model, but the computational capability is sufficiently general to integrate micromechanical models as they become available. The front tracking calculations are fast enough as to make microstructural optimization feasible.

C.   Continuum Modeling and Simulation of Microscopic, Multi-phase, Reactive Processes of Reactants at the Nano- and Microscale (D. Scott Stewart andMoshe Matalon, UIUC)

The efforts of Professors D. Scott Stewart and Moshe Matalon, and their students have been directed at continuum-based modeling and simulation of multifunctional energetic materials of interest to the US Air Force Office of Scientific Research, for advanced propulsion. For the contract year, the main effort has been modeling of condensed phase reaction/diffusion of mobile species with applications to metal combustion. And, specifically, the Stewart/Matalon team developed:

1) A model of generic solid/liquid condensed phase combustion of separated reactants (reaction/diffusion flames) dubbed the "Gibbs formulation". This included modeling of both energetic solids and liquids. The work on the multicomponent formulation is being prepared for publication [191].
2) Developed an analysis of a fundamental small-scale three components model (that is applicable to metal combustion with oxidizers). This model has been articulated for Aluminum (Al), oxidizers and binders in particular in a generic counterflow flame configuration. This work is currently being prepared for publication [192].
3) Started the development of a theory of a condensed phase homogenization/averaging.

Modeling of condensed phase reaction/diffusion of mobile species, with applications to metal combustion (Matalon/Stewart/Bdzil). Solid propellants are mixtures of metal particles, binders and various oxidizers that are combined in a mixture that is molded to manufacture large propellant grain configurations.

83

Substantial decomposition of the reactive materials takes place as the gross gas/condensed phase interface (surface) progresses through the large propellant grain. Exothermic reaction takes place in the condensed phase in the sub-surface regions. Moreover, the extreme temperature gradients and the associated thermal expansion cause the condensed phase materials to swell and set up flows around reactants that are initially separated. At the interfaces of reactants (metals and binders) and oxidizers (like Ammonium Perchlorate or other novel oxidizers) diffusion flames in the condensed materials can be established.

Initial considerations included looking at generic configurations that are representative of actual or realizable microstructures. Figure 68 shows a representative microstructure of a composite solid propellant. Figure 69 shows a characteristic schematic (based on a real microstructure) that indicates the generic and ubiquitous nature of a counterflow configuration that has two opposed flows of reactants (say Fuel and Oxidizer) in the condensed phase as one nears the condensed/gas surface. Figure 70 shows an inset that highlights the counterflow configuration our team analyzed in this past year
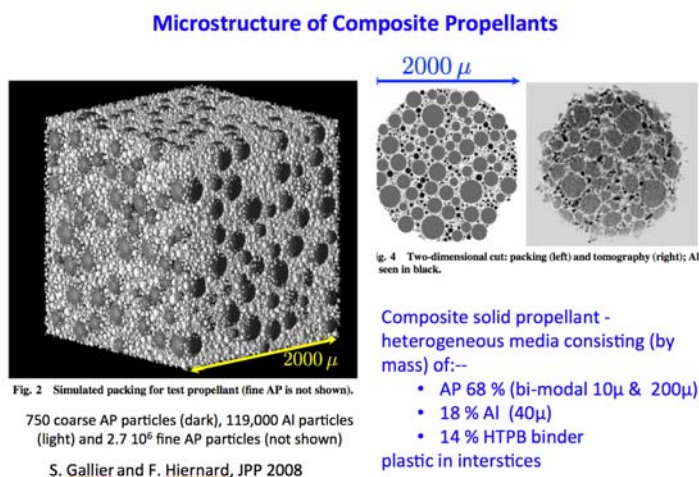
Figure 68 A representative microstructure of a composite solid propellant.
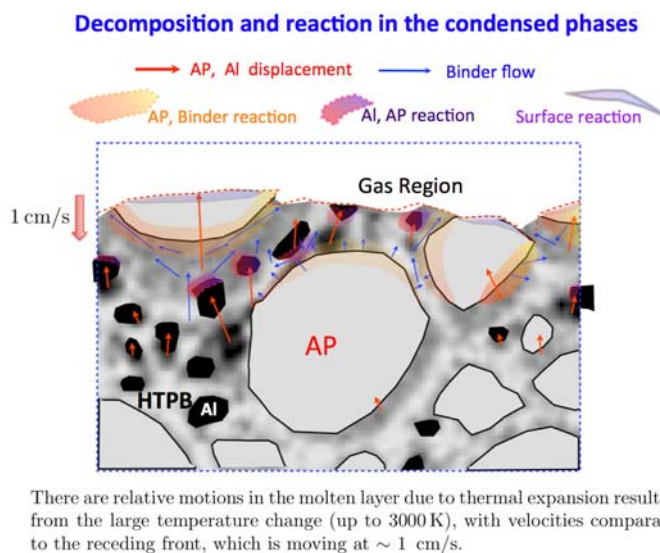
Figure 69 Schematic of a temporary state during the burning of a solid propellant (based on the microstructure shown in Fig. 68). The dashed corrugated curve on top illustrates the interface advancing through the propellant grain.

Multi-component, model for separated reactants
Condensed phase diffusion flames
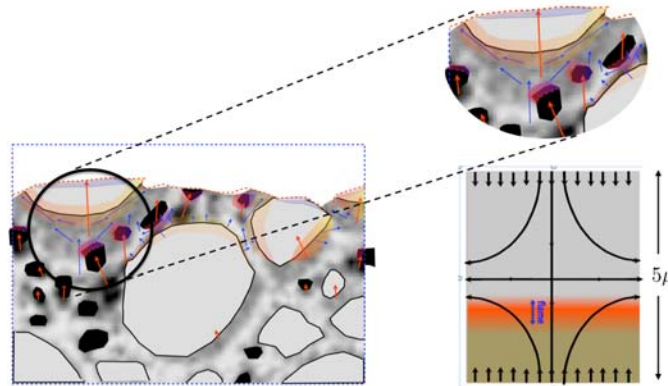
Figure 70 The inset on the right shows the relevance of the counterflow configuration studied by the Matalon/Stewart team in the contract year to the large-scale propellant burning.

Our team analyzed the counter flow flame configuration that has the following model elements:

- General equations for a multi-component (condensed) reactive material
- A Stefan-Maxwell diffusion model that leads to a generalized Fick's diffusion model
- Temperature and concentration dependent diffusion
- A generic three component counter flow flame configuration with 2 reactants that combine to generate products
- Arrhenius reaction rate kinetics
- Asymptotic analysis for large Damkohler number and activation energy, and explicit flame structure formulas
- Accompanying numerical solutions of the model equations for verification and generalization purposes

The work represented by the above list is being prepared for publication [192,193].

Figure 71 is a sketch of the flame structure that illustrates the unique characteristics of diffusion flames in condensed reactants. The striking element is related to the very small diffusion mobility of the condensed species which, in contract to gaseous flames, can only diffuse towards the reaction zone is a very thin mixing-zone where the temperature is sufficiently high. The mixing layer is seen to be significantly narrower than the heat conduction layers that are due to the $O(1)$ thermal diffusivities, and extend to much larger distances. In addition this type of flame leads to the possibility of extinction when the strain rate exceeds a critical value (or the properly defined Damkohler number D is reduced significantly, see Figure 72). This picture indicates the basic result that is being prepared for publications [192] & [193].
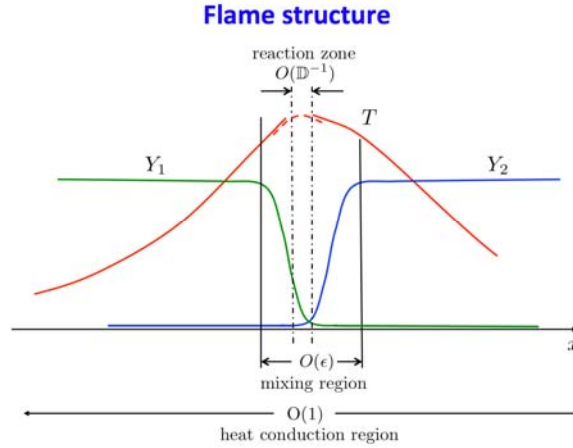
Flame structure

Figure 71 Sketch of the generic condensed phase diffusion flame structure based on recent asymptotic results by the UIUC team.

State diagram – burning/non-burning states ignition/extinction phenomena

Damköhler number $\mathbb{D} \sim$ residence time controlled by the strain rate ε.
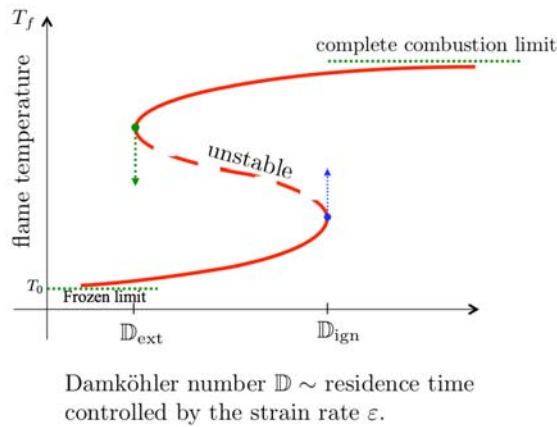
Figure 72 Typical response curve of flame temperature vs Damkohler number, illustrating the possibility of extinction states at sufficiently high strain rates (small D), based on our recent asymptotic and numerical results, [192].

Development of a continuum model for an <u>anisotropic energetic material</u> that undergoes phase change and chemical reaction subject to thermal loading and shear stress. As part of the modeling effort, the general multi-component formulation (dubbed the "Gibbs formulation") has been extended to develop a model for energetic solids that undergo decomposition. Some candidates are TATB crystals and Fox 7 (DADNE). This work is being done in collaboration with the U Missouri team. Figure 73 shows an overview sketch that represents this effort.

B) Development of a continuum model for an _anisotropic energetic material_ that undergoes phase change and chemical reaction subject to thermal loading and shear stress.

TATB and Fox7

20 µm

c) TATB Platelets
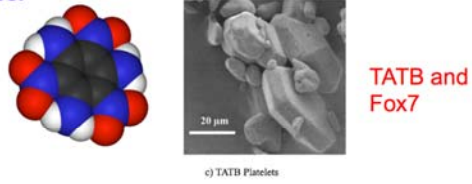
Mixture of a small-strain (anisotropic) elastic solid and compressible melt liquids and products

$$A \rightarrow B \rightarrow C$$

solid $\quad$ liquid $\quad$ Products (l)

$Y_1 \qquad Y_2 \qquad Y_3$
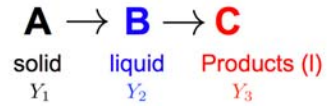
Figure 73 The UIUC team is developing a continuum-based model informed by atomistics for anisotropic energetic solids.

VII.   References

[1]   G. P. Sutton and O.Biblarz, "Rocket Propulsion Elements", A Wiley Interscience Pub., NY, 2001.

[2]   B. Palaszewski, L. S. Ianovski, and P. Carrick, "Propellant Technologies: Far Reaching Benefits for Aeronautical and Space Vehicle Propulsion", *J. of Propulsion and Power*, Vol. 14, No. 5, 1998, pp. 641-648.

[3]   E.W. Price, R. K. Sigman, in: V. Yang, T. B. Brill, and W. Z. Ren (Eds.), "Solid Propellant Chemistry, Combustion, and Motor Interior Ballistics", *AIAA Progress in Aeronautics and Astronautics*, Vol. 185, 2000, pp. 663-687.

[4]   D. R. Martin, *Journal of Chemical Education*, Vol. 36 No. 5, 1959, p. 208

[5]   A. Ulas, K. K. Kuo, and C. Gotzmer, *Combust. Flame*, Vol. 127, No. 1-2, 2001, pp. 1935-1957

[6]   S. G. Shore and R. W. Parry, *Journal of the American Chemical Society*, Vol. 77, No. 22, 1955, pp. 6084-6085

[7]   S. G. Shore and R. W. Parry, *Journal of the American Chemical Society,* Vol. 80, No. 1, 1958, pp. 8-12

[8]   C. F. Lane, *Ammonia-Borane and Related NBH Compounds and Materials: Safety Aspects, Properties and Applications (A survey completed as part of a project for the DOE Chemical Hydrogen Storage Center of Excellence, Contract # DE-FC36-05GO15060)*, 2006

[9]   G. Wolf, J. Baumann, F. Baitalow, and F. P. Hoffmann, *Thermochimica Acta*, Vol. 343, No. 1-2, 2000, pp. 19-25

[10]   M. R. Weismiller, T. L. Connell, G. A. Risha, and R. A. Yetter, *Characterization of Ammonia Borane (NH_3BH_3) Enhancement to a Paraffin Fueled Hybrid Rocket*, 46th AIAA/ASME/SAE/ASEE Joint Propulsion Conference & Exhibit, July 2010, 2010; Nashville, TN, 2010.

[11]   R. C. Brown, C. E. Kolb, H. Rabitz, S. Y. Cho, R. A. Yetter, and F. L. Dryer, *International Journal of Chemical Kinetics*, Vol. 23, 1991, pp. 957-970

[12]   R. A. Yetter, S. Y. Cho, H. Rabitz, F. L. Dryer, R. C. Brown, and C. E. Kolb, *Symposium (International) on Combustion*, Vol. 22, No. 1, 1989, p. 919

[13]   R. A. Yetter, H. Rabitz, F. L. Dryer, R. C. Brown, and C. E. Kolb, *Combust. Flame*, Vol. 83, No. 1-2, 1991, pp. 43-62

[14]   L. Pasternack, *Combust. Flame*, Vol. 90, No. 3-4, 1992, pp. 259

[15]   N. L. Allinger, Y. H. Yuh, and J. H. Lii, *Journal of the American Chemical Society*, Vol. 111, No. 23, 1989, p. 8551

[16]   S. L. Mayo, B. D. Olafson, and W. A. Goddard, *The Journal of Physical Chemistry*, Vol. 94, No. 26, 1990, p. 8897

[17]   M. R. Weismiller, A. C. T. van Duin, J. Lee, and R. A. Yetter, *J. Phys. Chem. A,* Vol. 114, 2010, pp. 5485-5492

[18]   A. C. T. van Duin, S. Dasgupta, F. Lorant, and W. A. Goddard, *Journal of Physical Chemistry A*, Vol. 105, No. 41, 2001, pp. 9396-9409 10.1021/jp004368u.

[19]   M. F. Russo Jr and A. C. T. van Duin, "Nuclear Instruments and Methods in Physics Research Section B", *Beam Interactions with Materials and Atoms*, Vol. 269, No. 14, 2011, p. 1549

[20]   A. Strachan, E. M. Kober, A. C. T. van Duin, J. Oxgaard, and W. A. Goddard, *Journal of Chemical Physics*, Vol. 122, No. 5, 2005, 10 054502 10.1063/1.1831277.

[21]   H. J. C. Berendsen, J. P. M. Postma, W. F. Vangunsteren, A. Dinola, and J. R. Haak, *Journal of Chemical Physics*, Vol. 81, No. 8, 1984, pp. 3684-3690

[22]   M. D. Allendorf and C. F. Melius, *The Journal of Physical Chemistry A*, Vol. 101, No. 14, 1997, p. 2670

[23]   D. A. Dixon and M. Gutowski, *J. Phys. Chem. A*, Vol. 109, No. 23, 2005, pp. 5129-5135

[24] P. R. P. Barreto, A. F. A. Vilela, and R. Gargano, *International Journal of Quantum Chemistry*, Vol. 103, No. 5, 2005, pp. 659

[25] A. D. Becke, *Journal of Chemical Physics*, Vol. 98, No. 7, 1993, pp. 5648-5652

[26] A. D. Becke, *Physical Review A*, Vol. 38, No. 6, 1988, pp. 3098-3100

[27] C. T. Lee, W. T. Yang, and R. G. Parr, *Phys. Rev. B*, Vol. 37, No. 2, 1988, pp. 785-789

[28] M. M. Francl, W. J. Pietro, W. J. Hehre, J. S. Binkley, M. S. Gordon, D. J. Defrees, and J. A. Pople, *Journal of Chemical Physics*, Vol. 77, No. 7, 1982, pp. 3654-3665

[29] Pc. Harihara and J. A. Pople, *Chemical Physics Letters*, Vol. 16, No. 2, 1972, p. 217

[30] Jaguar 7.8, Schrodinger LLC, New York, NY, 2011

[31] R. J. Kee, F. M. Rupley, J. A. Miller, M. E. Coltrin, J. F. Grcar, E. Meeks, H. K. Moffat; A. E. Lutz, G. Dixon-Lewis, M. D. Smooke, J. Warnatz, G. H. Evans, R. S. Larson, R. E. Mitchell, L. R. Petzold, W. C. Reynolds, M. Caracotsios, W. E. Stewart, P. Glarborg, C. Wang, and O. Adigun, CHEMKIN Collection, Release 4.0, Reaction Design, Inc., San Diego, CA, 2000

[32] L. E. Fried, K. R. Glaesemann, W. M. Howard, P. C. Souers, and P. A. Vitello, Cheetah, Lawrence Livermore National Laboratory, Livermore, C.A., 2004

[33] M. L. Hobbs, M. R. Baer, and B. C. McGee, *Propellants, Explosives, and Pyrotechnics*, Vol. 25, No. 5, 1999, pp. 269-279

[34] R. P. Lindstedt, F. C. Lockwood, and M. A. Selim, *Combust. Sci. Technol.*, Vol. 108, No. 4-6, 1995, pp. 231-254

[35] M. T. Nguyen, V. S. Nguyen, M. H. Matus, G. Gopakumar, and D. A. Dixon, *Journal of Physical Chemistry A*, Vol. 111, No. 4, 2007, pp. 679-690

[36] R. J. Kee, F. M. Rupley, J. A. Miller, M. E. Coltrin, J. F. Grcar, E. Meeks, H. K. Moffat, A. E. Lutz, G. Dixon-Lewis, M. D. Smooke, J. Warnatz, G. H. Evans, R. S. Larson, R. E. Mitchell, L. R. Petzold, W. C. Reynolds, M. Caracotsios, W. E. Stewart, P. Glarborg, C. Wang, and O. Adigun, TRANSPORT library, CHEMKIN Collection, Release 3.6, Reaction Design, Inc., San Diego, CA, 2000

[37] J. O. Hirschfelder and M. A. Eliason, *Annals of the New York Academy of Sciences*, Vol. 67, No. 9, 1957, p. 451

[38] R. A. Svehla, *Estimated Viscosities and Thermal Conductivities of Gases at High Temperatures*, 1962

[39] E. Clementi, D. L. Raimondi, and W. P. Reinhardt, *The Journal of Chemical Physics*, Vol. 47, No. 4, 1967, pp. 1300-1307

[40] V. Mokrushin, V. Bedanov, W. Tsang, M. Zachariah, and V. Knyazev, Chemrate, version 1.5.8, NIST, Gaithersburg, MD, 2009

[41] M. W. Chase, T. National Institute of Standards and, NIST-JANAF thermochemical tables, American Chemical Society; American Institute of Physics for the National Institute of Standards and Technology, [Washington, D.C.]; Woodbury, N.Y., 1998,

[42] A. Staubitz, A. P. M. Robertson, and I. Manners, *Chemical Reviews*, Vol. 110, No. 7, 2010, p. 4079

[43] M. G. Hu, R. A. Geanangel, and W. W. Wendlandt, *Thermochimica Acta*, Vol. 23, No. 2, 1978, pp. 249-255

[44] G. Wolf, J. Baumann, F. Baitalow, and F. P. Hoffmann, *Thermochimica Acta*, Vol. 343, No. 1-2, 2000, pp. 19-25.

[45] F. Baitalow, J. Baumann, G. Wolf, K. Jaenicke-R ßler, and G. Leitner, *Thermochimica Acta*, Vol. 391, 2002, p. 159

[46] J. Baumann, E. Baitalow, and G. Wolf, *Thermochimica Acta*, Vol. 430, No. 1-2, 2005, pp. 9-14, 10.1016/j.tca.2004.12.002.

[47] A. C. Stowe, W. J. Shaw, J. C. Linehan, B. Schmid, and T. Autrey, *Physical Chemistry Chemical Physics*, Vol. 9, No. 15, 2007, pp. 1831-1836, 10.1039/b617781f.

[48] S. Frueh, R. Kellett, C. Mallery, T. Molter, W. S. Willis, C. King'ondu, and S. L. Suib, *Inorganic Chemistry*, Vol. 50, No. 3, 2011, pp. 783-792

[49] Y. Oyumi and T. B. Brill, *Combust. Flame*, Vol. 62, No. 3, 1985, pp. 213

[50] E. S. Kim, H. S. Lee, C. F. Mallery, and S. T. Thynell, *Combust. Flame*, Vol. 110, No. 1-2, 1997, pp. 239

[51] A. Chowdhury and S. T. Thynell, *Thermochimica Acta*, Vol. 443, No. 2, 2006, p. 159

[52] J. D. Carpenter, B. S. Ault, J. Phys. Chem., Vol. 95, No. 9, 1991, pp. 3502-3506

[53] M. C. L. Gerry, W. Lewisbevan, A. J. Merer, and N. P. C. Westwood, *J. Mol. Spectrosc.*, Vol. 110, No. 1, 1985, pp. 153-163

[54] K. Niedenzu, W. Sawodny, H. Watanabe, J. W. Dawson, T. Totani, and W. Weber, *Inorganic Chemistry*, Vol. 6, No. 8, 1967, pp. 1453

[55] M. G. Hu, J. M. Vanpaasschen, and R. A. Geanangel, *Journal of Inorganic & Nuclear Chemistry*, Vol. 39, No. 12, 1977, pp. 2147-2150

[56] R. Komm, R. A. Geanangel, and R. Liepins, *Inorganic Chemistry*, Vol. 22, No. 11, 1983, pp. 1684-1686

[57] K. W. Boddeker, S. G. Shore, and R. K. Bunting, *Journal of the American Chemical Society*, Vol. 88, No. 19, 1966, pp. 4396

[58] J. Smith, K. S. Seshadri, and D. White, *J. Mol. Spectrosc.*, Vol. 45, No. 3, 1973, p. 327

[59] M. D. Allendorf and C. F. Melius, *The Journal of Physical Chemistry A*, Vol. 101, No. 14, 1997, pp. 2670

[60] M. R. Weismiller, A. C. T. van Duin, J. Lee, and R. A. Yetter, *J. Phys. Chem. A*, Vol. 114, 2010, pp. 5485-5492

[61] W. R. Nutt and M. L. McKee, *Inorganic Chemistry*, Vol. 46, No. 18, 2007, p. 7633

[62] E. W. Price and R. K. Sigman, "Solid Propellant Chemistry, Combustion, and Motor Interior Ballistics", Yang, V; Brill, T.B.; Ren, and W.Z. (Eds.), *AIAA Progress in Astronautics and Aeronautics*, Vol. 185, 2000, pp. 663-687.

[63] M. A. Trunov, M. Schoenitz, and E. L. Dreizin, "Effect of Polymorphic Phase Transformations in Alumina Layer on Ignition of Aluminum Particles", *Combust. Theory Modell*, Vol. 10, 2006, pp. 603- 623.

[64] T. Campbell, R. K. Kalia, A. Nakano, and P. Vashishta, "Dynamics of Oxidation of Aluminum Nanoclusters using Variable Charge Molecular-Dynamics Simulations on Parallel Computers", *Phys. Rev. Lett.* Vol. 82, 1999, pp. 4866-4869.

[65] Y. Huang, G. A. Risha, V. Yang, R. A. Yetter, "Effect of Particle Size on Combustion of Aluminum Particle Dust in Air", *Combust. Flame*, Vol. 156, 2009, pp. 5-13.

[66] T. J. Foley, C. E. Johnson, and K. T. Higa, "Inhibition of Oxide Formation on Aluminum Nanoparticles by Transition Metal Coating", *Chem. Mater.,* Vol. 17, 2005, pp. 4086-4091.

[67] T. Uchikoshi, Y. Sakka, M. Yoshitake, and K. Yoshihara, "A Study of the Passivating Oxide Layer on Fine Nickel Particles", *Nanostruct. Mater.*, Vol. 4, 1994, pp. 199-206.

[68] E. Shafirovich, A. Mukasyan, L. Thiers, A. Varma, B. Legrand, C. Chauveau, and I. Gokalp, "Ignition and Combustion of Al Particles Clad by Ni", *Combust. Sci. Tech.*, Vol. 174, 2002, pp. 125-140.

[69] D. A. Yagodnikov and A. V. Voronetskii, "Experimental and Theoretical Study of the Ignition and Combustion of an Aerosol of Encapsulated Aluminum Particles", *Combust. Expl. Shock Waves*, Vol. 33, 1997, pp. 49-55.

[70] T. A. Andrzejak, E. Shafirovich, and A. Varma, "Ignition Mechanism of Nickel-Coated Aluminum Particles", *Combust. Flame*, Vol. 150**,** 2007, pp. 60-70.

[71] A. P. Ilyin, A. A. Gromov, V. I. Vereshchagin, E. M. Popenko, V. A. Surgin, and H. Lehn, "Combustion of Agglomerated Ultrafine Aluminum Powders in Air", *Combust. Explos Shock Waves*, Vol. 37, 2001, pp. 664-669.

[72] Y. S. Kwon, A. A. Gromov, A. P. Ilyin, E. M. Popenko, and G. H. Rim, "The Mechanism of Combustion of Superfine Aluminum Powders", *Combust. Flame*, Vol. 133, 2003, pp. 385-391.

[73] A. Pivkina, P. Ulyanov, Y. Frolov, S. Zavyolov, and J. Schoonman, "Nanomaterials for Heterogeneous Combustion", *Propell. Expl. Pyrotech.*, Vol. 29, 2004, pp. 39-48.

[74]   K. J. Klabunde, J. Stark, O. Koper, C. Mohs, D. G. Park, S. Decker, Y. Jiang, I. Lagadic, and D. Zhang, "Nanocrystals as Stoichiometric Reagents with Unique Surface Chemistry", *J. Phys. Chem.*, Vol. 100, 1996, pp. 12142-12153.

[75]   P. Puri and V. Yang, "Effect of Particle Size on Melting of Aluminum at Nano Scales", *J. Phys. Chem. C*, Vol. 111, 2007, pp. 11776-11783.

[76]   A. Rai, D. Lee, K. Park, and M. R. Zachariah, "Importance of Phase Change of Aluminum in Oxidation of Aluminum Nanoparticles", *J. Phys. Chem. B*, Vol. 108, 2004, pp. 14793-14795.

[77]   G. A. Risha, S. F. Son, R. A. Yetter, V. Yang, and B. C. Tappan, "Combustion of Nano-Aluminum and Liquid Water", *Proc. Combust. Inst.*, Vol. 31, 2007, pp. 2029-2036.

[78]   P. Puri and V. Yang, "Thermo-Mechanical Behavior of Nanoalumnum Particles with Oxide Layers During Melting", *J. Nanopart. Res.*, Vol. 12, 2010, pp. 2989-3002.

[79]   F. Delogu, "Numerical Simulation of the Thermal Response of Al Core/Ni Shell Nanometer-Sized Particles", *Nanotechnology*, Vol. 18, 2007, pp. 505702.

[80]   B. J. Henz, T. Hawa, and M. Zachariah, "Molecular Dynamics Simulation of the Energetic Reaction between Ni and Al Nanoparticles", *J. Appl. Phys.*, Vol. 105, 2009, pp. 124310.

[81]   A.V. Evteev, E. V. Levchenko, D.P. Riley, I. V. Belova, and G. E. Murch, "Reaction of a Ni-Coated Al Nanoparticles to Form B2-NiAl: A Molecular Dynamics Study", *Philos. Mag. Lett.*, Vol. 89, 2009, pp. 815-830.

[82]   H. C. Andersen, "Molecular Dynamics Simulations at Constant Pressure and/or Temperature", *J. Chem. Phys.*, Vol. 72, 1980, pp. 2384-2393.

[83]   S. Nose, "A Unified Formulation of the Constant Temperature Molecular Dynamics Methods", *J. Chem. Phys.*, Vol. 81, 1984, pp. 511-519.

[84]   M. E. Tuckerman, *Statistical Mechanics: Theory and Molecular Simulation*; Oxford University Press: New York, USA, 2010.

[85]   Y. Shibuta and T. Suzuki, "A Molecular Dynamics Study of Cooling Rate during Solidification of Metal Particles", *Chem. Phys. Lett.*, 502, 2011, pp. 82-86.

[86]   M. P. Allen and D. J. Tildesley, *Computer Simulation of Liquids*; Oxford University Press: USA, 1989.

[87]   Y. Zhuo, M. Karplus, K. D. Ball, and R. S. Berry, "The Distance Fluctuation Criterion for Melting: Comparison of Square-Well and Morse Potential Models for Clusters and Homopolymers", *J. Chem. Phys.*, Vol. 116, 2002, pp. 2323-2329.

[88]   J. D. Gezelter, E. Rabani, and B. J. Berne, "Can Imaginary Instantaneous Normal Mode Frequencies Predict Barriers to Self-Diffusion?", *J. Chem. Phys.*, Vol. 107, 1997, pp. 4618-4627.

[89]   M. S. Daw and M. I. Baskes, "Embedded-Atom Method: Derivation and Application to Impurities, Surfaces, and Other Defects in Metals", *Phys. Rev. B*, Vol. 29, 1984, pp. 6443-6453

[90]   F. Cleri and V. Rosato, "Tight-Binding Potentials for Transition Metals and Alloys", *Phys. Rev. B*, Vol. 48, 1993, pp. 22-33.

[91]   E. B .Krissinel and J. Jellinek, "13-Atom Ni-Al Alloy Clusters: Structures and Dynamics", *Int. J. Quantum Chem.*, Vol. 62, 1997, pp. 185-197.

[92]   F. Delogu, "Demixing Phenomena in NiAl Nanometer-Sized Particles", *Nanotechnology*, Vol. 18, 2007, pp. 065708.

[93]   C. Kittel, *Introduction to Solid State Physics*; Wiley: New York, USA, 1966.

[94]   E. A. Brandes and G.B.Brook, *Smithells Metals Reference Handbook*; Butterworth-Heinemann Ltd: Oxford, 1992.

[95]   O. Kubaschewski, C. B. Alcock, and P. J. Spencer, *Materials Thermochemistry*; Pergamon Press: Oxford, 1993.

[96]   P. Puri and V. Yang, "Effect of Voids and Pressure on Melting of Nano-Particulate and Bulk Aluminum", *J. Nanopart. Res.*, Vol. 11, 2009, pp. 1117-1127.

[97]   Q. S. Mei and K. Lu, "Melting and Superheating of Crystalline Solids: From Bulk to Nanocrystals", *Prog. Mater. Sci.*, Vol. 52, 2007, pp. 1175-1262.

[98] Y. Qi, T. Cagin, W. L. Johnson, and W. A. Goddard, "Melting and Crystallization in Ni Nanoclusters: The Mesocale Regime", *J. Chem. Phys.*, Vol. 115, 2001, pp. 385-394.

[99] J. Eckert, J. C. Holzer, C. C. Ahn, Z. Fu, and W. L. Johnson, "Melting Behavior of Nanocrystalline Aluminum Powders", *Nanostruct. Mater.*, Vol. 2, 1993, pp. 407-413.

[100] S. L. Lai, J. R. A. Carlsoon, and L. H. Allen, "Melting Point Depression of Al Clusters Generated during the Early Stages of Film Growth: Nanocalorimetry Measurements", *Appl. Phys. Lett.*, Vol. 72, 1998, pp. 1098-1100.

[101] V. I. Levitas and K. Samani, "Size and Mechanics Effects in Surface-Induced Melting of Nanoparticles", *Nat. Commun.*, Vol. 2, 2011, p. 284.

[102] V. I. Levitas and K. Samani, "Coherent Solid/Liquid Interface with Stress Relaxation in a Phase-Field Approach to the Melting/Solidification Transition", *Phys. Rev. B*, Vol. 84, 2011, p. 140103.

[103] S. N. Luo and T. J. Ahrens, "Superheating Systematics of Crystalline Solids", *Appl. Phys. Lett.*, Vol. 82, 2003, pp. 1836-1838.

[104] J. Daeges, H. Gleiter, and J. H. Perepezko, "Superheating of Metal Crystals", *Phys. Lett. A*, Vol. 119, 1986, pp. 79-82.

[105] J. Zhong, L. H. Zhang, Z. H. Jin, M. L. Sui, and K. Lu, "Superheating of Ag Nanoparticles Embedded in Ni Matrix", *Acta Mater.*, Vol. 49, 2001, pp. 2897-2904.

[106] Q. S. Mei, S. C. Wang, H. T. Cong, Z. H. Jin, and K. Lu, "Pressure-Induced Superheating of Al Nanoparticles Encapsulated in Al_2O_3 Shells Without Epitaxial Interface *Acta Mater.*", Vol. 53, 2005, pp. 1059-1066.

[107] H. W. Sheng, G.Ren, L. M. Peng, Z. Q. Hu, and K. Lu, "Superheating and Melting-Point Depression of Pb Nanoparticles Embedded in Al Matrices", *Philos. Mag. Lett.*, Vol. 73, 1996, pp. 179-186.

[108] K. Lu and Z. H. Jin, "Melting and Superheating of Low-Dimensional Materials", *Curr. Opin. Solid State Mater. Sci.*, Vol. 5, 2001, pp. 39-44.

[109] Z. H. Jin, H. W .Sheng, and K. Lu, "Melting of Pb Clusters Without Free Surfaces", *Phys. Rev. B.*, Vol. 60, 1999, pp. 141-149.

[110] R. Hu and P. Nash, "The Enthalpy of Formation of NiAl", *J. Mater. Sci.*, Vol. 40, 2005, pp. 1067-1069.

[111] C. A. Alexander, J. S. Ogden, S. M. Risser, and V. E. Wood, "Thermodynamic Characterization of NiAl", *J. Chem. Thermodyn.*, Vol. 41, 2009, pp. 610-616.

[112] T. B. Massalski, *Binary Phase Diagrams*; ASM International: Ohio, 1992.

[113] W. Liu and J. N. Dupont, "In-Situ Reactive Processing of Nickel Aluminides by Laser-Engineered Net Shaping", *Metall. Mater. Trans. A*, Vol. 34, 2003, pp. 2633-2641.

[114] B. J. Henz, "Molecular Dynamics Studies of Metallic Nanoparticles", Ph.D. Thesis, University of Maryland, 2009.

[115] V. I. Levitas, "Burn Time of Aluminum Nanoparticles: Strong Effect of the Heating Rate and Melt Dispersion Mechanism", *Combust. Flame*, Vol. 156, 2009, pp. 543-546.

[116] V. I. Levitas, M. Pantoya, G. Chauhan, and L. Rivero, "Effect of the Alumina Shell on the Melting Temperature Depression for Aluminum Nanoparticles", *J. Phys. Chem. C*, Vol. 113, 2009, pp. 14088-14096.

[117] J. Sun and S.L. Simon, "The Melting Behavior of Aluminum Nanoparticles", *Thermochim. Acta*, Vol. 453, 2007, pp. 32-40.

[118] V. Yang, T. B. Brill, and W. Z. Ren (Eds.), "Solid Propellant Chemistry, Combustion, and Motor Interior Ballistics", *AIAA Progress in Aeronautics and Astronautics*, Vol. 185, 2000, p. 663-687.

[119] G. D. Roy (Ed.), Advances in Chemical Propulsion: Science to Technology, CRC Press, 2001 (Chapter 8).

[120] E. Shafirovich, V. Diakov, and A. Varma, *Combust. Flame*, Vol. 144, 2006, pp. 415-418.

[121] M. Epstein, H.K. Fauske, and T.G. Theofanous, *Nucl. Eng. Des.*, Vol. 201, 2000, pp. 71-82.

[122] G .A. Risha, S. F. Son, R. A. Yetter, V. Yang, and B. C. Tappan, *Proc. Combust. Inst.*, Vol. 31, 2007, pp. 2029- 2036.

[123]   D. S. Sundaram, V. Yang, T. L. Connell Jr., G. A. Risha, and R. A. Yetter, *Proc .Combust. Inst*., Vol. 34, 2013, pp. 2221-2228.

[124]   G. A. Risha, T. L. Connell Jr, D. S. Sundaram, R. A. Yetter, and V. Yang. *J. Prop. Power*, accepted

[125]   M. Schoenitz, C. M. Chen, and E. L. Dreizin, *J. Phys. Chem. B*, Vol. 113, 2009, pp. 5136-5140.

[126]   D. K. Kuehl, *AIAA Journal*, Vol. 3, 1965, pp., 2239-2247

[127]   T. G. Theofanous, X. Chen, P. Di Piazza, M. Epstein, and H. F. Fauske, *Phys. Fluids*, Vol. 6, 1994, p. 3513.

[128]   T. Parr, C. Johnson, D. Hanson-Parr, K. Higa, and K. Wilson, Proc. 39th JANNAF Combustion Subcommittee Meeting, Chemical Propulsion Information Agency, 2003.

[129]   M. A. Gurevich, K. I. Lapkina, and E. S. Ozerov, *Fiz. Goreniya Vzryva*, Vol. 6, 1970, pp. 172-175.

[130]   K. J. Klabunde, J. Stark, O. Koper, C. Mohs, D. G. Park, S. Decker, Y. Jiang, I. Lagadic, and D. Zhang, *J. Phys. Chem*., Vol. 100, 1996, pp. 12142-12153.

[131]   P. Puri and V. Yang, *J. Phys. Chem. C*, Vol. 111, 2007, pp. 11776-11783.

[132]   P. Puri and V. Yang, *J. Nanopart. Res*., Vol. 11, 2008, pp. 1117-1127.

[133]   P. Puri and V. Yang, *J. Nanopart. Res*., Vol., 12, 2010, pp. 2989-3002.

[134]   Y. Huang, G. A. Risha, V. Yang, and R. A. Yetter, *Combust. Flame*, Vol. 156, 2009, Pp. 5-13.

[135]   R. A. Yetter, G. A. Risha, and S. F. Son, *Proc. Combust. Inst*., Vol. 32, 2009, pp. 1819-1838.

[136]   V. G. Ivanov, S. N. Leonov, G. L. Savinov, O. V. Gavrilyuk, and O. V. Glazkov, *Combust. Explos. Shock Waves*, Vol. 30, No. 4, 1994, pp. 569 -570.

[137]   V. G. Ivanov, O. V. Gavrilyuk, O. V. Glazkov, and M. N. Safronov, *Combust. Explos. Shock Waves*, Vol. 36, 2000, pp. 213-219.

[138]   G. A. Risha, J. L. Sabourin, V. Yang, R. A. Yetter, S. F. Son, and B. C. Tappan, *Combust. Sci. Tech*., Vol. 180, 2008, pp. 2127-2142.

[139]   Y. Huang, G. A. Risha, V. Yang, and R. A. Yetter, *Proc. Combust. Inst*., Vol. 31, 2007, 2001-2009.

[140]   G. Tichá, W. Pabst, D. S. Smith, *J. Mater. Sci*., Vol. 40, 2005, pp. 5045-5047.

[141]   B. Badrinarayan and J. W. Barlow, *Proc. Solid Freeform Fabrication Symposium*, 1990, pp. 91-97.

[142]   E. W. Lemmon, M. L. Huber, and M. O. McLinden, Reference Fluid Properties, *National Institute of Standards and Technology*, 2007.

[143]   W. F. Gale and T. C. Totemeier, Smithells Metals Reference Book, 8th ed., Elsevier, 2004.

[144]   J. V. Sengers and J. T. R. Watson, *J. Phys. Chem. Ref. Data*, Vol. 15, 1986, pp. 1291-1314.

[145]   E. H. Buyco and F. E. Davis, *J. Chem. Eng. Data*, Vol. 15, 1970, pp. 518-523.

[146]   R. G. Munro, *J. Am. Ceram. Soc*., Vol. 80, 1997, pp. 1919-1928.

[147]   W. H. Press, S. A. Teukolsky, W. T. Vetterling, and B. P. Flannery, "Numerical Recipes in Fortran 77: The Art of Scientific Computing", Cambridge University Press, 1992.

[148]   V. Diakov, M. Diwan, E. Shafirovich, and A. Varma, *Chem. Eng. Sci*., Vol. 62, 2007, pp. 5586-5591.

[149]   M. Diwan, D. Hanna, E. Shafirovich, and A. Varma, *Chem. Eng. Sci*., Vol. 65, 2010, pp. 80-87.

[150]   T. Bazyn, H. Krier, and N. Glumac, *Combust. Flame*, Vol. 145, 2006, pp. 703-713.

[151]   C. Badiola and E. L. Dreizin, *Proc. Combust. Inst*., Vol. 34, 2013, pp. 2237-2243.

[152]   T. Bazyn, H. Krier, and N. Glumac, Proc. *Combust. Inst*., Vol. 31, 2007, pp. 2021-2028.

[153]   O. Levenspiel, "Chemical Reaction Engineering", John Wiley and Sons, New York, 1962, pp. 338-357.

[154]   K. Park, D. Lee, A. Rai, D. Mukherjee, and M. R. Zachariah, *J. Phys. Chem. B*., Vol. 109, 2005, pp. 7290-7299.

[155]   A. Rai, K. Park, L. Zhuo, and M. R. Zachariah, *Combust. Theory Modell*, Vol. 10, 2006, pp. 843-859.

[156]   R. Tomasi and Z. A. Munir, *J. Am. Ceram. Soc*., Vol. 82, 1999, pp. 1985-1992.

[157] I. Glassman and R.A. Yetter, Combustion, 4th ed., Academic Press, 2008.

[158] W. Cai, P. Thakre, and V. Yang, *Combust. Sci. Tech.*, Vol. 180, 2008, pp. 2143-2169.

[159] *M. W. Beckstead, K. Puduppakkam, P. Thakre, and V. Yang, Prog. Energy Combust. Sci., Vol. 33, 2007, pp. 497-551.*

[160] E. W. Price, R. K. Sigman, in: V. Yang, T. B. Brill, W. Z. Ren (Eds.), Solid Propellant Chemistry, Combustion, and Motor Interior Ballistics, Progress in Astronautics and Aeronautics, *AIAA*, Vol. 185, 2000, pp. 663-687.

[161] M. A. Trunov, M. Schoenitz, and E. L. Dreizin, *Combust. Theory Modell.*, Vol. 10, 2006, pp. 604-623.

[162] Y. Huang, G. A. Risha, V. Yang, and R. A. Yetter, *Combust. Flame*, Vol. 156, 2009, pp. 5-13.

[163] I. Glassman, P. Papas, K. Brezinsky, Combust. Sci. Tech. 83 (1992) 161-165.

[164] V. Yang, T. B. Brill, and W. Z. Ren (Eds.), Solid Propellant Chemistry, Combustion, and Motor Interior Ballistics, Progress in Astronautics and Aeronautics, *AIAA*, Vol. 185, 2000.

[165] P. Puri and V. Yang, *J. Phys. Chem. C*, Vol. 111, 2007, pp. 11776-11783.

[166] J. Eckert, J. C. Holzer, C. C. Ahn, Z. Fu, and W. L. Johnson, *Nanostruct. Mater.*, Vol. 2, 1993, pp. 407-413.

[167] P. Puri and V. Yang, *J. Nanopart. Res.*, Vol. 11, 2009, pp. 1117-1127.

[168] P. Puri and V. Yang, *J. Nanopart. Res.*, Vol. 12, 2010, pp. 2989-3002.

[169] L. H. Liang, J. C. Li, and Q. Jiang, *Phys. B*, Vol. 334, 2003, pp. 49-53.

[170] M. Zhao and Q. Jiang, *Solid State Commun.*, Vol. 130, 2004, pp. 37-39.

[171] Z. Zhang, X. X. Lu, and Q. Jiang, *Phys. B*, Vol. 270, 1999, pp. 249-254.

[172] S. Panda and S. E. Pratsinis, *NanoStruct. Mater.*, Vol. 5, 1995, pp. 755-767.

[173] R. Hultgren, P. D. Desai, D. T. Hawkins, M. Gleiser, and K. K. Kelley., Selected Values of Thermodynamic Properties of the Elements, American Society for Metals, 8th Edition, Metal Parks, Ohio, 1973.

[174] S. K. Rhee, *J. Am. Ceram. Soc.*, Vol. 53, 1970, pp. 386-389.

[175] S.W. Chung, E. A. Guliants, C. E. Bunker, P. A. Jelliss, and S. W. Buckner, *J. Phys. Chem. Solids*, Vol. 72, 2011, pp. 719-724.

[176] P. Puri, Ph.D. Thesis, The Pennsylvania State University, 2008.

[177] L. P. H. Jeurgens, W. G. Sloof, F. D. Tichelaar, and E. J. Mittemeijer, *J. Appl. Phys.*, Vol. 92, 2002, pp. 1649-1656.

[178] A. Ermoline and E. L. Dreizin, *Chem. Phys. Lett.*, Vol. 505, 2011, pp. 47-50.

[179] S. Mohan, A. Ermoline, and E. L. Dreizin, *J. Nanopart. Res.*, Vol. 14, 2012, pp. 723-729.

[180] K. J. Klabunde, J. Stark, O. Koper, C. Mohs, D. G. Park, S. Decker, Y. Jiang, I. Lagadic, and D. Zhang, *J. Phys. Chem.*, Vol. 100, 1996, pp. 12142-12153.

[181] JANAF Thermodynamic Tables, 3rd Edition, American Chemical Society, 1981.

[182] A. V. Filippov and D. E. Rosner, *Int. J. Heat Mass Transfer*, Vol. 43, 2000, pp. 127-138.

[183] S. C. Saxena and R. K. Joshi, "Thermal Accommodation and Absorption Coefficient of Gases", 1989, Hemisphere, New York.

[184] D. R. Lide Handbook of Chemistry and Physics, 2003, CRC Press, New York.

[185] Y. V. Martynenko and L. I. Ognev, *Tech. Phys.*, Vol. 50, 2005, pp. 1522-1524.

[186] M. Rosenberg, R. D. Smirnov, and A. Y. Pigarov, *J. Phys. D: Appl. Phys.*, Vol. 41, 2008, p. 015202.

[187] I. S. Altman, *Journal of Aerosol Science*, Vol. 30, 1999, pp. S423-S424

[188] J. D. Hightower and E. W.Price, "Combustion of Ammonium Perchlorate," *Proceedings of the Combustion Institute*, Vol. 11, No. 1, 1967, pp. 463-472.

[189] T. L.Boggs, "Deflagration Rate, Surface Structure, and Subsurface Profile of Self-Deflagrating Single Crystals of Ammonium Perchlorate," *AIAA Journal*, Vol. 8, No. 5, 1970, pp. 867-873.

[190] A. I. Atwood, T. L.Boggs, P. O. Curran, T. P. Parr, D. M. Hanson-Parr, C. F. Price, and J. Wiknich, "Burning Rate of Solid Propellant Ingredients, Part 1: Pressure and Initial Temperature Effects," *Journal of Propulsion and Power*, Vol. 15, No. 6, 1999, pp. 740-747.

[191] D. S. Stewart, M. Matalon, J. Bdzil and K. Lee, "A Gibbs formulation for multi-component condensed phase reactive flow"

[192] S. Kumar, J. Bdzil, M. Matalon and D. Scott Stewart, "Analysis of a counterflow configuration reaction diffusion condensed phase flames with application to thermitic and propellant combustion."

[193] L. Li, D.S. Stewart and M. Matalon, "Diffusion Flames in a finite domain with different counter flow velocities".

PUBLICATIONS

1. T.L. Connell Jr., G.A. Risha, R.A. Yetter, G. Young, D. Sundaram, V. Yang, Combustion of alane and aluminum with water for hydrogen and thermal energy generation, *Proceedings of the Combustion Institute,* Vol. 33, No.2, 2011, 1957-1965.

2. D. Sundaram, V. Yang, T.L. Connell, G.A. Risha, R.A. Yetter, G. Young, Combustion of Aluminum, Aluminum Hydride, and Ice Mixtures, *49th AIAA Aerospace Sciences Meeting*, Orlando, Florida, 2011, AIAA-2011-603.

3. Sundaram, DL; Yang, V; Connell, Jr, TL; Risha, GA; Yetter; Flame Propagation of Nano/Micron-Sized Aluminum Particles and Ice (ALICE) Mixtures, PROCEEDINGS OF THE COMBUSTION INSTITUTE Volume: 34 Pages: 2221-2228 DOI: 10.1016/j.proci.2012.06.129, 2012.

4. "Effects of Particle Size and Pressure on Combustion of Nano-Aluminum Particles and Liquid Water" by D. S. Sundaram, V. Yang, Y. Huang, G. A. Risha, R. A. Yetter. Combustion and Flame, Vol. 160, 2013, pp. 2251-2259.

5. "Thermochemical Behavior of Nickel-Coated Nanoaluminum Particles" by D. S. Sundaram, P. Puri, V. Yang. Journal of Physical Chemistry C, Vol. 117, 2013, pp. 7858-7869.

6.   "Pyrophoricity of Nascent and Passivated Aluminum Particles at Nano Scales" by D. S. Sundaram, P. Puri, V. Yang. Combustion and Flame, Vol. 160, 2013, pp. 1870-1875.

7. Michael R. Weismiller, Adri C. T. van Duin,* Jongguen Lee, and Richard A. Yetter, ReaxFF Reactive Force Field Development and Applications for Molecular Dynamics Simulations of Ammonia Borane Dehydrogenation and Combustion, J. Phys. Chem. A 2010, 114, 5485–5492.

8. M.R. Weismiller, S.Q. Wang, A. Chowdhury, S.T. Thynell, R.A. Yetter, Confined Rapid Thermolysis Studies of Ammonia Borane, THERMOCHIMICA ACTA Volume: 551 Pages: 110-117 DOI: 10.1016/j.tca.2012.10.008, 2013.

9. M.R. Weismiller, M.F. Russo Jr, A.C.T. van Duin, R.A. Yetter, Using molecular dynamics simulations with a ReaxFF reactive force field to develop a kinetic mechanism for ammonia borane oxidation, PROCEEDINGS OF THE COMBUSTION INSTITUTE Volume: 34 Pages: 3489-3497 DOI: 10.1016/j.proci.2012.06.030 Part: 2 , 2013.

10. Johansson, R; Connell Jr, TA; Risha, GA; Yetter, RA; Young, G; Investigation of Solid Oxidizer and Gaseous Fuel Combustion Performance using an Elevated Pressure Counterflow Experiment for Reverse Hybrid Rocket Engine, ENERGETIC MATERIALS AND CHEMICAL PROPULSION Source: ENERGETIC MATERIALS AND CHEMICAL PROPULSION Volume: 11 Issue: 6 Pages: 511-536 DOI: 10.1615/IntJEnergeticMaterialsChemProp.2013005785, 2012.

11. "Thermochemical Behavior of Nano-Sized Aluminum-Coated Nickel Particles" by D. S. Sundaram, P. Puri, V. Yang. Journal of Nanoparticle Research, Submitted.

12. David E. Kittell , Lori J. Groven , Travis R. Sippel , Timothée L. Pourpoint & Steven F. Son (2013) Dependence of Nano-Aluminum and Water Propellant Combustion on pH and Rheology, Combustion Science and Technology, 185:5, 817-834, DOI: 10.1080/00102202.2012.759948.

13. Combustion of Nanoaluminum and Water Propellants: Effect of Equivalence Ratio and Safety/Aging Characterization, Travis R. Sippel,*Timothee L. Pourpoint, and Steven F. Son, Propellants Explos. Pyrotech. 2013, 38, 56–66.
14. Combustion of micron-aluminum and hydrogen peroxide propellants, Christopher R. Zaseck, Steven F. Son, Timothée L. Pourpoint, Combustion and Flame 01/2013; 160(1):184–190. DOI:10.1016/j.combustflame.2012.10.001.
15. Preparation and Characterization of Energetic Crystals with Nanoparticle Inclusions, David A. Reese, Steven F. Son, and Lori J. Groven, Propellants Explos. Pyrotech. 2012, 37, 635–638.
16. Modifying Aluminum Reactivity with Poly(Carbon Monofluoride) via Mechanical Activation, Travis. R. Sippel, Steven F. Son, and Lori J. Groven, Propellants Explos. Pyrotech. 2013, 38, 321–326.
17. M. P. Kroonblawd and T. D. Sewell, J. Chem. Phys. 139, 074503 (2013); subject: anisotropic thermal conductivity in crystalline TATB.